Optimization of the High Brightness Beam Performance of the CERN PSB with H^- Injection

Dissertation
zur Erlangung des Doktorgrades
der Naturwissenschaften

vorgelegt beim Fachbereich Physik
der Johann Wolfgang Goethe-Universität
in Frankfurt am Main

von

Tirsi Prebibaj
aus Bajram Curri

Frankfurt am Main 2023
(D 30)

vom Fachbereich Physik der Johann Wolfgang Goethe-Universität als Dissertation angenommen.

Dekan:

Gutachter:

Datum der Disputation:

Abstract

In the framework of the LHC Injectors Upgrade Project (LIU), the CERN Proton Synchrotron Booster (PSB) went through major upgrades resulting in new effects to study, challenges to overcome and new parameter regimes to explore. To assess the achievable beam brightness limit of the machine, a series of experimental and computational studies in the transverse planes were performed. In particular, the new injection scheme induces optics perturbations that are strongly enhanced near the half-integer resonance. In this thesis, methods for dynamically measuring and correcting these perturbations and their impact on the beam performance will be presented. Additionally, the quality of the transverse beam distributions and strategies for improvement will be addressed. Finally, the space charge effects when dynamically crossing the half-integer resonance will be characterized. The results of these studies and their broader significance beyond the PSB will be discussed.

Acknowledgements

This work would not have been possible without the support and help of many people over the last three years.

I consider myself fortunate to have collaborated with and been supervised not by one, but by three individuals. I am deeply grateful to Dr. Fanouria Antoniou for the opportunity to join CERN and for guiding and motivating me throughout the years. She is an outstanding scientist, an exceptional mentor, and, most importantly, a very kind person. I cannot thank Dr. Hannes Bartosik enough for sharing his immense knowledge and giving me a deeper understanding of the field of particle accelerators. He is an excellent teacher and a great mind. Last but not least, I want to express my appreciation to Dr. Foteini Asvesta for the extensive training and countless hours in the control room. Her experience and intelligence allowed us to overcome many experimental limitations in the PSB.

I would also like to thank my university advisor, Apl. Prof. Dr. Giuliano Franchetti, whose knowledge, ideas and excitement guided the studies in this thesis. Additionally, I am grateful to Prof. Dr. Ulrich Ratzinger for carefully reading and correcting this thesis, and to Hannes Bartosik and Bernhard Holzer for carefully editing the 'Zusammenfassung'.

What makes CERN a unique place is its people. Being part of the BE-ABP group, the INC section, the Space Charge Working Group, the L4-PSB Machine Performance Coordination, the PSB beam commissioning and the Injectors Performance Panel meetings, was a remarkable and highly beneficial experience for me. It gave me the privilege to interact, receive feedback, and gain insights from Guido Sterbini, Giovanni Rumolo, Yannis Papaphilippou, Davide Gamba, Gian Piero Di Giovanni, Simon Albright, Chiara Bracco, Elisabeth Renner, Federico Roncarolo, Piotr Skowronski, Andrea Calia, and many more experts of the field, which was fundamental for the work presented in this thesis. I want to thank all of these colleagues.

Life inside and outside of work would not have been that pleasant without friends, for whom I am very grateful. To 'buildings 6, 9 and 10': Natalia, Kostas, Sofia, Elena F., Elena G., Kyriacos, Michael, Matteo, Alex, Elle, Ingrid, Chiara, Despoina, Michalis and Lorenzo, thank you for creating a fun atmosphere in the corridors and the cafeteria. To my 'crew': Chris, Manos, Maggie, Olga, Stergios and Thenia, thank you for the countless fun memories. To my 'local' friends: Stamatis, Vasilis, Katerina, Kacper, Irini, Noshin, Alina, and to my 'distant' friends: Angelos, Athina, Spyros, Dimitris,

Panagiota, Pinelopi, Christina, and Christos, thank you for filling the past three years with so many happy moments.

Finally, I want to express my gratitude to my family, Petrit, Tone and Tiona. They always remind me what is important in life through their endless love and support.

Extended Summary

The CERN Proton Synchrotron Booster (PSB) is a circular synchrotron consisting of four identical superimposed rings that accelerate protons from an energy of 160 MeV up to 2 GeV. Within the CERN Accelerator Complex, the PSB lies between the Linac4 (L4) and the Proton Synchrotron (PS) and it delivers high-intensity beams for fixed target experiments and high-brightness beams for collisions at the Large Hadron Collider (LHC). The performance of the PSB is limited mainly by the space charge effects that the beams suffer at low energies. Above a certain beam intensity, the space charge tune spread at injection can reach values above $\Delta Q_{x,y}^{SC} = -0.5$ and thus particles can interact with the resonances at the integer tunes $Q_{x,y} = 4.0$. The systematic resonances $4Q_{x,y} = 16$ are strongly excited by the space charge potential due to the lattice periodicity of 16 in combination with all other random field errors. The modulation of the space charge detuning of bunched beams leads to the periodic resonance crossing of the integer resonances which causes an emittance growth and reduces the beam brightness. The beam brightness that the LHC injectors deliver, is of fundamental importance since it contributes to the luminosity, and eventually to the collision rate, of the LHC beams.

To mitigate these effects, the PSB underwent major upgrades in the framework of the LHC Injectors Upgrade (LIU) project. The LIU project aimed to upgrade not only the PSB but the whole LHC injector chain in order to fulfil the High-Luminosity LHC project's beam requirements. For the PSB, the LIU consisted of upgrading the injection transfer line and the injection sector, for the connection with the Linac4 (L4), as well as upgrades in the rings and extraction transfer line. The L4 delivers H^- at an increased energy of 160 MeV, compared to its predecessor, Linac2, which delivered protons at an energy of 50 MeV. The increase of the injection energy reduces the space charge effects and allows production of beams with a larger intensity for similar transverse emittances and space charge detuning.

For converting the H^- ions to protons, the multi-turn injection was replaced by a charge-exchange injection system. This consists of a horizontal chicane and a thin stripping foil that strips the electrons from the H^- atoms. The chicane is created by a set of four, short, pulsed, dipole chicane magnets (BSWs) and after the injection has finished it decays over 5 ms (or approximately 5000 beam revolutions). Strong quadrupolar field perturbations are induced by the BSWs in the vertical plane through the edge focusing and the eddy currents. These perturbations cause optics distortions in the form of β-beating and tune-shifts. The operation of the machine close to the vertical

half-integer resonance $2Q_y = 9$, to avoid beam degradation due to the integer resonances, enhances considerably these optics distortions (for example the maximum β-beating can exceed 200 %) which can eventually lead to beam loss and degrade the machine performance. The control of the β-function as a machine property is fundamental for any synchrotron since it dictates the particle motion in the transverse planes, the betatron tunes, the beam size and consequently the beam losses, emittance and brightness. This task is particularly challenging for the PSB in which the source of these perturbations dynamically changes over a short period of time, as the injection chicane collapses.

During 2020, before the restart of the upgraded PSB, a method for measuring and correcting the optics distortions induced by the injection chicane were developed. This consisted of measuring the local β-distortions at two individually powered defocusing quadrupoles using k-modulation and then interpolating them to a model-based response matrix. The use of a response matrix is possible due to the fact that the source of the focusing errors is localized (at the injection region). The method was entirely simulated in MAD-X and worked very well as it was able to dynamically correct, nearly perfectly, the β-beating for a wide range of working points.

The robustness and effectiveness of the k-modulation-based correction method was tested extensively before the 2021 beam commissioning using MAD-X and Py-ORBIT simulations. Uncertainties that are expected to be present in the real machine, such as the accurate determination of the tune, random focusing errors, and space charge effects, were taken into account and studied in detail. Still, the method proved to be reliable and was expected to reduce the β-beating to at least below 6 % which was considered acceptable for the LIU brightness targets.

The measurement and correction of the optics distortions at injection was implemented into an operational GUI application and was used in the 2021 and 2022 beam commissioning. After overcoming many technical challenges, the measurement of the β-beating and tune was performed during the collapse of the injection chicane for the working point of $(Q_x, Q_y) = (4.39, 4.44)$. The agreement between the expected and the measured distortion in the optics was excellent which suggests that the modelling of the injection chicane error sources and the machine lattice is very good. The dynamic correction was calculated and applied in the PSB which resulted in bringing the β-beating from values above 30 % to values below 3 %. The measurements of 2022 were similar.

The minimization of the optics distortions at injection allows the stable operation of the beams with higher working points closer to the half-integer resonance, i.e. further away from the integer resonances. These working points are not accessible without the dynamic correction of the β-beating, as the beam is fully lost almost immediately. By injecting further away from the integer resonances, the emittance growth induced by the periodic resonance crossing becomes weaker. Thus, the transverse emittances become smaller for the same beam intensity. This contributed in an increased beam brightness at extraction of the PSB that exceeded the targets of the LIU project. This achievement not only represents the success of the LIU upgrades but also shows how good is the understanding and modelling of the accelerator.

An important aspect of the brightness optimization is the measurement and anal-

ysis of the transverse beam shapes. The particle distribution shape in the transverse planes plays a critical role in computing both the beam emittance and, ultimately, the beam brightness. Generally, the particle distributions are modelled with Gaussian functions but in some cases, like in the PSB, these distributions might slightly differ from a Gaussian. Observations of overpopulated beam tails, mostly in the vertical plane, have been made both at injection and at extraction energies of the PSB. The modelling of the non-Gaussian beam tails was done with a generalized Gaussian function known as q-Gaussian. The q-Gaussian distribution incorporates a parameter 'q' to model the weight of the distribution's tails. Overpopulated beam tails can lead to beam losses in the downstream machines of the accelerator complex and eventually reduce the beam brightness. To explore potential causes of beam tail enhancement and ultimately enhance the quality of delivered beams, a measurement campaign was launched.

The beam profile measurements evolved on two fronts. A significant part of the studies was dedicated in the way the profiles are reconstructed with the available instrumentation. The transverse beam profiles are assessed with a Wire Scanner (WS) which consists of a thin rotating wire that intercepts the beam particles over thousands of revolutions. The beam-wire interaction generates secondary particles that create a detectable signal proportional to the local density of the particles in the plane of rotation. However, it is known from previous studies that the beam-wire interaction induces also scattering effects to the beam that affect the particle distribution and emittance. Within this thesis, a simulation model of the WS measurement was implemented to reproduce the effects of the WS scattering on the beam. The parameters of this model were calibrated using real profile measurements which provided a method for estimating the actual wire width and scattering angle. This model was then used to extract qualitative and quantitative results on the behaviour of the beam core (in terms of emittance growth) and the beam tails (in terms of enhancement of depression of the tail population) during the WS measurement, which explained the experimental observations. With the use of this simulation model and the q-Gaussian function, new techniques were established to account and remove the scattering effects of the beam-wire interaction, which resulted in improved reconstructions of the measured profiles.

The second part of the profile studies was dedicated in the interplay of space charge and third and fourth order resonances and how this can affect the particle distribution along the cycle of the PSB. The beam profiles were characterized for different working points, beam intensities and beam energies and the tail formation mechanisms were associated in most cases with the periodic resonance crossing induced by the space charge detuning. Means for reducing the tail population and optimizing the beam accumulation were considered in terms of modification in the tune evolution along the cycle. The horizontal particle distributions were addressed separately due to the non-zero dispersion present in the PSB. The treatment of the horizontal profiles requires the use of dispersion deconvolution algorithms and so indirect estimations of the horizontal beam tails were done.

The improved beam brightness when correcting the injection chicane β-beating and injecting with higher working points, further away from the integer resonances, motivated

the study of the injection even above the half-integer resonance $2Q_y = 9$. In principle, such an injection could further minimize the interaction with the integer resonances, due to the space charge tune spread, and result to an even larger brightness. This triggered a series of studies that aimed to the characterization of all the space charge effects when being near and when dynamically crossing the half-integer resonance.

An almost perfect control of the vertical half-integer resonance $2Q_y = 9$ was achieved in the PSB. The resonance, that is naturally excited by machine imperfections, is compensated experimentally with the use of two families of quadrupole correctors that create orthogonal half-integer resonance driving terms. By scanning the strengths of the quadrupole correctors, a configuration can be found at which the driving term that the quadrupoles create cancels the unknown driving term of the half-integer resonance and thus compensate it. By deliberately degrading the compensating values of the quadrupole correctors' strengths, the resonance can be excited in a controlled way. A method for experimentally estimating the stopband width of the resonance for the different excitations, by means of transmission monitoring when dynamically crossing the resonance with different crossing speeds, was established. The stopband width estimations were in good agreement with analytical expectations.

The control of the half-integer resonance and the flexibility of the PSB to create a variety of different beam and machine conditions allowed the experimental study of many non-linear effects for the first time. The vertical beam profiles were measured with the WS during the adiabatic crossing of the half-integer resonance from above with a coasting beam. The profiles revealed the resonance island structure in the vertical phase space due to the space charge detuning and how these evolve towards larger transverse amplitudes while the beam crosses the resonance. The same process was reproduced in detail in tracking simulations. The particle trapping was studied for different space charge regimes and in the majority of cases the agreement between measurements and simulations is excellent. Other aspects of the particle trapping were also analyzed experimentally, such as the rotation of the vertical phase space structure while rotating the excitation driving term and also the re-merging of the particles of the resonance islands with the beam core.

The effects of the crossing speed, chromaticity and synchrotron motion were all studied independently but also combined. It was shown how for relatively slow crossing of the resonance the beam losses (due to the particle trapping) dominate, while when the crossing becomes faster the emittance blow-up dominates. The chromaticity induces an additional detuning that is not amplitude dependent and thus particles with a specific momentum offset will see the resonance islands at different transverse amplitudes. In this case, the population of the particles in the vertical phase space (or equivalently in the measured vertical profile) will not form around two distinct resonance islands but rather in a strip of particles that reaches the machine aperture. Finally, a bunched beam will perform synchrotron oscillations which induce a modulation in the space charge detuning of single particles. This results to periodic resonance crossing and to higher losses when dynamically crossing the half-integer resonance compared to a coasting beam.

The crossing of the half-integer resonance with tunes $Q_y < 4.5$ (crossing from below)

was also studied. In the case of a coasting beam and with compensated chromaticity, the resonance islands move from large transverse amplitudes towards the center, as the dynamic crossing from below progresses. This results to an emittance growth, as expected also from tracking simulations. A considerable beam transmission fluctuation was observed between between different shots when crossing from below under the same beam and machine conditions.

The characterization of the half-integer resonance effects are of operational interest for the PSB due to the possible brightness gain from injecting above the half-integer resonance. Under operational conditions in the PSB, the chromaticity is non-zero, the beams are bunched with a longitudinal shape that dynamically changes throughout the cycle, and also the space charge tune spread reduces while the beams are accelerated. The combination of these effects requires a very careful configuration of the working point at injection and its evolution along the cycle, for each beam intensity. The beam degradation during the half-integer crossing was minimized by revising the injection chicane induced perturbations and the half-integer resonance compensation. Multiple techniques were devised for the half-integer resonance compensation, that were not only based on the monitoring of the beam losses but also on the shape of the transverse beam distributions. The injection above and the dynamic crossing of the half-integer resonance under operational beam conditions was successfully performed experimentally with a measured beam brightness still exceeding the LIU targets. Although currently this is not used operationally, it was shown that the dynamic half-integer crossing is feasible with an excellent beam quality.

Overall, the major upgrades that the PSB underwent within the LIU project, brought new effects to study, challenges to overcome and new parameter regimes to explore. The studies that were performed pushed the performance of the PSB regarding the LHC beams in terms of brightness and the overall understanding of the machine. Furthermore, the experimental analysis of the space charge effects near the half-integer resonance go beyond the needs of the PSB as they can be beneficial for any high-brightness high-intensity accelerator.

Zusammenfassung

Der CERN Proton Synchrotron Booster (PSB) ist ein kreisförmiger Teilchenbeschleuniger, der aus vier identischen, übereinander angeordneten Ringen bestehtEr beschleunigt Protonen von einer kinetischen Energie von 160 MeV auf bis zu 2 GeV. Innerhalb des CERN-Beschleunigerkomplexes liegt der PSB zwischen dem Linac4 (L4) und dem Protonen-Synchrotron (PS) und liefert hochintensive Strahlen für Fixed-Target-Experimente und hochbrillante Strahlen für Kollisionen am Large Hadron Collider (LHC). Die Leistungsfähigkeit des PSB wird hauptsächlich durch Raumladungseffekte limitiert, denen die Strahlen bei niedrigen Energien ausgesetzt sind. Oberhalb einer bestimmten Strahlintensität kann die raumladungsbedingte Verschiebung des Arbeitspunktes ('Tune-Verschiebung', ΔQ) bei der Injektion Werte über $\Delta Q_{x,y}^{SC} = -0.5$ erreichen, sodass Teilchen auf Resonanzen bei den ganzzahligen Tunes $Q_{x,y} = 4.0$ treffen können. Diese systematischen Resonanzen ($4Q_{x,y} = 16$) werden durch das Raumladungspotential aufgrund der Gitterperiodizität des PSB von 16 in Kombination mit allen anderen zufälligen Feldfehlern stark angeregt. Die Modulation der raumladungsbedingten Tune-Verschiebung von gebündelten Strahlen führt dann zur periodischen Kreuzung der ganzzahligen Resonanzen und damit zu eiunem Anwachsen der Strahlemittanz, welches die Strahlbrillanz verringert. Die Strahlbrillanz, die die LHC-Injektoren liefern, ist von grundlegender Bedeutung, da sie zur Luminosität und schließlich zur Kollisionsrate der LHC-Strahlen beiträgt.

Um diese Auswirkungen abzuschwächen, wurde der PSB im Rahmen des LHC Injectors Upgrade (LIU)-Projekts umfassend modernisiert. Ziel des LIU-Projekts war es, die Leistungsfähigkeit nicht nur des PSB, sondern der gesamten LHC-Injektorkette zu erhöhen, um die Anforderungen des LHC-Projekts an Intensität und Strahlbrillanz zu erfüllen. Für den PSB umfasste das LIU-Projekt die Modernisierung der Injektions-Transferlinie und des Injektionsbereiches für den Anschluss an den Linac4 (L4), sowie die Modernisierung des eigentlichen Beschleunigers und der Extraktions-Transferlinie. Der L4 liefert H^--Ionen mit einer Energie von 160 MeV, verglichen mit seinem Vorgänger Linac2, der Protonen mit einer Energie von 50 MeV lieferte. Die Erhöhung der Injektionsenergie reduziert die Raumladungseffekte und ermöglicht die Erzeugung von Strahlen mit größerer Intensität bei ähnlichen transversalen Emittanzen und raumladungsbedingter Tune-Verschiebung.

Für die Umwandlung der H^--Ionen in Protonen wurde die bisherige Multiturn-Injektion durch ein Ladungsaustausch-Injektionssystem ersetzt. Dieses besteht aus einer

horizontalen gepulsten Orbitauslenkumg ("Schikane") und einer dünnen Kohlenstoff-Folie (Stripping foil), die die Elektronen von den H^--Ionen abtrennt. Die Schikane wird von vier kurzen, gepulsten Dipol-Magneten (BSWs) während der Injektion erzeugt, sodass der injizierte Strahl für die Dauer von 5 ms (oder etwa 5000 Strahlumläufen) die Folie passiert. Im Verlauf dieser Orbitverschiebung werden starke quadrupolare Feldstörungen von den BSWs in der vertikalen Ebene durch Kantenfokussierung und Wirbel-ströme induziert. Diese Störungen verursachen Fehler in der Strahloptik, ausgedrückt als relativer Fehler der optischen Funktion $\Delta\beta/\beta$, sog. β-Beating, und Verschiebungen des Arbeitspunktes, ΔQ, in beiden transversalen Ebenen. Der Betrieb der Maschine in der Nähe der vertikalen halbzahligen Resonanz $2Q_y = 9$ zur Vermeidung der ganzzahligen Resonanzen verstärkt diese optischen Fehler erheblich (beispielsweise kann das maximale β-Beating 200 % überschreiten), was schließlich zu Strahlverlusten und einer Verschlechterung der Strahlqualität führen kann. Die Kontrolle der β-Funktion ist für jedes Synchrotron von grundlegender Bedeutung, da sie die Teilchenbewegung in den transversalen Ebenen, den Arbeitspunkt der Maschine, die Strahlgröße und folglich die Strahlverluste, die Emittanz und die Strahlbrillanz bestimmt. Diese Aufgabe ist für den PSB eine besondere Herausforderung, da sich diese Störungen innerhalb kurzer Zeit dynamisch verändern, wenn die Amplitude der Injektionsbeule nach erfolgter Injektion wieder zurückgesetzt wird.

Im Jahr 2020, vor der Wiederinbetriebnahme des modernisierten PSB, wurde eine Methode zur Messung und Korrektur der durch die Injektions-Orbitbeule verursachten optischen Fehler entwickelt. Dazu wurden die lokalen β-Funktionen an zwei einzeln betriebenen defokussierenden Quadrupolen mittels k-Modulation gemessen und anschließend zu einer modellbasierten Antwortmatrix interpoliert. Die Verwendung einer Antwortmatrix ist möglich, da die Quelle der Fokussierungsfehler lokalisiert ist (d.h. im Bereich der Strahlinjektion liegt). Die Methode wurde vollständig in MAD-X simuliert und funktionierte sehr gut, da sie in der Lage war, den optischen Fehler $\Delta\beta/\beta$ für einen breiten Bereich von Arbeitspunkten dynamisch und nahezu perfekt zu korrigieren.

Die Robustheit und Effektivität der k-modulationsbasierten Korrekturmethode wurde vor der Inbetriebnahme des Strahls im Jahr 2021 mit Hilfe von MAD-X- und Py-ORBIT-Simulationen ausgiebig getestet. Dabei wurden Unsicherheiten, die in der realen Anlage zu erwarten sind, wie die genaue Bestimmung des Tune, zufällige Fokussierungsfehler und Raumladungseffekte berücksichtigt und eingehend untersucht. Die Methode erwies sich als zuverlässig und sollte den relativen Fehler der β-Funktion auf unter 6 % reduzieren, was im Rahmen der LIU-Brillanzziele als akzeptabel befunden wurde.

Die Messung und Korrektur der optischen Verzerrungen bei der Injektion wurde in eine operationelle GUI-Anwendung implementiert und bei der Strahlinbetriebnahme 2021 und 2022 eingesetzt. Nach Überwindung einiger technischer Herausforderungen wurde die Messung der β-Funktion und deren Abweichung während der Reduktion der Injektionsbeule für den Arbeitspunkt $(Q_x, Q_y) = (4.39, 4.44)$ durchgeführt. Die Übereinstimmung zwischen erwartetem und gemessenem Optikfehler war ausgezeichnet, was darauf schließen lässt, dass die Modellierung der Fehlerquellen des Injektionsschemas und der Maschine sehr gut ist. Die dynamische Korrektur wurde berechnet und im PSB

angewandt, sodass der relative Fehler der β-Funktion von Werten über $\Delta\beta/\beta = 30\%$ auf Werte unter 3 % gebracht wurde. Die Messungen des Jahres 2022 waren ähnlich.

Die Minimierung der optischen Fehler bei der Injektion ermöglicht den stabilen Betrieb der Strahlen mit Arbeitspunkten näher an der halbzahligen Resonanz, d.h. weiter entfernt von den ganzzahligen Resonanzen. Diese Arbeitspunkte sind ohne die dynamische Korrektur des β-Beatings nicht erreichbar, da der Strahl fast vollständig verloren geht. Durch die Injektion in größerer Entfernung von den ganzzahligen Resonanzen wird das durch die periodische Kreuzung von Resonanzen induzierte Emittanzwachstum abgeschwächt. Somit bleiben die transversalen Emittanzen bei gleicher Strahlintensität kleiner. Dies trägt zu einer erhöhten Strahlbrillanz bei der Extraktion aus dem PSB bei. Die Ziele des LIU-Projekts konnten somit sogar übertroffen werden. Diese Leistung stellt nicht nur den Erfolg des LIU-Projects dar, sondern zeigt auch, wie gut das Verständnis und die Modellierung des Beschleunigers ist.

Ein wichtiger Aspekt der Brillanzoptimierung ist die Messung und Analyse der transversalen Strahldimension. Die Form der Teilchenverteilung in den transversalen Ebenen spielt eine entscheidende Rolle bei der Berechnung der Strahlemittanz und letztlich der Strahlbrillanz. Im Allgemeinen werden die Teilchenverteilungen mit Gaußfunktionen modelliert, aber in einigen Fällen, so wie beim PSB, können diese Verteilungen leicht von einer idealen Gaußform abweichen. Sowohl bei der Injektion als auch bei den Extraktionsenergien des PSB wurden starke Ausläufer der Teilchendistribution, meist in der vertikalen Ebene, beobachtet. Die Modellierung der nicht-gaußschen Ausläufer erfolgte mit einer verallgemeinerten Gaußschen Funktion, der so genannten q-Gaußschen Funktion. Die q-Gauß-Verteilung enthält einen Parameter ‘q’ zur Modellierung der Ausläufer. Verstärkte Ausläufer der Teilchendistribution können zu Strahlverlusten in den nachgeschalteten Maschinen des Beschleunigerkomplexes führen und schließlich die Strahlbrillanz verringern. Um mögliche Ursachen für die Verstärkung der Ausläufer zu untersuchen und letztlich die Qualität der gelieferten Strahlen zu verbessern, wurde eine Messreihe gestartet.

Die Messungen der Strahlprofile entwickelten sich an zwei Fronten. Ein wesentlicher Teil der Studien war der Art und Weise gewidmet, wie die Profile mit den verfügbaren Instrumenten rekonstruiert werden. Die transversalen Strahlprofile werden mit einem Wire Scanner (WS) gemessen, der aus einem dünnen rotierenden Draht besteht und der die Strahlteilchen über Tausende von Umläufen durchkreuzt. Die Strahl-Draht-Wechselwirkung erzeugt Sekundärteilchen, die ein messbares Signal darstellen, das proportional zur lokalen Dichte der Teilchendistribution in der Rotationsebene ist. Aus früheren Studien ist jedoch bekannt, dass die Strahl-Draht-Wechselwirkung auch zu Streueffekten des Strahls führt, die die Teilchenverteilung und die Emittanz beeinflussen. In dieser Arbeit wurde ein Simulationsmodell der WS-Messung implementiert, um die Auswirkungen der WS-Streuung auf den Strahl zu reproduzieren. Die Parameter dieses Modells wurden anhand realer Profilmessungen kalibriert, was eine Schätzung der tatsächlichen Drahtbreite und des Streuwinkels ermöglichte. Dieses Modell wurde verwendet, um qualitative und quantitative Ergebnisse über das Verhalten des Strahlkerns (in Bezug auf den Anstieg der Emittanz) und der Strahlausläufer (in Bezug

auf deren Rekuktion) während der WS-Messung zu erhalten, die die experimentellen Beobachtungen erklären. Mit Hilfe dieses Simulationsmodells und der q-Gauß'schen Funktion wurden neue Techniken entwickelt, um die Streuungseffekte der Strahl-Draht-Wechselwirkung zu berücksichtigen und zu korrigieren, was zu verbesserten Rekonstruktionen der gemessenen Profile führte.

Der zweite Teil der Profilstudien widmete sich dem Zusammenspiel von Raumladung und Resonanzen dritter und vierter Ordnung und der Frage, wie sich dies auf die Teilchenverteilung entlang des Zyklus des PSB auswirken kann. Die Strahlprofile wurden für verschiedene Arbeitspunkte, Strahlintensitäten und Strahlenergien charakterisiert, und die Mechanismen der Bildung von Strahlausläufern wurden in den meisten Fällen mit der periodischen Resonanzkreuzung in Verbindung gebracht, die aufgrund der Raumladungs-bedingten Tune-Verschiebung induziert wird. Verfahren zur Reduzierung der Strahlausläufer und zur Optimierung der Strahlakkumulation wurden in Form von Modifikationen der Tune-Funktion entlang des Zyklus untersucht. Die horizontalen Teilchenverteilungen wurden aufgrund der Dispersions-Funktion im PSB gesondert betrachtet. Die Behandlung der horizontalen Profile erfordert den Einsatz von Algorithmen zur Dekonvolution der Dispersions-Funktion, sodass indirekte Schätzungen der horizontalen Strahlausläufer vorgenommen wurden.

Die verbesserte Strahlbrillanz bei der Korrektur des durch die Injektions-schikane verursachten Optik Fehlers, , sowie die dadurch ermöglichte Injektion mit höheren Arbeitspunkten, weiter entfernt von den ganzzahligen Resonanzen, motivierte die Untersuchung der Injektion auch oberhalb der halbzahligen Resonanz $2Q_y = 9$. Im Prinzip könnte eine solche Injektion die Wechselwirkung mit den ganzzahligen Resonanzen aufgrund der raumladungsbedingten Tune-Verschiebung weiter minimieren und zu einer noch größeren Strahlbrillanz führen. Dies war der Auslöser für eine Reihe von Studien, die auf die Charakterisierung der Raumladungseffekte in der Nähe und beim dynamischen Durchqueren der halbzahligen Resonanz abzielten.

Eine nahezu perfekte Kontrolle der vertikalen halbzahligen Resonanz $2Q_y = 9$ wurde im PSB erreicht. Die Resonanz, die normalerweise durch Unvollkommenheiten der Maschine angeregt wird, wurde experimentell durch den Einsatz von zwei Familien von Quadrupolkorrektoren kompensiert, die orthogonale halbzahlige Resonanz-Terme erzeugen. Durch systematisches Variieren der Quadrupolkorrektoren konnte eine Konfiguration gefunden werden, bei der der von den Quadrupolen erzeugte Term den unbekannten Treiber der halbzahligen Resonanz aufhebt und dessen Effekt somit kompensiert. Durch gezielte Verschlechterung der Kompensationswerte der Quadrupolkorrektoren kann die Resonanz dann kontrolliert angeregt werden. Desweiteren wurde eine Methode zur experimentellen Abschätzung der Stoppbandbreite der Resonanz für die verschiedenen Anregungen mittels Transmissionsmessungen beim dynamischen Durchqueren der Resonanz mit unterschiedlichen Durchquerungsgeschwindigkeiten entwickelt. Die Abschätzungen der Stoppbandbreite stimmten gut mit den analytischen Erwartungen überein.

Die Kontrolle der halbzahligen Resonanz und die Flexibilität des PSB, eine Vielzahl unterschiedlicher Strahl- und Maschinenbedingungen zu erzeugen, ermöglichten erstmals die experimentelle Untersuchung vieler nichtlinearer Effekte. Die vertikalen Strahlprofile

wurden mit dem WS während der adiabatischen Durchquerung der halbzahligen Resonanz von oben mit einem longitudinal ungebündelten, d.h. gleichstrom-artigen Strahl gemessen. Die Profile zeigten die Struktur der Resonanzinseln im vertikalen Phasenraum, die auf die Tune-Verschiebung durch die Raumladung zurückzuführen ist, und wie sich diese zu größeren transversalen Amplituden entwickeln, während der Strahl die Resonanz durchquert. Derselbe Prozess wurde in Simulationen zur Berechnung der Teilchenbahnen (Tracking-calculations) im Detail reproduziert. Der Teilcheneinfang in der Resonanz wurde für verschiedene Raumladungsregimes untersucht, und in den meisten Fällen ist die Übereinstimmung zwischen Messungen und Simulationen ausgezeichnet. Andere Aspekte des Teilcheneinfangs in der Nähe der Resonanz wurden ebenfalls experimentell analysiert, wie z.B. die Rotation der vertikalen Phasenraumstruktur während der Rotation des anregenden Terms und auch die Wiedervermischung der Teilchen der Resonanzinseln mit dem Strahlkern.

Die Auswirkungen der Überquerungsgeschwindigkeit, der Chromatizität und der Synchrotronbewegung auf die Strahlqualität wurden unabhängig voneinander als auch in ihrem Zusammenwirken untersucht. Es wurde gezeigt, dass bei einer relativ langsamen Überquerung der Resonanz die Strahlverluste (aufgrund des Teilcheneinfangs) dominieren, während bei einer schnelleren Überquerung die Aufblähung der Emittanz überwiegt. Die Chromatizität führt zu einer zusätzlichen Tune-Verschiebung, die nicht amplitudenabhängig ist, sodass Teilchen mit einer bestimmten Impulsabweichung die Resonanzinseln mit unter-schiedlichen transversalen Schwingungs-Amplituden sehen. In diesem Fall bildet sich die Teilchenpopulation im vertikalen Phasenraum aus (bzw. im gemessenen vertikalen Profil) nicht um zwei getrennte Resonanzinseln herum, sondern in einem Streifen von Teilchen, der die Maschinenakzeptanz erreicht. Schließlich führt ein longitudinal gebündelter Strahl Synchrotronschwingungen aus, die eine Modulation in der Tune-Verschiebung der einzelnen Teilchen bewirken. Dies führt zu periodischen Resonanzüberquerungen und zu höheren Verlusten beim dynamischen Überqueren der halbzahligen Resonanz im Vergleich zu einem gleichstromartigen, ungebündeltem Strahl.

Das Kreuzen der halbzahligen Resonanz mit Tunes $Q_y < 4.5$ (Kreuzen von unten) wurde ebenfalls untersucht. Im Falle eines ungebündelten Strahls und mit kompensierter Chromatizität bewegen sich die Resonanzinseln von großen transversalen Amplituden zur Mitte hin, wenn die dynamische Kreuzung von unten geschieht. Dies führt zu einem Anstieg der Emittanz, wie es auch von Tracking-Simulationen erwartet wird. Eine erhebliche Schwankung der Strahltransmission wurde bei der Überquerung von unten unter denselben Strahl- und Maschinenbedingungen beobachtet.

Die Charakterisierung der Resonanzeffekte in der Nähe der halbzahligen Resonanz ist für den PSB von erheblichem Interesse, da durch die Injektion oberhalb der Halbzahl-Resonanz ein Brillanzgewinn möglich ist. Unter den Betriebsbedingungen des PSB ist die Chromatizität ungleich Null, die longitudinale Form der Strahlen ändert sich während des Zyklus dynamisch, und auch die Tune-Verschiebung durch die Raumladung nimmt ab während die Strahlen beschleunigt werden. Die Kombination dieser Effekte erfordert eine sehr sorgfältige Konfiguration des Arbeitspunkts bei der Injektion und während des Zyklus für jede Strahlintensität. Die Verschlechterung der Strahlqualität während

der Überquerung der halbzahligen Resonanz wurde durch Überarbeitung der durch die Injektions-Orbitbeule verursachten Störungen und der halbzahligen Resonanzkompensation minimiert. Für die halbzahlige Resonanzkompensation wurden mehrere Techniken entwickelt, die nicht nur auf der Messung der Strahlverluste, sondern auch auf der Form der transversalen Strahlverteilungen basieren. Die Injektion oberhalb und das dynamische Kreuzen der halbzahligen Resonanz unter operativen Strahlbedingungen wurde erfolgreich experimentell durchgeführt, wobei die gemessene Strahlbrillanz die LIU-Ziele übertraf. Obwohl dies derzeit nicht operationell genutzt wird, konnte gezeigt werden, dass die dynamische Überquerung der Halbzahlresonanz mit einer hervorragenden Strahlqualität möglich ist.

Insgesamt brachten die umfangreichen Verbesserungen, denen der PSB im Rahmen des LIU-Projekts unterzogen wurde, neue zu untersuchende Effekte, zu bewältigende Herausforderungen und neue zu erforschende Parameterbereiche. Die durchgeführten Studien haben die Leistung des PSB für die LHC-Strahlen in Bezug auf die Strahlbrillanz und das allgemeine Verständnis der Maschine verbessert. Darüber hinaus geht die experimentelle Analyse der Raumladungseffekte in der Nähe der halbzahligen Resonanz über die Anwendung im PSB hinaus, da sie für jeden Beschleuniger mit hoher Strahlbrillanz und hoher Intensität von Nutzen sein kann.

Contents

List of Figures

List of Tables

Nomenclature

Abbreviations

BBQ	Base-Band Tune pickup
BCT	Beam Current Transformer
LHC	Large Hadron Collider
LIU	LHC Injectors Upgrade project
PSB	Proton Synchrotron Booster
RMS	Root Mean Square
SC	Space Charge
WP	Working Point
WS	Wire Scanner

Physical Constants

ϵ_0	Electric permittivity in vacuum	$8.854\,188 \times 10^{-12}\,\mathrm{Fm}^{-1}$
μ_0	Magnetic permeability in vacuum	$1.256\,637 \times 10^{-6}\,\mathrm{NA}^{-2}$
c	Speed of light in a vacuum	$299\,792\,458\,\mathrm{m\,s}^{-1}$
e	Elementary charge	$1.602\,177 \times 10^{-19}\,\mathrm{C}$
m_e	Electron mass	$9.109\,384 \times 10^{-31}\,\mathrm{kg}$
$m_u c^2$	Atomic mass constant energy equivalent	$931.494\,102\,\mathrm{MeV}$
m_u	Atomic Mass Constant	$1.660\,539 \times 10^{-27}\,\mathrm{kg}$
p_e	Proton mass	$1.672\,622 \times 10^{-27}\,\mathrm{kg}$
r_e	Classical electron radius	$2.817\,940 \times 10^{-15}\,\mathrm{m}$

PSB Parameters

τ_c	Magnetic cycle time	1.2 s
C_{PSB}	Circumference	157.08 m
L_p	Period length	9.82 m
R_{PSB}	Radius	25 m

Symbols

α, β, γ Twiss parameters

β_r, γ_r Relativistic factors

$\delta Q_x^{SC}, \delta Q_y^{SC}$ Horizontal and vertical tune spread from space charge

ϵ_x, ϵ_y Horizontal and vertical normalized emittances

$\epsilon_{x,g}, \epsilon_{y,g}$ Horizontal and vertical geometrical emittances

$\frac{\delta p}{p}$ RMS momentum spread

θ_x, θ_y Orbital angle

ξ_x, ξ_y Horizontal and vertical normalized linear chromaticity

D_x, D_y Horizontal and vertical linear dispersion

f_{rev}, T_{rev} Revolution frequency and period

J_x, J_y, ϕ_x, ϕ_y Action-angle variables

N_b Beam intensity

Q_x, Q_y Horizontal and vertical betatronic tunes

$Q_x^{'}, Q_y^{'}$ Horizontal and vertical linear chromaticity

Chapter 1

Introduction

In particle physics research, a considerable amount of discoveries were made by colliding particles. Colliding particle beams at high energies create the conditions for studying the dynamics and structure of matter, and even for the formation of new particles. For this purpose, in the early 20^{th}-century, physicists and engineers started building machines that accelerate charged particles, namely particle accelerators. The size, design and performance between the different particle accelerators can vary significantly. However, the majority of them rely on electromagnetic fields for accelerating and controlling the beams. Particle accelerators are not only used for particle and nuclear physics research, but also in material science, industry, medical imaging and radiotherapy, etc.

1.1 The CERN Accelerator Complex

Currently the largest particle physics laboratory is operated by the European Organization of Nuclear Research (CERN) [1] and is located between the Franco-Swiss border, near Geneva. CERN is home to the Large Hadron Collider (LHC) [2], the world's largest accelerator. The LHC is a circular particle collider with 27 km circumference and it accelerates particles to energies up to 6.8 TeV. At the LHC, two different particle beams travel nearly to the speed of light in opposite directions and collide at four different points around the machine. These points are called interaction points and they house highly sophisticated particle detectors: ATLAS, CMS, ALICE and LHCb. These detectors identify and track the particles that are produced by the beam collisions.

The LHC is one out of the currently eight operating accelerators at CERN. Besides the LHC, there are four other circular accelerators: the Proton Synchrotron Booster (PSB), the Proton Synchrotron (PS), the Super Proton Synchrotron (SPS) and the Low Energy Ion Ring (LEIR), that can accelerate protons and/or ions. The remaining three accelerate particles in a straight line (linear accelerators). They consist of Linac4 (L4) that accelerates negative hydrogen ions (H^-), Linac3 (L3) that accelerates lead ions and the CERN Linear Electron Accelerator for Research (CLEAR) that accelerates electrons. Finally, CERN hosts two particle decelerators that decrease the speed and the energy of the particles: the Antiproton Decelerator (AD) and the Extra Low ENergy Antipro-

ton (ELENA) decelerator that both operate with antiprotons. The network of all the CERN accelerators and the way they are coupled to each other is called the CERN Accelerator Complex and is illustrated in Figure 1.1.

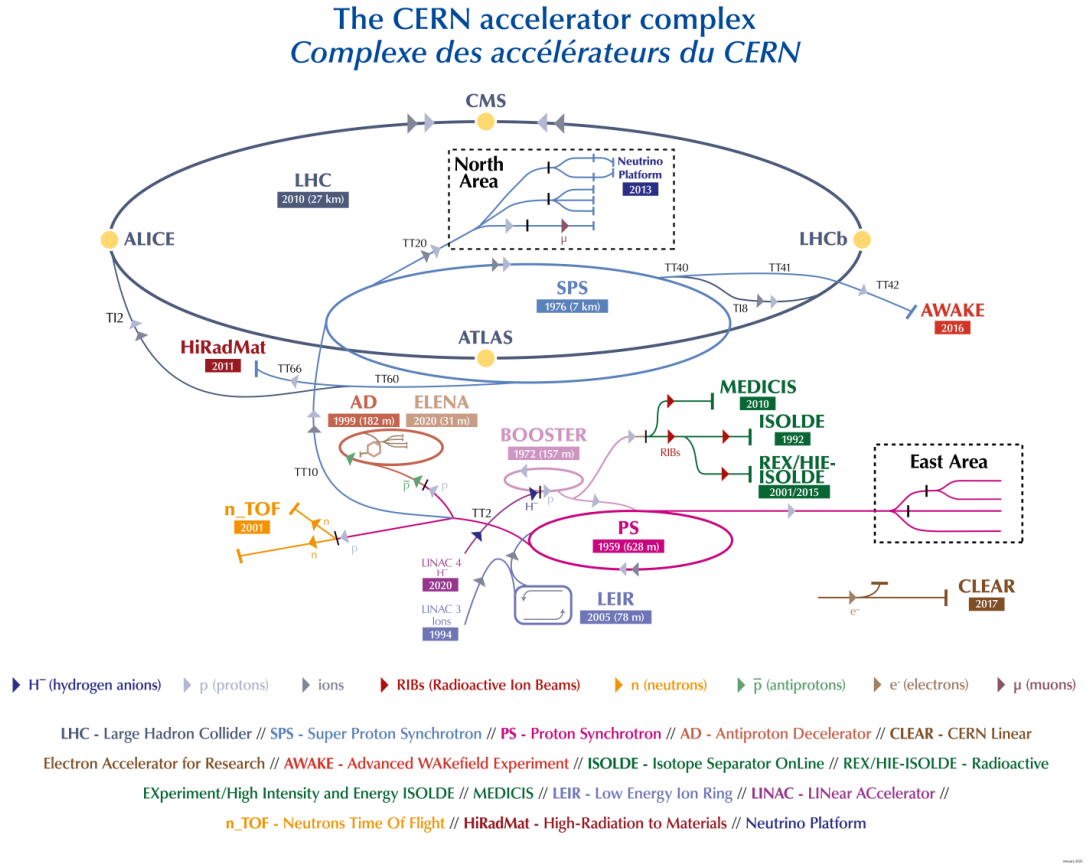

Figure 1.1: A schematic of the accelerator complex at CERN.

The different beams of the accelerator complex are either used as injection to increasingly higher energy accelerators, and end up colliding at the LHC, or are sent to various experimental areas for lower energy fixed target experiments. For example, the protons that end up in the LHC start from L4 as H^- ions and are accelerated to a kinetic energy of 160 MeV. These particles are then injected into the PSB, at the injection of which the electrons are stripped from the H^- ions converting them to protons. The PSB increases their energy to 2 GeV. Afterwards, the beam travels through the PS, where it reaches an energy of 25 GeV, followed by the SPS which accelerates them up to 450 GeV. Ultimately, the protons are injected into the LHC. The ions follow a similar path, only that instead of L4 and PSB the ions start from L3 and LEIR, respectively. At the lower energy experiments the beam particles collide with fixed targets at various energies. The fixed target experiments include the Online Isotope Mass Separator (ISOLDE), the

neutron Time-Of-Flight (nTOF) etc.

The focus of this study will be on the Proton Synchrotron Booster. The PSB was built between 1968-1972 and received its first beams on the 26th of May 1972. The machine center was placed exactly between the border of France and Switzerland. PSB has a unique design of four identical superimposed rings. The PSB lies between L4 and the PS and it only accelerates protons. Currently, the PSB can extract particles at an energy of either 1.6 GeV or 2 GeV. The only direct client of the PSB for fixed target experiments is ISOLDE.

1.2 LHC Injectors Upgrade Project

The first run of the LHC (Run 1) took place between 2009-2013. Following a two-year Long Shutdown 1 (LS1) between 2013-2015, the LHC restarted for Run 2 in 2015 until 2018 and then it was again shutdown for the Long Shutdown 2 (LS2). In 2022 the LHC restarted and is currently doing its third run (Run 3).

The High Luminocity LHC (HL-LHC) Project [3] aims at increasing the collision rate between the particles at the LHC during Run 4 by approximately a factor 10. The HL-LHC requires demanding beam characteristics at the injection of the LHC, exceeding the performance reach of the LHC injectors. To overcome the limitations in the injectors, the LHC Injectors Upgrade (LIU) Project [4] was initiated.

The LIU project aimed to upgrade the LHC injector chain in order to fulfill the HL-LHC beam requests. The upgrade included the proton and the ion injectors and it was successfully implemented during LS2. The project covers the replacement of Linac2 by Linac4, as well as major upgrades in the PSB, PS, SPS, Linac3 and LEIR. Currently, the project has been completed and all the machines have been re-commissioned. The performance ramp-up has been successfully completed in the PSB and the PS, while the gradual intensity ramp-up in the SPS is going according to plan until the end of Run 3.

1.3 Aim and Outline of the Thesis

Following the implementation of the LIU project, the PSB received several upgrades resulting in new effects to study, challenges to overcome and new parameter regimes to explore. The purpose of this thesis is to present the work performed for the optimization of the beam brightness performance of the PSB with the new H^- injection. The beam brightness incorporates the properties of the beam that the LHC injectors contribute to the luminosity, and eventually to the collision rate, of the LHC beams. The studies are focused mostly in the beam effects of the transverse planes, both near injection and later on in the cycle. These studies are a mixture of measurements (Machine Development (MD) studies), analytical calculations and computer simulations to evaluate and benchmark the modelling of the accelerator as a whole.

The work of this thesis is organized in the following way. Chapter 2 starts with an introduction of the PSB. At first, details regarding its layout, operation and beam instrumentation are presented. Then, the beam dynamics effects that are present in the

PSB and relevant for this study, like resonances and space charge, are briefly discussed. It is assumed that the reader is familiar with Accelerator Physics: only a few formulas that are relevant for this study are derived in the Appendix A. The chapter ends with the PSB upgrades in the context of LIU and the modelling of the PSB in simulation codes.

Chapter 3 is focused on the new injection scheme and the implications that it introduces. At first, the perturbations in the magnetic fields that are expected by the injection magnets are defined. The injection perturbations, in the form of tune distortions and β-beating, are strongly enhanced near the half-integer resonance and affect the brightness by means of losses and emittance growth. The simulation campaign that was performed in the context of this thesis in order to develop operational methods for dynamically compensating these perturbations is presented. Finally, the application of these methods to the actual machine after the LS2 are shown and the impact on the actual beam performance is demonstrated.

Chapter 4 deals with the quality of the beam distributions in the transverse planes and how they can be improved. The shape of the transverse beam distributions is very important not only for the assessment of the beam brightness but also for the clean transmission of the beams throughout the accelerator chain. The effects treated here extend also to the way the present instruments reconstruct the transverse beam profiles and how they impact the beam particles.

Chapters 5 and 6 explore what are the limits of the brightness performance of the PSB, beyond the LIU specifications. The subjects discussed in this chapter are twofold. On the one hand, means for operationally improving the PSB performance are attempted. On the other hand, these attempts drive studies that are of general academic interest for understanding fundamental beam dynamics effects, such as the particle trapping in the resonance islands in presence of space charge. The wide range of beam conditions accessible with the upgraded PSB with its new H^- charge exchange injection scheme allowed for a detailed experimental characterization of these effects.

Finally, the results of the work done in the context of this thesis are all summarized and reviewed in Chapter 7.

Chapter 2

Beam Dynamics in the PSB

This chapter describes the main components, operational aspects and relevant transverse beam dynamics of the Proton Synchrotron Booster. For an introduction to the fundamentals of Accelerator Physics the reader is referred to the classical textbooks of A. Wolski [5], H. Wiedemann [6] and S. Y. Lee [7] and the lectures of the CERN Accelerator School [8] and the Joint Universities Accelerator School [9].

2.1 Machine Layout and Beams

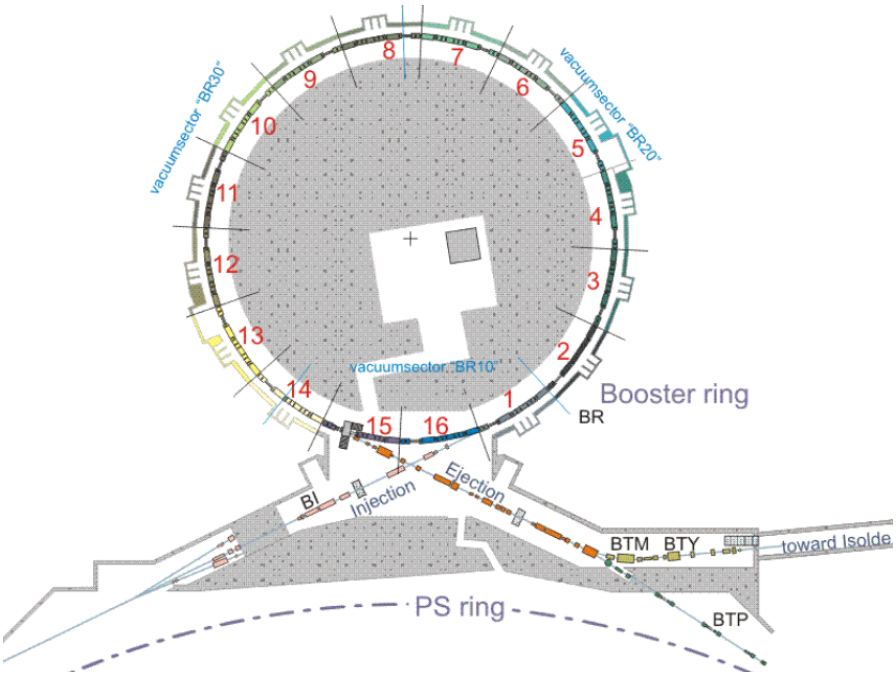

Figure 2.1: PSB layout (top view).

The Proton Synchrotron Booster (PSB) [10] consists of four identical superimposed rings of mean radius 25 m and a total circumference of 157.08 m. Each ring is composed of 16 periods (or sectors) of length 9.82 m. Each period consists of one straight section of length 2.65 m, two bending magnets and a quadrupole triplet of length 3.93 m. The layout of the PSB is shown in Figure 2.1 and of the second period in Figure 2.2.

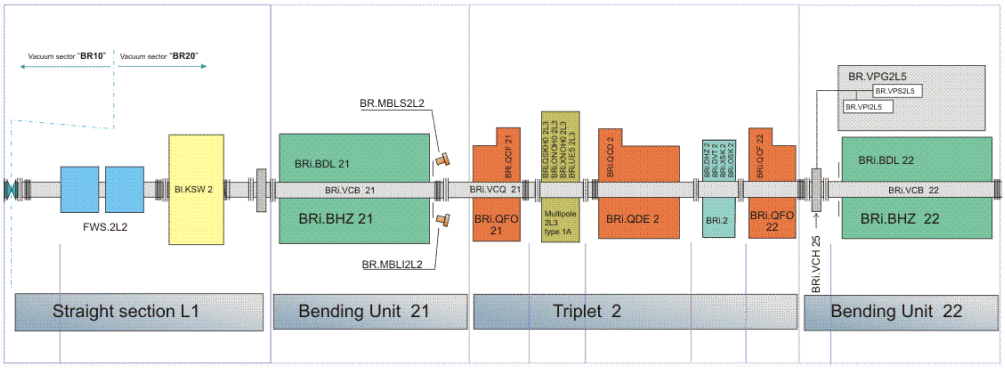

Figure 2.2: Layout of the PSB period (sector) 2.

Besides the main straight section, other smaller sections are available between the dipoles and the quadrupoles for additional magnets or devices. The different sections are denoted as n_1Ln_2, where n_1 represents the period number and n_2 the straight section number. For example, 2L1 corresponds to the main straight section at the second period of the PSB, while 4L2 corresponds to the second straight section (section between the first dipole and the first focusing quadrupole) at the fourth period of the PSB.

The dipoles have a length of 1.62 m and they cover approximately 33 % of the circumference, thus the bending radius is 8.24 m. Each quadrupole triplet consists of two focusing quadrupoles of length $l_{\mathrm{QFO}} = 0.504$ m each and one defocusing quadrupole of length $l_{\mathrm{QDE}} = 0.879$ m. In total, there are 128 focusing and 64 defocusing quadrupoles when considering all four PSB rings. It should be noted that the magnets have a common iron yoke for the four PSB rings, and thus trim windings are needed to control the magnet strengths for each ring individually.

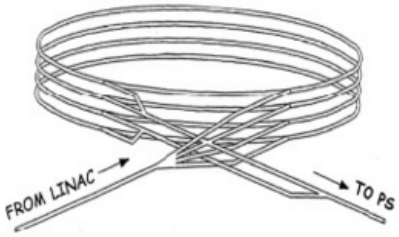

Figure 2.3: Schematic of the PSB injection and extraction.

There are three wideband Finement Radio-Frequency (RF) cavities in the PSB for capturing and accelerating the beams, installed in the 5th, 7th and 13th period [11]. Apart from acceleration, the cavities are used for bunch shaping, to produce longitudinally flatter beams (double or tripple harmonic), and for controlled longitudinal blow-up.

The PSB rings share a common injection and extraction line (Figure 2.3). The L4 beam is deflected vertically by a system that consists of five pulsed kicker magnets (vertical distributor), a vertical septum magnet and other vertical bending magnets [4],

in order to inject them to the four PSB rings respectively. This system splits and deflects the incoming beam to the right angles for entering the PSB rings. The incoming H^- ions are converted to protons by a charge-exchange system described in section 2.6. Each ring can be filled or not independently of the other rings. After the injection and acceleration in the PSB, the bunches are extracted and recombined by a system of kicker and septum magnets. The bunches are extracted over one turn.

The PSB is a relatively fast accelerator with a magnetic cycle of $\tau_c = 1.2\,\mathrm{s}$. The beam is injected at $t_{\mathrm{inj}} = 275\,\mathrm{ms}$ and is extracted at $t_{\mathrm{extr}} = 805\,\mathrm{ms}$ within the PSB cycle τ_c. During normal operation, the PSB is constantly cycled with different beams. The cycles follow a programmable super-cycle, which is repeated many times (pulse-by-pulse modulation). Table 2.1 summarizes the beam energy and relative parameters at injection and extraction of the PSB before and after the LIU upgrade. The revolution period at the new 160 MeV injection energy is usually approximated to 1 μs.

PSB parameters				
	Injection		Extraction	
	Pre-LIU	Post-LIU	Pre-LIU	Post-LIU
E_{kin} [GeV]	0.050	0.160	1.4	2.0
β_r	0.3140	0.5198	0.9160	0.9476
γ_r	1.053	1.171	2.492	3.132
f_{rev} [MHz]	0.5994	0.9920	1.748	1.809
T_{rev} [μs]	1.668	1.008	0.5720	0.5529

Table 2.1: PSB energy and relevant parameters at injection and extraction.

The PSB serves the different users with beams covering a large variety of intensities and emittances. There are two main beam classes: the high-intensity high-emittance beams that are used for fixed target experiments and the high-intensity low-emittance beams that are mostly sent to the PS to be eventually used for collisions in the LHC. Table 2.2 summarizes the most common beam types accelerated by the PSB.

PSB Beams						
Type	N_b [10^{10}ppb]	ϵ_x [μm]	ϵ_y [μm]	ϵ_δ [eVs]	h	Destination
LHC25	165	< 2.2	< 2.2	1.3	1	LHC
BCMS	85	< 1.2	< 1.2	0.9	1	LHC
EAST	170	$1-2$	$1-2$	< 1.3	1	East area (PS)
STAGISO	200-300	< 5	< 4	< 1.6	1	ISOLDE (PSB)
AD	400	9	5	1.3	1	AD (PS)
SFTPRO_MTE	< 600	$< 6-8$	< 4	< 1.3	2	North area (SPS)
NORMGPS/HRS	800	< 15	< 8	< 1.8	1	ISOLDE (PSB)
TOF	900	12	8	1.7	1	nTOF (PS)

Table 2.2: Common PSB beam types and typical parameters.

2.2 Beam Instrumentation

A number of measuring instruments and diagnostics are available in the PSB. The ones relevant for the studies of this thesis are briefly described in the following paragraphs.

2.2.1 Beam position monitors

Each PSB period contains one Beam Position Monitor (BPM) per ring [12]. BPMs allow the turn-by-turn measurement of the beam center of charge. The BPMs are based on the measurement of the voltage induced by the image current created by the passing beam on four electrodes, two placed horizontally and two vertically. From the induced signals, the transverse beam position can be reconstructed in a non-destructive way. The BPMs are placed between the first focusing quadrupole and the defocusing quadrupole (L3). In total, there are 64 BPMs in the PSB.

2.2.2 Beam intensity

The beam intensity is measured in the PSB using Beam Current Transformers (BCT) [13]. The BCTs consist of an AC transformer that measures the voltage induced by the magnetic field lines of the circulating beam. The BCTs operate in a limited frequency range that usually does not exceed a few hundreds of MHz. Each PSB ring contains one BCT at 8L1.

2.2.3 Beam profiles

The instrument to assess the transverse beam distributions and emittances in the PSB rings is the Wire Scanner (WS) [14]. A WS consists of a thin carbon wire that is connected to a rotating mechanical system. The wire physically rotates and crosses the beam during several turns with speeds of the order of a few tens of meters per second. The interaction of the wire with the charged particles creates a shower of secondary particles that are detected by multiple scintillators coupled to a photomultiplier. The photomultiplier creates an amplified current signal from which the transverse beam profile is reconstructed.

Until the end of Run 2, 8 wire scanners were located at the straight section of the second period (2L1), one for each ring and each plane (horizontal and vertical). During LS2, 8 additional wire scanners with an improved design (LIU-WS) [15, 16] were installed for each ring at 4L1 for the horizontal plane and at 11L1 for the vertical plane as part of the LIU project.

In the PSB, each wire scanner can perform the profile measurement twice within the cycle. In the first profile scan, the wire starts to rotate in an arc from its resting position, crosses the beam and reaches a temporary parking position. The first scan is referred as the ‘IN’ scan. After a programmable delay, typically around 200 ms, the wire rotates in the opposite direction with the same speed until it reaches its starting position. This second scan is referred to as the ‘OUT’ scan. With only a few exceptions, only profiles obtained from the IN scan will be shown in this thesis.

2.2.4 Tune measurement

The tune is measured by exciting a transverse oscillation of the beam with the transverse damper. Typically an excitation with a frequency sweep between two values ("chirp") is applied. The turn-by-turn beam position data is recorded through a Base-Band-tune pickup (BBQ system) [17]. By using Fast Fourier Transform (FFT) algorithms on the turn-by-turn data over many turns, the fractional tune of the beam can be extracted. Due to limitations in the frequency chirp excitation, the beam tunes can be reconstructed no faster than 1 ms. At injection energy, this corresponds to approximately 1000 revolutions for the turn-by-turn data. The pickup is located at 3L1 and the damper at 12L1.

2.2.5 Longitudinal distribution

The energy and momentum spread of a bunched beam can be determined by reconstructing its longitudinal phase space distribution. In the PSB, this is done by measuring the longitudinal profile of the bunch over many turns. Due to the synchrotron motion, the particles inside the bunch rotate in the phase space. Thus, the different longitudinal bunch profile acquisitions correspond to different projections of the phase space at different angles. Similar to tomography, by properly combining these profiles, a first approximation of the two dimensional distribution can be obtained. The back projection of the reconstructed phase space to the bunch profile shapes and the comparison to the measured ones can be applied in an iterative process that improves the reconstruction of the phase space. This algorithm has been improved by using particle tracking to consider the non-linearities of the synchrotron motion at large amplitudes. This measurement has been automatized in the Tomoscope application [18].

2.3 Beam Optics

Particles in a periodic sequence of dipole and quadrupole magnets perform oscillations in the transverse planes known as betatron oscillations. The betatron oscillations have a modulated amplitude and phase and are usually expressed in the form:

$$u = \sqrt{2\beta_u J_u} cos\left(\int_{s_0}^{s} \frac{1}{\beta_u} + \psi_{u,0}\right), u = x \text{ or } y \tag{2.1}$$

where β_u is a function of s and J_u, $\psi_{u,0}$ are integration constants which are known as action and initial phase respectively. The β-function is a machine property and it depends on the arrangement and strength of the quadrupoles. It governs the motion in the transverse planes as it defines the variation in the local amplitude and phase of the betatron motion. It is one of the most critical parameters when designing and operating synchrotron as it encompasses most of the transverse beam properties such as the beam size and the number of betatron oscillation a particles performs during one revolution

(betatron tunes). The β-function along with the α and γ functions:

$$\alpha_u = -\frac{1}{2}\frac{d\beta_u}{ds}, \tag{2.2}$$

$$\gamma_u = \frac{1+\alpha_u^2}{\beta_u}, \tag{2.3}$$

$$u = x \text{ or } y, \tag{2.4}$$

are known as the Twiss functions or machine optics. The theory of betatron oscillations was developed and explained thoroughly by Courant and Snyder and was published in 1958 [19].

In the PSB, the transverse planes are usually between 4.0 and 4.5 in the PSB (Q4Q4 optics). The pair of horizontal and vertical betatron tunes (Q_x, Q_y) that a machine operates is known as the working point. A typical working point at injection for the LHC-type beams is $(Q_x, Q_y) = (4.40, 4.45)$ while for the fixed target beams the tunes can be lower for both planes. The extraction in the PSB is set only for the working point of $(Q_x, Q_y) = (4.17, 4.23)$. Thus, for all the different beams, the tunes are eventually dynamically ramped down throughout the cycle to this working point. Studies on different integer tunes (Q3Q5 optics for example) have been tested but not used operationally.

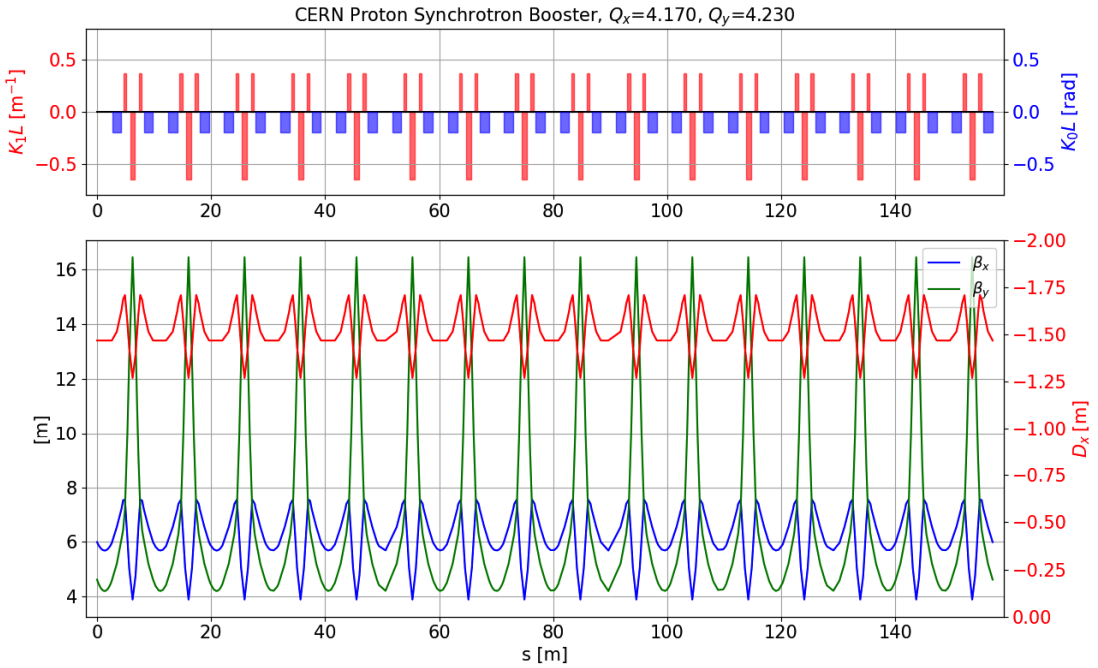

Figure 2.4: Top: integrated strength of the dipoles (blue) and quadrupoles (red) around the PSB ring. Bottom: Twiss parameters around the PSB ring for the working point of $(Q_x, Q_y) = (4.17, 4.23)$ (MAD-X). The horizontal β-function is shown in blue, the vertical β-function in green and the horizontal dispersion in red.

The PSB has a 16-fold symmetry. The model optics of the PSB are shown in Fig. 2.4 for the working point of $(Q_x, Q_y) = (4.40, 4.45)$. The horizontal and vertical β-functions are plotted in blue and green respectively. The horizontal dispersion, shown in red, is non-zero all around the ring of the PSB.

Measuring the optics of the PSB accurately is a challenging task [20]. Nevertheless, extensive studies have been performed in the past that combine different methods of determining the β-function around the ring [21]. Dispersion measurements in all rings were performed at the end of Run 2 in 2018 at the location of the pre-LIU wire scanners (2L1) and at the extraction line. In 2021 the dispersion was measured again at the positions of the LIU wire scanners (4L1 and 11L1). In both cases, the measured dispersion was very close to the model and the non-linear dispersion was small.

The chromaticity is measured in the PSB using the BBQ system. The natural chromaticity is approximately $(\xi_x, \xi_y) \approx (-0.84, -1.60)$ and is close to what is expected from the model. Generally, the PSB operates with the natural chromaticity. In case the chromaticity needs to be corrected, the PSB is equipped with dedicated sextupole correctors. However, these correctors can correct the chromaticity only at one plane at a time (horizontal or vertical).

2.4 Resonances

Magnet imperfections, such as misalignments, fringe fields and errors in the magnetic fields, can perturb the betatron motion and induce a resonant motion. Non-linear magnetic fields can also excite resonances. In the transverse planes, a resonance occurs when the betatron tunes satisfy the relation (see Appendix A.3):

$$n_x Q_x + n_y Q_y = r, \tag{2.5}$$

where n_x, n_y and r are integers. In lattice with a periodicity R, the resonance condition becomes:

$$n_x Q_x + n_y Q_y = Rr, \tag{2.6}$$

Resonances for which $n_x Q_x + n_y Q_y$ is not a multiple of the lattice periodicity are suppressed and can be excited only by random errors (random resonances). The resonances for which $n_x Q_x + n_y Q_y$ is a multiple of the lattice periodicity are called systematic. The order of the resonance is $|n_x| + |n_y|$. The resonance conditions of any order are represented with a set of lines in the tune diagram (Figure 2.5). The solid lines represent the normal resonances (even n_y) and the dashed lines skew resonances (odd n_y). The motion near a resonance can become chaotic and particles can diffuse to large amplitudes and eventually be lost in the machine aperture.

Resonance studies have been an important part of the PSB operation. In 2021, resonances up to fourth order are observed [22], both normal and skew. Figure 2.6 shows a typical loss map measurement of all the PSB rings. The measurement is performed by dynamically changing the tunes and recording the beam loss rate at each working point. Differences are observed between the different rings. However, the vertical half-integer resonance at $Q_y = 4.5$ is present in all rings (omitted from Figure 2.6).

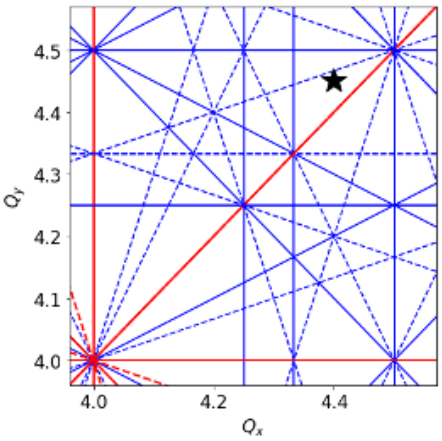

Figure 2.5: Tune diagram for the PSB. Up to fourth order normal (solid lines) and skew (dashed lines) resonances are plotted. The systematic resonances are plotted with red. The star shows a typical working point at injection.

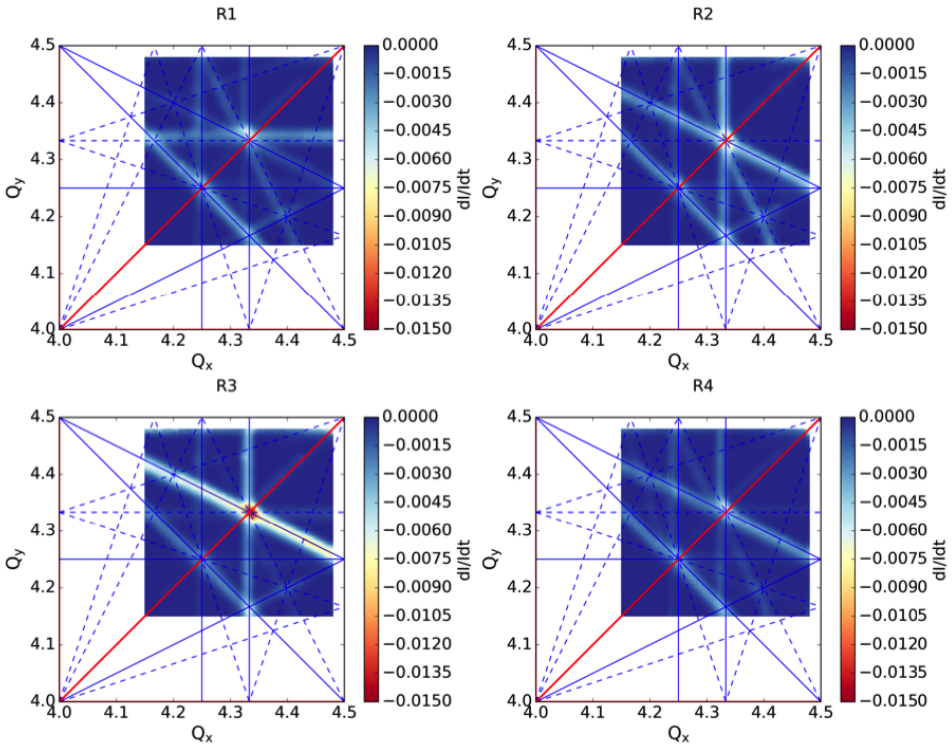

Figure 2.6: Measured loss map for the PSB ring 1 (top-left), ring 2 (top-right), ring 3 (bottom-left) and ring 4 (bottom-right) [22]. The colors correspond to the beam loss rate variation during the dynamic tune scans. Resonance lines up to 4th order are plotted.

Quadrupole, sextupole and octupole correctors are used throughout the cycle of the PSB in order to develop compensation schemes for the measured resonances. For example, the naturally excited half-integer resonance at $Q_y = 4.5$, is compensated experimentally by two orthogonal families of quadrupole correctors. The quadrupoles of each family have opposite polarity and so the overall tune shift that they induce is zero.

2.5 Space Charge and Brightness

The direct space charge refers to the electro-magnetic self-interaction between the charged particles of a beam. The self-fields that move with the beam induce a continuous defocusing force to the beam particles. This defocusing induces a negative tune shift. The defocusing is non-linear and therefore particles will have different tune shifts depending on their betatron amplitude (tune spread). Particles in the beam core will receive a larger tune shift than the ones of the beam tails. It can be shown [23] that for a bi-Gaussian distribution, the maximum tune shift is given by:

$$\delta Q_{x,y}^{SC} = -\frac{r_0 \lambda}{2\pi e \beta_r^2 \gamma_r^3} \oint \frac{\beta_{x,y}}{\sigma_{x,y}(s)\left[\sigma_x(s) + \sigma_y(s)\right]}, \tag{2.7}$$

where r_0 is the classical proton radius, λ the longitudinal charge density, e the elementary charge, β_r and γ_r the relativistic parameters, $\beta_{x,y}$ the Twiss functions and $\sigma_{x,y}$ the beam sizes in the horizontal and vertical planes. It can be seen that the detuning decreases with energy like $\beta_r^2\gamma_r^3$. For high-energy machine, the space charge effects are negligible. But, for low energy machines, like the PSB, the maximum space charge tune spread can reach values even up to -0.5 at injection energies, as it is shown in the tune diagram of Figure 2.7. In this case the bare tune is set at the black square point. Due to space charge, the tunes of the individual particles can reach values even beyond the first order resonances at the integer tunes of $Q_{x,y} = 4.0$ (green lines). The second order vertical half-integer resonance at $Q_y = 4.45$ is highlighted with the red line.

The space charge detuning depends on the longitudinal line density λ. For an unbunched (coasting) beam, λ is constant while for a bunched beam λ is a function of z. In the latter case, the space charge force, and therefore the tune spread, will be stronger for particles in the bunch center rather than in the bunch head or tail. Particles in a bunch perform energy-phase oscillations known as synchrotron oscillations. The frequency of the synchrotron oscillations is known as synchrotron tune and is usually much smaller than the betatron tunes. Due to the synchrotron motion, the longitudinal position z of a particle, and therefore its local line density, changes. This translates in a modulation of the space charge tune spread with a frequency that is twice the synchrotron frequency.

Space charge, through the tune spread, can drive particles into resonances and can result to beam degradation such as beam losses and emittance growth. The underlying mechanisms have been described in terms of periodic resonance crossing due to the modulation of the space charge detuning of bunched beams [24, 25, 26]. Particles that periodically cross the resonance will diffuse to larger transverse amplitudes. The macroscopic behavior of the beam with space charge near a resonance depends on the

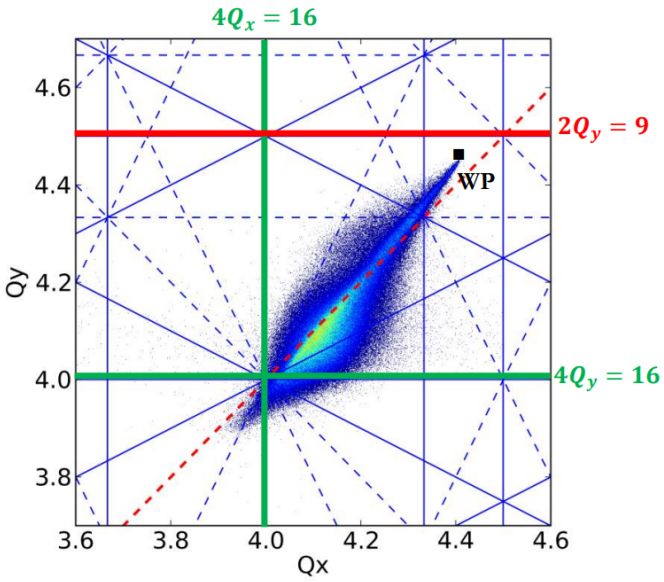

Figure 2.7: Simulation example of the space charge induced tune spread at injection of the PSB.

tune spread and the distance between the working point and the resonance line. This is illustrated in Figure 2.8. In the left graph, the bare tune is set on the resonance. In the absence of space charge, setting the bare tune on a resonance would make the particle motion unstable. But here, the space charge depresses the particle tunes and so, almost no particle is fulfilling the resonance condition. Macroscopically, no emittance increase or losses would be observed. If the bare tune is moved slightly higher, like the second graph of Figure 2.8, the particles in the beam tails would satisfy the resonance condition. The periodic resonance crossing, would force these particles to drift towards larger amplitudes, and eventually get lost. With fewer beam particles, the space charge would become weaker and the tune spread would shrink. This process would be repeated until the a large fraction of the beam is lost. By moving the bare tune higher, like in the third graph of Figure 2.8, particles from the beam core would now periodically cross the resonance. The diffusion of these particles to higher amplitudes would induce emittance growth and some losses. The increase of the emittance (beam size), would also reduce the space charge tune spread until the resonance does not affect the beam any longer. Finally, for even higher bare tunes, only some residual emittance growth would appear.

Space charge in combination with resonances can limit the brightness performance of an accelerator. The beam brightness is defined as the ratio between the beam intensity and the transverse emittances:

$$B = \frac{N_b}{0.5(\epsilon_x + \epsilon_y)}. \tag{2.8}$$

If the space charge tune spread is large enough, particles from the beam core can reach the integer resonances, as shown in Figure 2.7. This would lead to an emittance growth

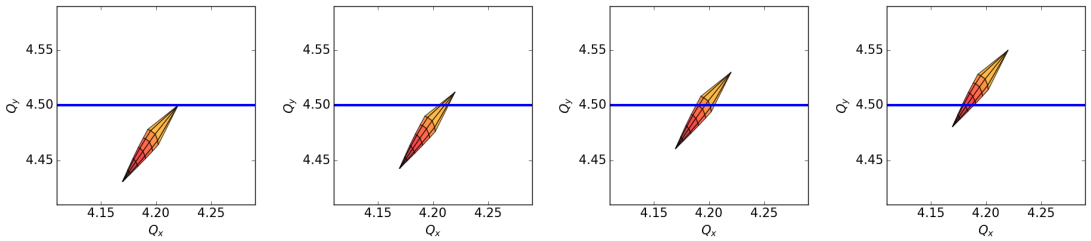

Figure 2.8: Illustration of different scenarios on the relative positioning between the space charge tune spread (orange) and a resonance line (blue). Due to the periodic resonance crossing, beam losses dominate in the first and second case while emittance growth dominates in the third and fourth case.

and reduce the beam brightness. With an increased beam intensity, the space charge becomes stronger, and so does the emittance growth. This results to the overall brightness remaining almost constant. Space charge in combination with resonances constitutes the main limit of the PSB brightness reach.

2.6 LIU Upgrades

As described in Chapter 1.2, the LHC injectors recently underwent major upgrades as part of the LIU project, with the aim of achieving the high-intensity and high-brightness beams required by the HL-LHC. Regarding the PSB, the upgrades can be summarized into two main parts:

- upgrade of the injection transfer line and the injection sector for the connection of Linac4,
- upgrade of the rings and the extraction transfer line.

Both of these upgrades aim at addressing the space charge effects. In particular, the injection upgrade mitigates space charge at PSB injection, while the upgrades in the ring mitigate space charge effects in the PS.

2.6.1 Injection upgrade

An increase of the PSB injection energy reduces the tune spread induced by space charge, which is inversely proportional to $\beta_r^2\gamma_r^3$ (see eq. 2.7). To this end, Linac2 delivering protons at a kinetic energy of 50 MeV was replaced by Linac4 that delivers H^- ions at an increased kinetic energy of 160 MeV. This energy increase results in a factor of two reduction of the space charge forces. This in turn allows doubling the beam intensity while having similar space charge detuning for the same transverse emittances.

To convert the H^- ions to protons, the multi-turn stacking injection system was replaced by a new charge exchange injection [27]. This consists of a horizontal chicane

and a thin carbon stripping foil. A set of four pulsed dipole chicane magnets (BSWs) have been installed in the 2.6 m long 1L1 straight section, for each of the four PSB rings (16 independently powered magnets in total). These chicane magnets create a maximum horizontal bump of 46 mm (injection bump). In addition, the beam orbit is deformed by a bump created outside of the injection period by another set of four kicker magnets (KSW). The KSW magnets are located in 1L4, 2L1, 16L1 and 16L4 and produce a closed orbit bump of 35 mm at the injection point.

The charge-exchange injection process is illustrated in Figure 2.9. The incoming H^- beam (shown in red) is deflected by the BSW2. When the beam passes through the stripper foil, the electrons are removed. The remaining protons are deflected by BSW3 and BSW4 and continue their path around the ring. The partially stripped hydrogen atoms H^0 or H^- end up in a beam dump. The process is repeated over many turns (multi-turn injection) until the desired beam intensity is reached. After the injection process the bump decays to zero. Note that BSW1 has a reduced width compared to the rest of the bumpers in order not to interact with the incoming H^- beam.

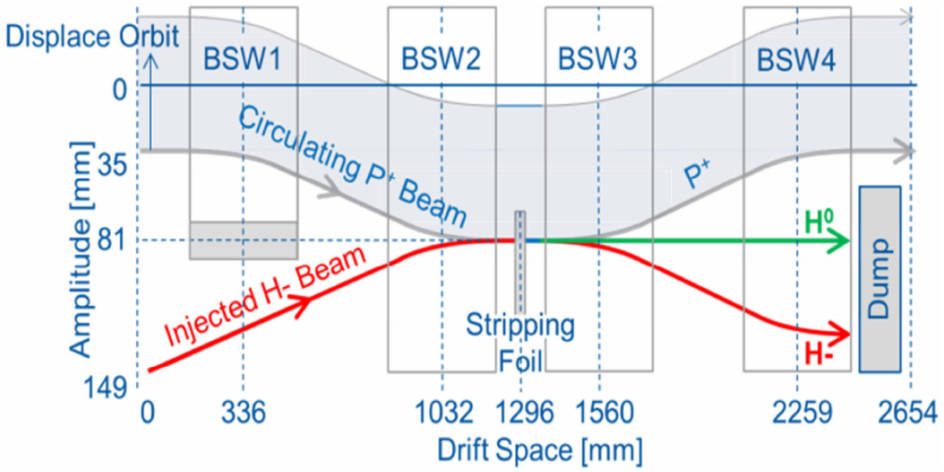

Figure 2.9: Schematic layout charge-exchange injection region. The red line represents the H^- beam that comes from the Linac4.

A significant benefit of the new injection scheme is the injection efficiency. While with the old injection scheme approximately 50 % of the beam would be lost at injection, now the injection is almost loss-free, with the stripping efficiency being more than 99 %. Furthermore, the new injection scheme allows transverse painting to fill the phase space area more uniformly and further decrease space charge. This can be done by adjusting the KSW bump (painting bump) according to the requirements of the different users. Longitudinal painting to equally fill the RF bucket is also possible by modulating the energy spread of the incoming L4 beam.

2.6.2 Rings upgrades

The PS also suffers from strong space charge effects at injection. Similarly to the PSB, the injection energy of the PS was increased from 1.4 GeV to 2 GeV. Thus, considerable upgrades were applied in the PSB rings and their extraction systems in order to permit the acceleration and extraction of 2 GeV beams.

Since the existing power converters could not satisfy the voltage and power increase foreseen for the PSB magnets with the LIU extraction energy, a new main power supply was built. The new power supply consists of a number of nested circuits that go through the dipoles and quadrupoles of the machine. In this new configuration, there is one common circuit going through the dipoles of the external rings of the PSB (ring 1 and 4), the MPS14, and one common circuit that powers the dipoles of the internal rings (ring 2 and 3), the MPS23. The MPS14 is also shared with the 128 focusing quadrupoles and the MPS23 with the 64 defocusing quadrupoles of all rings. In addition, there are trim power supplies for the focusing and the defocusing quadrupoles, namely QFO and QDE circuits respectively, that are used for the base tune control. Separate q-strip circuits for each ring are also available for the focusing quadrupoles (QCF circuits) and the defocusing quadrupoles (QCD circuits). These can be used for ring-to-ring tune adjustments. The total current for the PSB focusing (QF) and defocusing (QD) quadrupoles can be summarized using the relations:

$$I_{\mathrm{QF}}^{\mathrm{total}} = I_{\mathrm{MPS14}} + I_{\mathrm{QFO}} + 0.5 \cdot I_{\mathrm{QCF}} \tag{2.9}$$

$$I_{\mathrm{QD}}^{\mathrm{total}} = I_{\mathrm{MPS23}} + I_{\mathrm{QDE}} + 0.5 \cdot I_{\mathrm{QCD}} \tag{2.10}$$

The factor 0.5 for the currents of the QCF/QCD circuits is due to the fact that the main coils of the quadrupoles have twice the number of turns compared to the trim coils of the q-strips.

The RF systems also underwent major renovations. The low-level RF (LLRF) system was upgraded to a fully digital system and the C02 and C04 RF systems were replaced by new wideband cavities.

Other upgrades within LIU included the improved instrumentation for assessing the beam characteristics (e.g. LIU-WS), modifications in the electrical and vacuum systems and refined control and interlock systems.

2.7 Modelling of the PSB

All the CERN accelerators are modelled in MAD-X [28]. The different machines are available for the different beams (optics scenarios) and for different instances during the accelerating cycle (injection, flat bottom, flat top, etc.). The MAD-X sequence of all the different elements in the PSB (magnets, instruments, collimators and RF cavities), along with their corresponding apertures, will be referred throughout the thesis as the PSB model (MAD-X) lattice. The PSB model lattice can be matched to a wide range of working points and can include magnetic field errors, magnet misalignments, edge focusing and higher order multipoles for studying the optics stability.

The PSB particle tracking simulations have been performed using PTC-PyORBIT [29]. The Polymorphic Tracking Code (PTC) [30] is a set of FORTRAN90 libraries for integrating equations of motion for particles in modern accelerators and storage rings (tracking). Each accelerator element of the PSB was divided into 5 equal slices and for each step an integration is performed using the "Matrix-Kick-Matrix" model and the exact Hamiltonian. PyORBIT is a Python wrapper for the Objective Ring Beam Injection and Tracking (ORBIT) [31] code, which provides the framework for modelling processes like the beam injection. PyORBIT included MPI, to exploit the parallel computing capabilities of the CERN computer clusters and boost the speed of the calculation, and Patricle-In-Cell (PIC) routines for detailed space charge calculations.

Chapter 3

Injection Chicane Beta-Beating

3.1 Perturbations from the Injection Magnets

The upgrade of the PSB injection system brought along many benefits but also some new challenges. One of these challenges is the magnetic field perturbations induced by the injection chicane magnets. More specifically, the four BSW magnets, that are relatively short and rectangular in shape, induce strong fringe fields in the space around their edges. In a linear approximation, the fringe fields of a horizontal dipole have the effect of a quadrupolar-like field perturbation in the vertical plane, known as edge focusing. Furthermore, during the ramp-down of the injection chicane, eddy currents are generated in the metallic vacuum chamber that create additional magnetic fields inside the BSWs. The eddy currents induce a sextupolar field, proportional to the ramp rate of the BSWs [32, 33]. Because the polarity of the outer BSWs (BSW1 and BSW4) is opposite to the polarity of the inner ones (BSW2 and BSW3), the sextupolar components cancel each other and third order resonances are not excited by them. But, since the beam enters the BSWs with an offset with respect to their magnetic center, the sextupolar component leads to feed-down effects. The feed-down effects refer to the lower field components that are produced from magnet misalignments. In this case, due to the offset between the BSWs and the beam orbit, the sextupolar component causes quadrupolar field perturbations also in the vertical plane. The effects of the fringe field and the eddy currents are of comparable size and cause distortions in the vertical optics around the machine.

The KSW magnets that produce the painting bump, also induce edge focusing. However, their deflection angles are much weaker than the ones of the injection chicane. This is why the KSW induced quadrupolar field perturbations are insignificant compared to the ones of the BSW and are neglected for the rest of the study.

The edge effects and the sextupolar components that are expected from the BSW magnets have been estimated using measurements and magnetic simulations [32]. Figure 3.1 shows the expected dipolar and sextupolar component at one of the BSW magnets as a function of time. The chicane fully collapses 5 ms after the injection, which itself happens 275 ms after the start of the PSB magnetic cycle. The field components are

similar for the other BSW magnets and have been modelled in MAD-X in order to be applied in the PSB lattice.

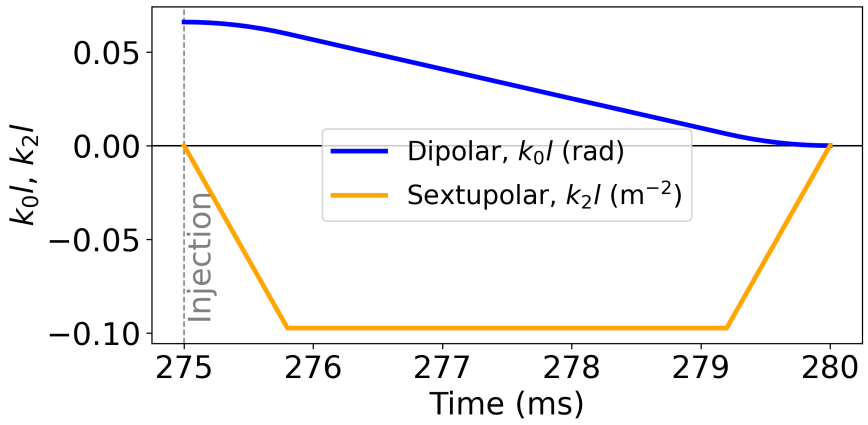

Figure 3.1: Modelled dipolar (blue) and sextupolar (orange) components of the BSWs as a function of time.

The injection chicane field perturbations are expected to have a strong impact on the beam performance, especially close to the vertical half-integer resonance $2Q_y = 9$. In the PSB at injection energies, the incoherent space charge tune spread can reach values up to $\Delta Q = -0.5$ [34]. The systematic resonances at the integer tunes $4Q_{x,y} = 16$ are strongly excited by the space charge potential due the lattice periodicity of 16, in combination with all other random field errors. To avoid beam degradation due to the integer resonances, the machine is operated very close to the vertical half-integer resonance. Operation with working points close to the half-integer resonance strongly enhances the optics distortions induced by the injection chicane perturbations, which can eventually lead to beam losses and reduce the deliverable beam brightness.

3.2 Simulations of the Injection Chicane Perturbations

3.2.1 Tune distortions and beta-beating

As discussed in Section 2.3, the β-function is one of the most important property of an accelerator for controlling the motion and quality of the particle beams. Perturbations in the magnetic field of quadrupoles introduce a variation in the β-function. This results to a change both in the amplitude and the phase of the betatron oscillations. These effects are known as β-beating and tune shift, respectively. To first order in the perturbation strength k_1 (linear approximation), the tune shift is calculated to be (see Appendix A.1):

$$\delta Q = -\frac{1}{4\pi} \oint \beta_x(s) k_1(s) ds, \tag{3.1}$$

and the β-beating:

$$\frac{\delta\beta(s)}{\beta(s)} = \frac{1}{2\sin(2\pi Q_0)} \oint \beta(s_1)k_1(s_1)\cos\left[2(\psi(s)-\psi(s_1))+2\pi Q_0\right] ds_1, \tag{3.2}$$

where ψ is the betatron phase advance, and Q_0 is the bare (unperturbed) betatron tune. The distortion in the β-function is referred as 'beating' because its amplitude modulates with twice the betatron frequency. The tune shift and the β-beating are proportional to the perturbation strength and the β-function at its location. Furthermore, when the fractional part of the bare tune approaches an integer or a half-integer (i.e. 0.5) value, the β-beating grows to infinity. The perturbation has the biggest impact to the β-function when the tune approaches these values, like in the case of the PSB at which the working points can be close to 4.5. When the β-beating is strong, the betatron oscillations can be large enough so that particles hit the machine aperture and are eventually lost.

The edge focusing and the feed-down effects of the BSW magnets induce quadrupolar field perturbations in the vertical plane, which lead to a tune shift and β-beating. The quadrupolar perturbations dynamically change during the collapse of the injection chicane (Figure 3.1) and so are the distortions in the tune and optics of the machine.

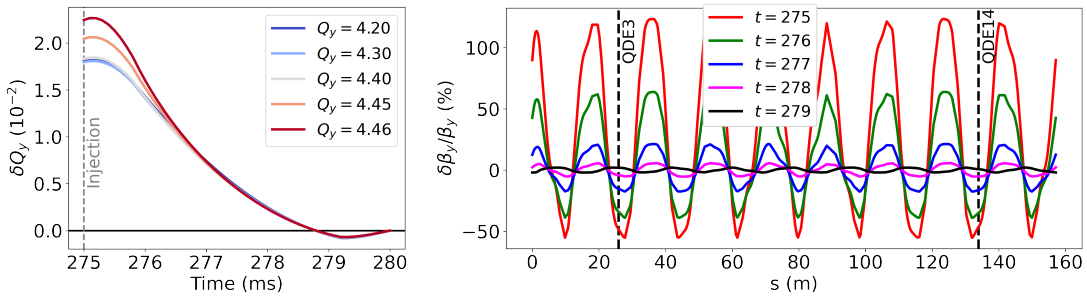

Figure 3.2: Left: tune perturbation as a function of time for different vertical tunes. The horizontal tune is kept constant at $Q_x = 4.40$. Right: β-beating around the machine for different times during the collapse of the injection chicane for the working point of $(Q_x, Q_y) = (4.40, 4.44)$.

Fig. 3.2 shows a simulation of the expected tune shift and the β-beating, during the first 5 ms after injection. The plot on the left hand side shows the vertical tune shift as a function of time, for different vertical tunes. The quadrupolar perturbations are stronger at injection, which lead to a tune shift of approximately 0.02. On the right hand side, the vertical β-beating is plotted around the ring:

$$\frac{\delta\beta_y}{\beta_y} = \frac{\beta_y - \beta_{y,0}}{\beta_{y,0}}, \tag{3.3}$$

where $\beta_{y,0}$ is the nominal β-function, for the working point of $(Q_x, Q_y) = (4.40, 4.44)$. The different colors correspond to different times after injection. The β-beating dynamically changes during the decay of the chicane. At the injection time ($t = 275$ ms), the

chicane is at its maximum amplitude and the perturbation is the strongest with the expected maximum β-beating reaching 100%.

For tunes even closer to the half-integer resonance, the β-beating grows rapidly. As shown in Figure 3.3, for a given focusing perturbation (in this case the one at $t = 275$ ms), the maximum β-beating can exceed 200%. Here, the β-beating is plotted as a function of the set vertical tune. Due to the induced tune shift, the beam will be closer to the half-integer resonance.

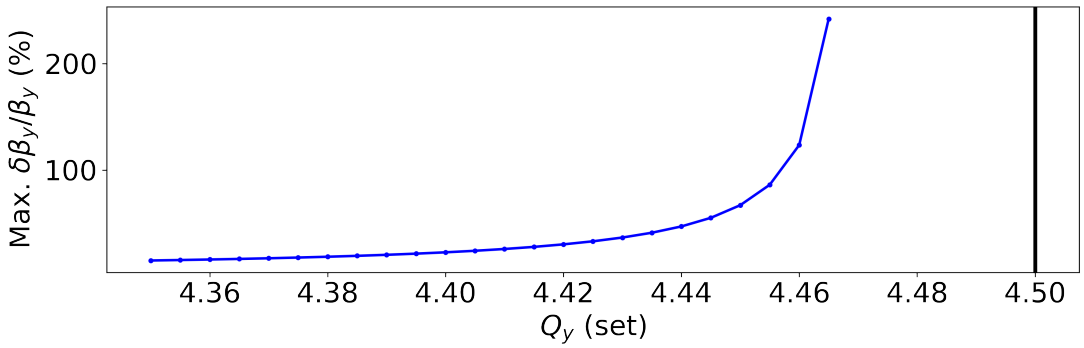

Figure 3.3: Maximum β-beating as a function of the set vertical tune near the half-integer resonance $2Q_y = 9$ (black line).

The control of the optics plays a fundamental role in the performance and operation of strong focusing synchrotrons. The β-function dictates the motion of the particles in the transverse planes, the betatron tune and the beam size and consequently the beam losses, beam emittance, brightness and the luminosity in particle colliders. For example, the reduction of the β-beating to below 1 % in the LHC provided equal luminosity to ATLAS and CMS [35]. But, the optics control is a very difficult task to do. This is particularly true for the PSB since the strong time-varying perturbations require fast and dynamic correction of the optics already at injection. If not corrected, the beam cannot be injected for a large set of tunes around the half-integer resonance and the brightness performance of the PSB can be limited. The dynamic optics correction not only requires to overcome technical challenges, but also provides unique physical aspects in the dynamics of the beams, as it is discussed in the next sections.

3.2.2 Method of measurement and correction

As shown in section 2.6.2, all the quadrupoles in the PSB are powered in series and so, before the LIU upgrades, individual control of quadrupoles was not possible. For this reason, in order to compensate the injection chicane induced perturbations, two of the main defocusing quadrupoles of the machine received additional, individually controlled, fast power supplies [36]. The preferred quadrupoles to receive the separate power supplies were the defocusing quadrupoles of periods 3 and 14, QDE3 and QDE14 respectively. The QDE3 and QDE14 are equidistant and relatively close to the localized

perturbations at the injection region. Following the same notation as of eq. 2.9, the total current of these two special quadrupoles can be expressed as:

$$I_{\mathrm{QD3}}^{\mathrm{total}} = I_{\mathrm{MPS23}} + I_{\mathrm{QDE}} + 0.5 \cdot I_{\mathrm{QCD}} + 0.5 \cdot I_{\mathrm{QCD3}} \tag{3.4}$$

$$I_{\mathrm{QD14}}^{\mathrm{total}} = I_{\mathrm{MPS23}} + I_{\mathrm{QDE}} + 0.5 \cdot I_{\mathrm{QCD}} + 0.5 \cdot I_{\mathrm{QCD14}} \tag{3.5}$$

The aim is to apply additional current only to QDE3 and QDE14, through the new knobs I_{QCD3} and I_{QCD14}, in order to compensate the β-beating induced by the injection chicane.

Since the quadrupolar perturbations dynamically change, time dependent compensation strengths need to be applied in QDE3 and QDE14 during these 5 ms. The left plot of Fig. 3.4 shows a simulation of the expected distortion in the spatial average (average along the quadrupole magnet) $\bar{\beta}_y = \int \beta_y(s)\, ds$ at the location of QDE3 as a function of time, for the working point of $(Q_x, Q_y) = (4.40, 4.44)$. The unperturbed $\bar{\beta}_y$ (blue line) is constant at 16.26 m. Due to the injection chicane perturbations, the β-function is deformed (orange line). The right plot of Fig. 3.4 shows the local β-beating at the location of QDE3 as a function of time for different vertical tunes. While the bare tune approaches the half-integer resonance, the local β-beating grows significantly. The local β-beating is similar at the position of the QDE14 magnet.

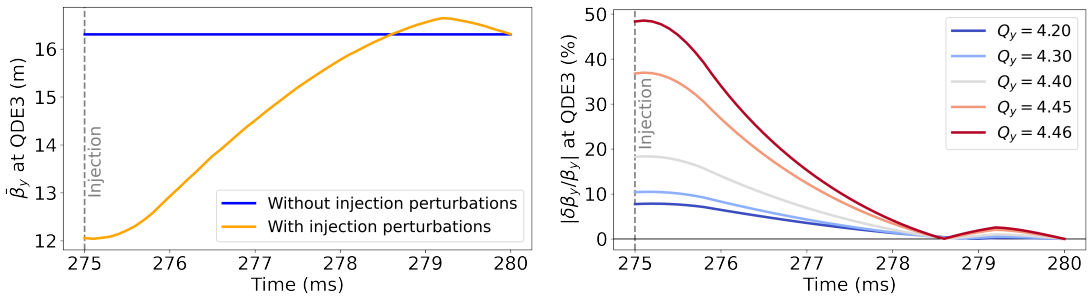

Figure 3.4: Left: distortion in the $\bar{\beta}_y$ at the position of QDE3 as a function of time for the working point of $(Q_x, Q_y) = (4.40, 4.44)$. Right: local beta-beating at the position of QDE3 for different vertical tunes (right). The horizontal tune is kept constant at $Q_x = 4.40$.

Within this context, the need for a method to identify and correct the optics distortions induced by the injection chicane was created[37]. There were three important requirements that this method had to satisfy. The first one is that it had to be able to measure the real optics distortions in the machine, that might come from field perturbations that deviate from the expected ones of Figure 3.1. The second condition was that it had to predict optics correction values over time for the special quadrupoles QDE3 and QDE14 that are based on the measured distortions. Finally, the method had to take into account all the machine conditions and restrictions so that it can be operationally implementable.

In the beginning of 2020, a series of simulations were performed in MAD-X in order to develop such a method as part of this thesis. These simulations will be described in detail in the following sections. By the end of 2020, the method was implemented in an operational application. During the beam commissioning of 2021 and the restart of the machines in 2022, it was used for correcting the injection chicane induced optics distortions and is now part of the PSB commissioning procedures.

K-modulation

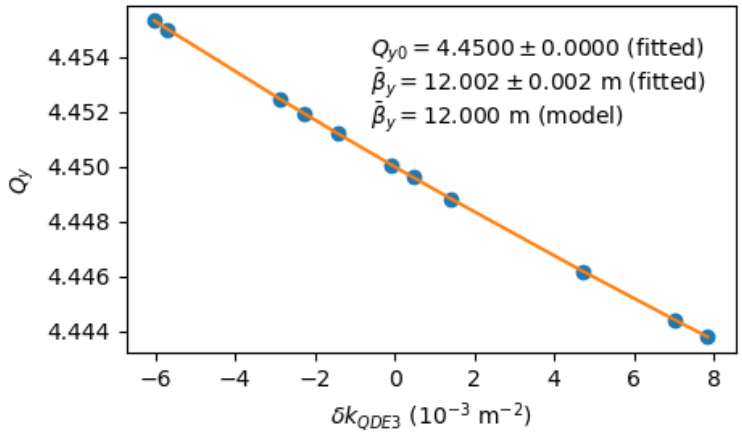

Figure 3.5: MAD-X simulation of the k-modulation measurement at QDE3. The blue points are fitted with equation 3.7 (orange line). The reconstructed from the fit $\bar{\beta}_y = 12.002 \pm 0.002$ m is identical with the expected from the model.

The injection chicane β-beating is compensated by measuring and correcting the local β function distortions at the positions of QDE3 and QDE14. The aim is to find a configuration for the powering of the two quadrupoles such that their induced β-wave cancels the β-wave of the injection chicane perturbations. The injection chicane induced distortion at the positions of QDE3 and QDE14 (local β-beating) is measured with k-modulation [38]. The k-modulation is a method to accurately measure the β-function at the location of a quadrupole. The method consists of applying a small quadrupolar kick (δk) to the beam and measuring the induced tune shift (δQ). The tune shift depends on the β-function at the location of the quadrupole. When the kick is small, the induced tune shift is approximately linear with the β-function:

$$\delta Q \approx \frac{\delta k \beta_0 L}{4\pi} \tag{3.6}$$

Although this approximation is valid for most cases, for the PSB near the half-integer resonance the non-linear expression is needed:

$$\delta Q = \frac{1}{2\pi} \cos^{-1}\left(\cos(2\pi Q_0) + \frac{\bar{\beta}\delta k L}{2}\sin(2\pi Q_0)\right) - Q_0, \tag{3.7}$$

where Q_0 is the nominal betatron tune, L is the quadrupole magnetic length and $\bar{\beta}$ is the spatial average β-function along the quadrupole. This is still a first order approximation in δk. A derivation of this expression is presented in the Appendix A.2.

Figure 3.5 shows a simulation of the β-function measurement at the QDE3 using MAD-X. The blue points represent the tune for the different kicks in QDE3 and the orange line the fitting of eq. 3.7. It can be seen that even near the half-integer resonance ($Q_y = 4.45$) the β-function can be reconstructed from the fit very accurately with only a handful of points.

Error response matrix

Having measured the local β-beating at QDE3 and QDE14, one needs to compute a dynamic β-beating correction specific for the measured distortions. This is done by interpolating the measured distortions to a pre-defined response matrix. The use of a response matrix is possible due to the fact that the source of the focusing errors is localized (all BSW magnets are located in the straight section of the first period of the PSB). The injection chicane perturbations can be very well approximated as a focusing error installed at the injection point.

The response matrix is generated using MAD-X the in following way. In the injection region of the PSB MAD-X lattice, a focusing error is installed that mimics the β-beating induced by the injection chicane. The β-beating is then corrected by matching the optics back to the unperturbed values using as knobs the focusing strengths of QDE3 and QDE14. These knobs represent the separate power supplies that the two quadrupoles have received. This procedure is repeated for a large range of working points and for different strengths of the focusing error at the injection region. In this way, a mapping is created between the induced β-distortions at the location of QDE3 and QDE14 and the focusing strengths that, when applied in QDE3 and QDE14, will compensate these distortions.

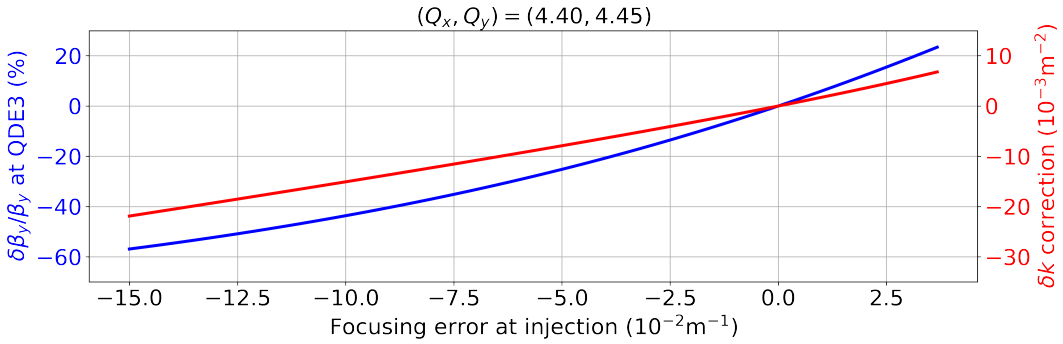

Figure 3.6: Simulated response of the $\bar{\beta}_y$ (blue) and the QDE3/QDE14 compensation strengths (red) for different strengths of focusing errors at injection. The working point is fixed at $(Q_x, Q_y) = (4.40, 4.45)$.

In Figure 3.6, a small part of this response matrix is plotted. On the horizontal axis is the strength of the focusing error at the injection region, that represents the injection chicane perturbations. On the left vertical axis is the induced β-distortion at the location of QDE3 and on the right vertical axis is the focusing strength of QDE3 and QDE14 that compensates the corresponding β-distortion. These values have been calculated for the working point of $(Q_x, Q_y) = (4.40, 4.45)$. For different horizontal and/or vertical tunes, these values can change considerably.

The β-functions that are measured with k-modulation are interpolated to this response matrix in order to find the optimal configuration for the strengths of QDE3 and QDE14 to minimize the local β-beating. Figure 3.7 shows an example of the optimal dynamic correction functions over time retrieved from such an interpolation.

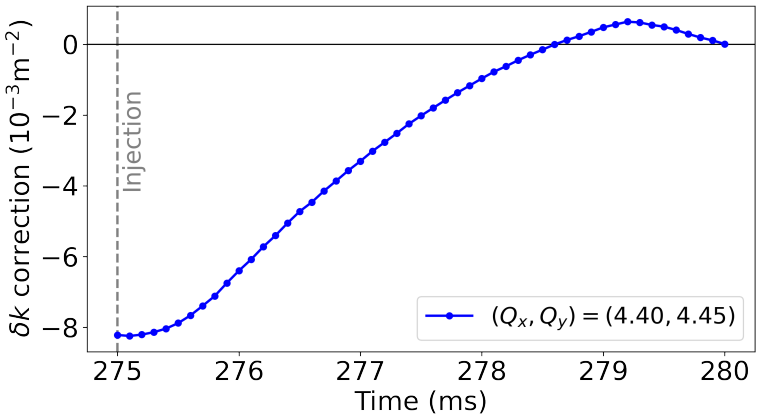

Figure 3.7: Optimal dynamic β-beating correction functions for QDE3 and QDE14 from simulations.

The tune distortions induced by the injection chicane need to be dynamically corrected along with the β-beating. The dynamic correction of the tune is extracted also by interpolating to a response matrix. The only difference to before is that not only QDE3 and QDE14 are used as knobs for the correction but all the focusing and defocusing quadrupoles of the PSB (QCF/QCD circuits). It is important to mention that the β-beating correction can slightly distort the tune and the tune correction can slightly degrade the β-beating correction. For example, a dynamic correction like the one of Figure 3.7 affects the vertical tune. This is taken into account and corrected accordingly. A compromise between low β-beating and flat (corrected) tune must be made.

Simulation of the β-beating correction

The k-modulation measurement and the β-beating correction from the response matrix was entirely simulated in MAD-X. The PSB model lattice was perturbed using the field components of Figure 3.1 and then the local β-beating measurement with k-modulation, at the positions of QDE3 and QDE14, was simulated for the full decay of the injection

chicane. The local β-beating values were interpolated to the response matrix and the dynamic correction functions were extracted and applied in QDE3 and QDE14.

A simulation example of the β-beating correction is shown in Figure 3.8. The red dashed line shows the β-function of the PSB ring 3, at $t = 275$ ms (time of the injection) for the working point of $(Q_x, Q_y) = (4.39, 4.44)$. At this time, the injection chicane perturbations are the strongest and cause an RMS β-beating of the order of more than 30%, for this working point. The blue line shows the β-function after the correction has been applied. The β-beating is nearly perfectly compensated with only some residual β-beating around the injection region, which is expected due to the design of the compensation scheme. It is nevertheless small. The dynamic tune correction, that was also included in the simulations, only slightly degraded the β-beating correction (within 1%).

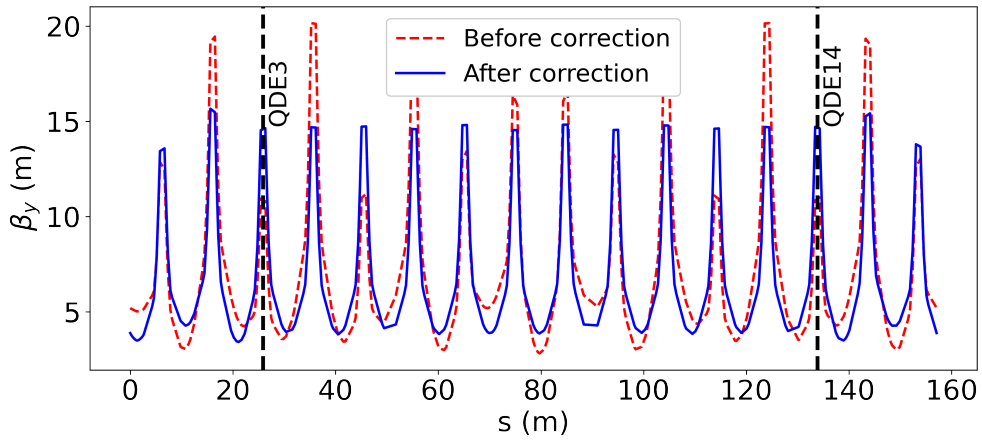

Figure 3.8: Simulated β-function before (red) and after (blue) applying the correction at $t = 275$ ms for the working point of $(Q_x, Q_y) = (4.39, 4.44)$. The black dashed lines represent the positions of QDE3 and QDE14.

The simulation was repeated for all the times during the decay of the injection chicane and also for a wide range of horizontal and vertical tunes. In all cases the correction was nearly perfect, which demonstrated a proof of principle of the method for the PSB.

3.2.3 Sensitivity studies

Although the k-modulation-based correction method works very well in principle, there are uncertainties in the real machine that need to be taken into account. For example, the k-modulation relies on an accurate tune measurement for relatively small quadrupolar kicks δk. However, the accurate experimental determination of the tune is not trivial. Moreover, not only the injection chicane perturbations might be present in the real machine. Sources of random focusing errors, that excite the half-integer resonance and cause additional β-beating, were observed in the previous years in the PSB. These errors can reduce the effectiveness of the method as they are not modelled by the response matrix.

The space charge effects and the ways they can affect the β-beating correction also need to be taken into account. The robustness of the β-beating correction method, when considering all of these factors, was tested extensively before the 2021 beam commissioning, using simulations and data from previous runs of the PSB.

Uncertainty in the tune measurement

The transverse tunes in the PSB are measured by exciting betatron oscillations of the beam and applying Fourier analysis to turn-by-turn beam position data. Depending on the exact beam parameters, the quality of the excitation, the beam position data and the number of turns analyzed, the reconstructed tune will have an uncertainty with respect to the (unknown) true value.

The uncertainty in the tune has been included in the simulated k-modulation measurement of MAD-X. For each quadrupolar kick δk, the tune shift δQ has been randomized using samples from a normal distribution:

$$\delta Q \rightarrow \delta Q + \delta\epsilon_{\text{random}} \tag{3.8}$$

where $\delta\epsilon_{\text{random}}$ is drawn from a normal distribution centered at zero and with a standard deviation σ_Q. The value of σ_Q will be referred to as the level of uncertainty in the tune measurement.

During the time of this study, all the CERN accelerators were shut-down, so the actual uncertainty σ_Q was unknown. Therefore, in order to get a reasonable value for σ_Q, turn-by-turn data from studies of the past years were analyzed. The tune uncertainty from an impedance study carried out in the PSB in 2014 at 160 MeV was approximately $0.5 \cdot 10^{-3}$ [39]. A similar uncertainty was estimated from a study in 2018 regarding the q-strips [40]. The 2018 reference tune measurements showed a slightly higher uncertainty of approximately $\sigma_Q \approx 1.0 \cdot 10^{-3}$ [41].

The simulation of the k-modulation measurement was repeated in MAD-X, but now including the uncertainty in the tune measurement. Figure 3.9 shows a simulation of the β-function measurement at the QDE3 using MAD-X, similarly to Figure 3.5, but with $\sigma_Q = 1.2 \cdot 10^{-3}$. The reconstruction from the fit of the β-function at QDE3 is now much less accurate (model value is 12 m) and precise (uncertainty is ± 0.715 m). This can degrade the β-beating correction.

By increasing the number of points in the k-modulation measurement, the uncertainty (error) of the reconstructed β-function from the fit will decrease. For this reason, one can impose in the simulation a tolerance in the error of the fitted β-function. This tolerance can be reached by repeating the (simulated) tune measurement for random values of the δk shift. For example, given an uncertainty in the tune measurement of $\sigma_Q = 0.6 \cdot 10^{-3}$, to reach an error tolerance in the fitted β-function of 0.1 m, approximately 300 $\delta k - Q_y$ points are needed.

The fitted β-function error tolerance was used as an input parameter in the simulation in order to statistically test the performance of the β-beating measurement and correction method. Figure 3.10 shows the residual β-beating after the correction method

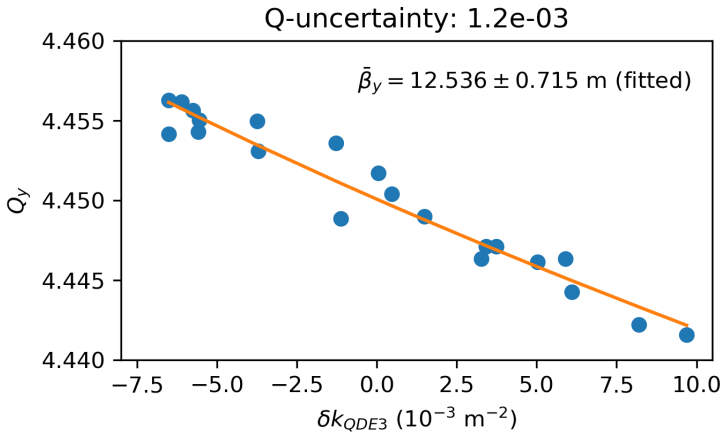

Figure 3.9: MAD-X simulation of the k-modulation measurement at QDE3 when including a fluctuation in the tune measurement (blue points). In this case, the reconstructed from the fit (orange line) $\bar{\beta}_y$ has an uncertainty of 6 %.

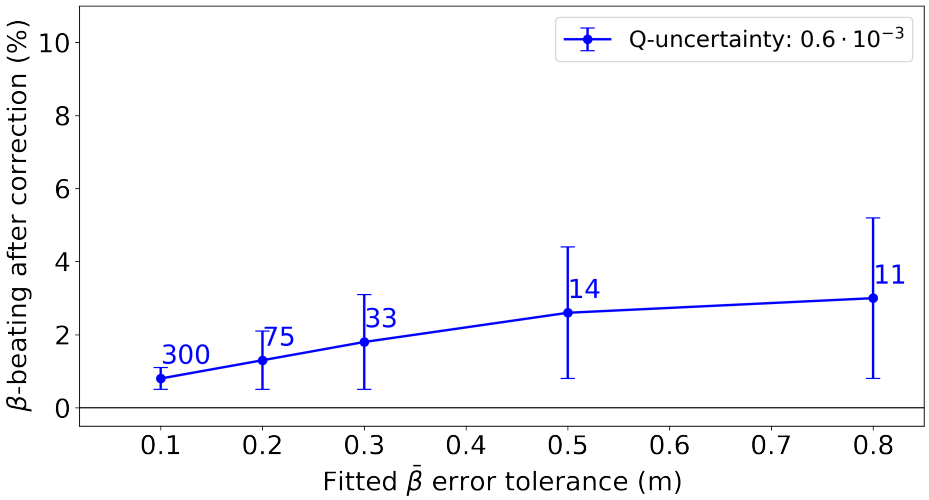

Figure 3.10: Residual β-beating after the correction as a function of the error in the fitted β-function when assuming $\sigma_Q = 0.6 \cdot 10^{-3}$. The numbers near the data points represent the number of tune measurements needed to reach the specified β-function error tolerance.

has been applied, as a function of how precisely the β-function is reconstructed from the fit (error tolerance). For a large error in the β-function (≈ 0.8 m), the residual β-beating after the correction will be on average $\approx 4\%$. But, as the error of the β-function decreases (precision increases), so does the residual β-beating. For an error of the order of 0.1 m, the residual β-beating drops on average below 1%. This is due to the random

nature of the tune uncertainty since an increased precision in the β-function will result also to an increased accuracy of β-function with respect to the true value.

The compromise to reach a specific tolerance in the error of the fitted β-function, is the number of δk-Q_y points that are needed in the k-modulation measurement. The number that is noted above the data points of Figure 3.10 indicates the average number of tune measurements needed to achieve the fitted β error tolerance. For example, according to this statistical analysis, given a level of uncertainty in the tune measurement of $\sigma_Q = 0.6 \cdot 10^{-3}$, approximately 75 points will be needed for reaching a β error tolerance of 0.2 m. For the PSB this is not an unrealistic number of measured points. A typical super-cycle lasts less than one minute. So, a precise k-modulation measurement should not last more than about an hour.

Impact of random focusing errors

Data from previous runs of the PSB showed that focusing errors are present in the machine during normal operation. The sources of these errors can be of random nature and include field imperfections, magnet misalignments and fringe fields. These random focusing errors can excite the half-integer resonance and cause β-beating, similarly to the injection chicane perturbations.

If other random focusing errors are present in the machine, the injection chicane β-beating correction scheme that has been devised can degrade and not be very effective. The location and the strength of the random focusing errors can not be known a priori and so they cannot be easily included in the response matrix in a systematic way. For example, it can be that the random focusing errors distort the optics in a such a way that locally, at the positions of QDE3 or QDE14, the β-beating is very small. In this case, the k-modulation measurement can lead to the false conclusion that no random focusing errors are present, since locally no additional β-beating is recorded. Even if the β-beating of the random focusing errors is corrected experimentally in some way, there can be always residuals that are non-negligible.

Similarly to before, the k-modulation-based correction method was tested in simulations with the presence of both uncertainty in the tune measurement and random focusing errors. The focusing errors were randomly distributed in all of the focusing and defocusing quadrupoles of the PSB model lattice in MAD-X as integrated field errors. The strength of the field errors was sampled from a normal distribution centered at zero and with a standard deviation $\sigma_{kl}^{\text{random}}$.

Figure 3.11 shows again the residual β-beating after the correction method has been applied, as a function of the precision (error) in the fitted β-function, but with both uncertainty in the tune and random focusing errors of $\sigma_{kl}^{\text{random}} = 10^{-3}$ m^{-1} (in blue). Each data point is a statistical average over many simulations with the same parameters but different seeds in the distribution and strength of the random focusing errors. Here, a reduction of the fitted beta error measurement will not considerably reduce the β-beating after the correction since a high precision will not guarantee a high accuracy to the β-function perturbed by the injection chicane. The random focusing errors induce additional β-beating that might slightly or considerably change the perturbation at the

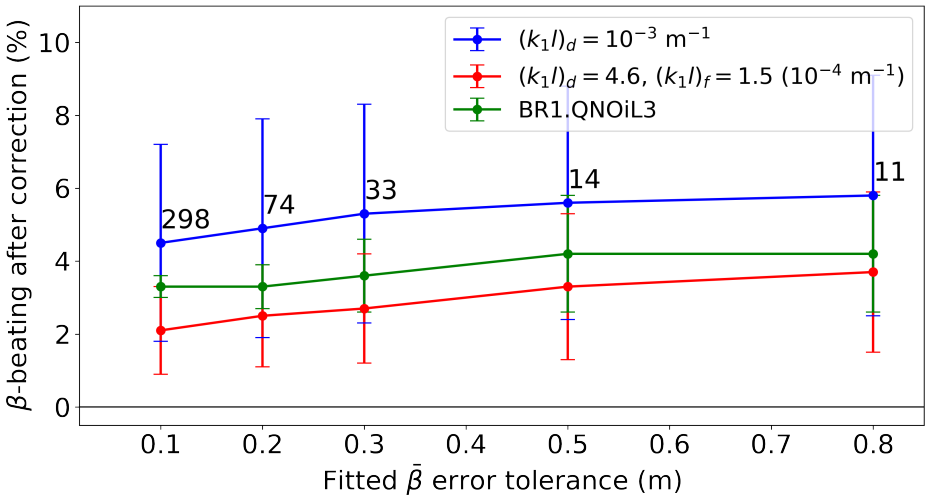

Figure 3.11: Residual β-beating after the correction as a function of the error in the fitted β-function when assuming $\sigma_Q = 0.6 \cdot 10^{-3}$ and including other random focusing errors. The numbers near the data points represent the number of tune measurements needed to reach the specified β-function error tolerance. Each color corresponds to different estimated distributions of random focusing errors.

observation points (at QDE3 and QDE14). For this $\sigma_{kl}^{\text{random}}$, the residual β-beating after the correction varies between 4-6% ($\pm$3%).

As in the tune uncertainty, data from previous years were analyzed in order to get a reasonable value for $\sigma_{kl}^{\text{random}}$. Estimating the $\sigma_{kl}^{\text{random}}$ is less evident since there are no direct measurements of the β-beating available. A kick-response study in the PSB from 2013 [42] revealed that the quadrupole errors have on average a strength of approximately $0.46 \cdot 10^{-3}$ m^{-1} for the defocusing quadrupoles and $0.15 \cdot 10^{-3}$ m^{-1} for the focusing quadrupoles. The statistical analysis of these random focusing errors is shown with red in Figure 3.11. Another estimation of the PSB β-beating was calculated by the half-integer compensation values of 2018. The quadrupole corrector values that compensate the half-integer resonance $2Q_y = 9$ were applied in the PSB model lattice in MAD-X, in order to get the β-beating wave that they induce. In that case, the same statistical analysis is shown in Figure 3.11 with green. In both cases the residual β-beating is smaller than 5%.

Impact of space charge

So far the analysis and testing of the method described above has been performed in MAD-X. The tunes in the k-modulation measurement have been extracted from the TWISS tables while the only observable has been the β-beating as defined in eq. 3.3. In order to include the effects coming from space charge and to evaluate possible beam losses or emittance growth, a realistic 3D particle distribution was used in the PSB model

and tracked with PyOrbit for 25 thousand turns at the injection energy of 160 MeV. The 25 thousand turns correspond to approximately 25 ms, which is well beyond the collapse of the injection chicane. To simulate the k-modulation measurement, the strength of QDE3 or QDE14 was shifted by δk for the full simulation, and the particles were excited with a dipolar kick every 500 turns. The tune was reconstructed using Fast Fourier Transformation (FFT) algorithms on turn-by-turn data of blocks of 500 turns. The same simulation was repeated with different δk settings, until the β-function throughout the fall of the chicane was reconstructed (like Fig. 3.5). A self-consistent 2.5D space charge solver was used [43].

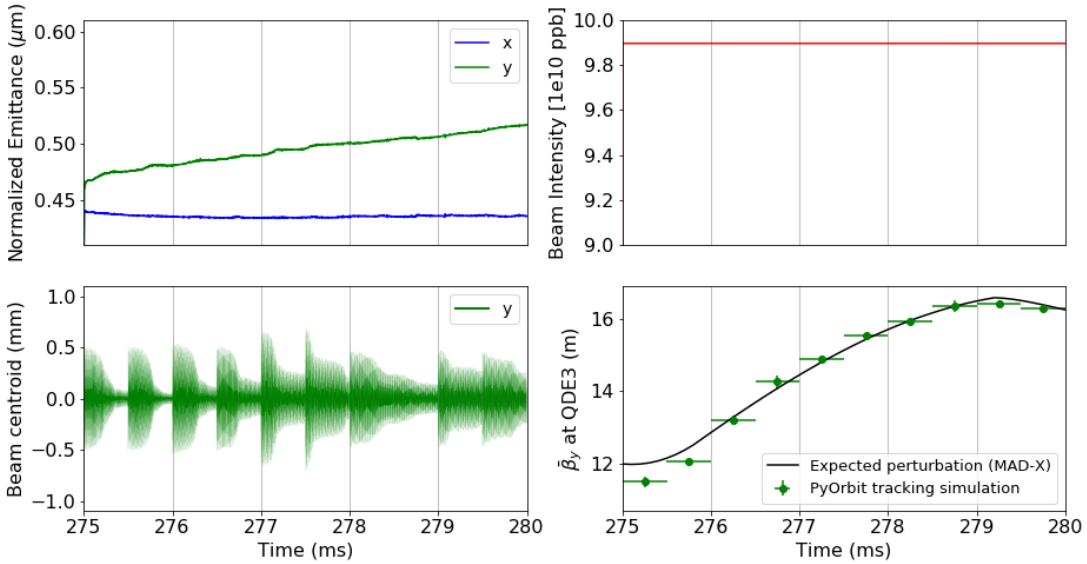

Figure 3.12: Top-left: simulation of the horizontal (in blue) and vertical (in green) emittance evolution throughout the injection chicane decay with PyOrbit. Top-right: beam intensity evolution of the same simulation. Bottom-left: average beam position (centroid) in the vertical plane while the beam receives a dipolar kick every 0.5 ms. Bottom-right: $\bar{\beta}_y$ reconstruction at the position of QDE3 using the turn-by-turn data from the space charge tracking simulations (in green) and expected perturbation from MAD-X (in black).

Fig. 3.12 summarizes the results of the tracking simulations. On the top-left plot, the emittance evolution throughout the fall of the chicane is shown. In the vertical plane (shown in green), the emittance growth is below 10 % after the chicane collapse. By using a low intensity beam with approximately 10^{10} protons, the space charge induced tune spread is smaller than 0.03. In this case, no losses were observed throughout the simulation, as shown in the top-right plot. On the bottom-left plot, the turn-by-turn beam centroid in the vertical plane is shown. The dipolar kicks are applied every 0.5 ms (corresponding to approximately 500 turns at injection) and the beam decoherence takes similar times. Finally, on the bottom-right plot the reconstructed from the FFT analysis

$\bar{\beta}_y$ function at the location of QDE3 is compared with the expected from MAD-X. With the exception of the points near the injection, the reconstruction is excellent throughout the full decay of the chicane.

Space charge is not expected to degrade the correction method, especially when keeping the beam intensity low. On the other hand, the beam must be intense enough so that the turn-by-turn BBQ pickup signal is stronger than its noise level. Therefore, in the operational scenario, a compromise for the beam intensity is needed to be found experimentally.

Other sources of uncertainties

Additional simulation tests were carried out to assess the robustness of the correction method. For example, calibration errors were included in the quadrupole δk-shifts and noise was added in the turn-by-turn data of the tracking simulations. In both cases, the residual β-beating after the correction was small. The sextupolar component of the BSWs was also changed from the expected value (see Fig 3.1). In the extreme case at which the sextupolar component is twice as large, the residual β-beating increases only to approximately 1%.

Overall outcome

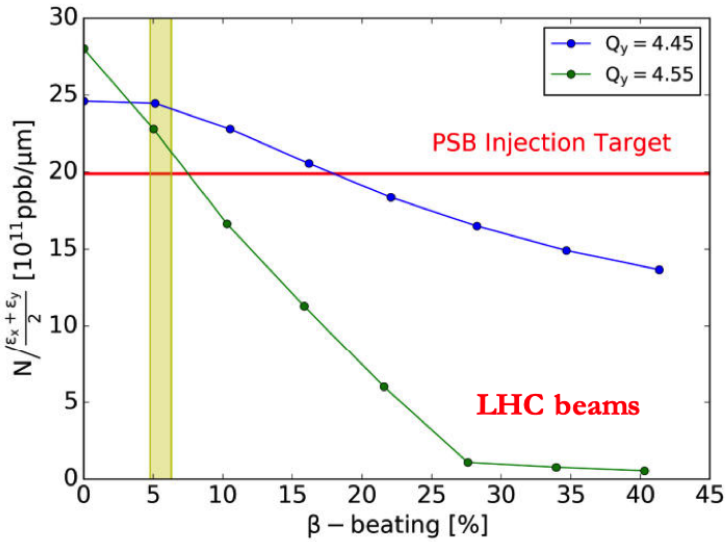

Figure 3.13: Simulation of the expected beam brightness as a function of the residual β-beating in the PSB. The blue points correspond to an injection at $Q_y = 4.45$ and the green points to an injection at $Q_y = 4.55$. The LIU target brightness is shown with the red line. A beam brightness within the targets is expected with a residual 6 % β-beating (highlighted yellow area). Graph from [44].

The k-modulation-based method for measuring and correcting the injection chicane β-beating proved to be very robust and reliable for the PSB. By considering realistic levels of uncertainty in the tune measurement and in the presence of random focusing errors and also by minimizing the effect of space charge, the method is expected to reduce the RMS β-beating on average to less than 6%. This is a considerable improvement comparing to the expected 100% β-beating at the vertical tune of $Q_y = 4.44$ (Figure 3.2). Based on tracking simulations [44], a 6% residual β-beating was considered acceptable for the LIU beam brightness target of the LHC-type beams at injection of the PSB, as shown in Fig. 3.13.

3.3 Beta-beating Measurement and Correction

Following the two-year long shutdown (LS2) of the CERN accelerators, the upgraded PSB took beam for the first time in December 2020, three months later than scheduled due to the Covid-19 pandemic. The initial goal of the PSB beam commissioning was to re-produce the different beams that were available in Run II. Only after, the machine would try to make use of the new capabilities that came with the LIU upgrade and push the beam performance.

The optics measurements were one of the first steps of the beam commissioning. After the steering the beam in the H^- injection, the establishment of the closed orbit and the beam capture, the optics measurements took place in parallel to other commissioning activities such as the working point setting and the resonance compensation. The measurement and the correction of the injection chicane β-beating using the k-modulation technique, as described in the previous sections, was part of these optics measurements.

3.3.1 Operational implementation

The operational implementation of the k-modulation-based method for correcting the injection β-beating was not trivial. Since the injection perturbations change during the fall of the chicane, the quadrupole setting had to be static, in the sense that a single shift in the strength (δk) of QDE3 or QDE14 was programmed for the full duration of the chicane. To construct the δk-δQ plot of the k-modulation, multiple cycles with different k-settings were needed. Furthermore, for a particular k-setting, the tune was measured multiple times during the cycle. The response of the tune for a particular k-setting will depend on the injection perturbations that occur at the time of the measurement, and so the data needed to be carefully disentangled.

In order to automatize and ease the data acquisition and analysis, a dedicated application was developed with its own graphical user interface. The application was developed in Python, using the PyQT5 libraries [45] and the acc-py environment and deployment tools [46]. The purpose of the application was to perform the k-modulation measurement and do the full analysis of the dynamic correction needed for the injection chicane β-beating on-line. The application was developed in such a way that it could be extendable for the β-function measurement at the low energy quadrupoles of the PS. A

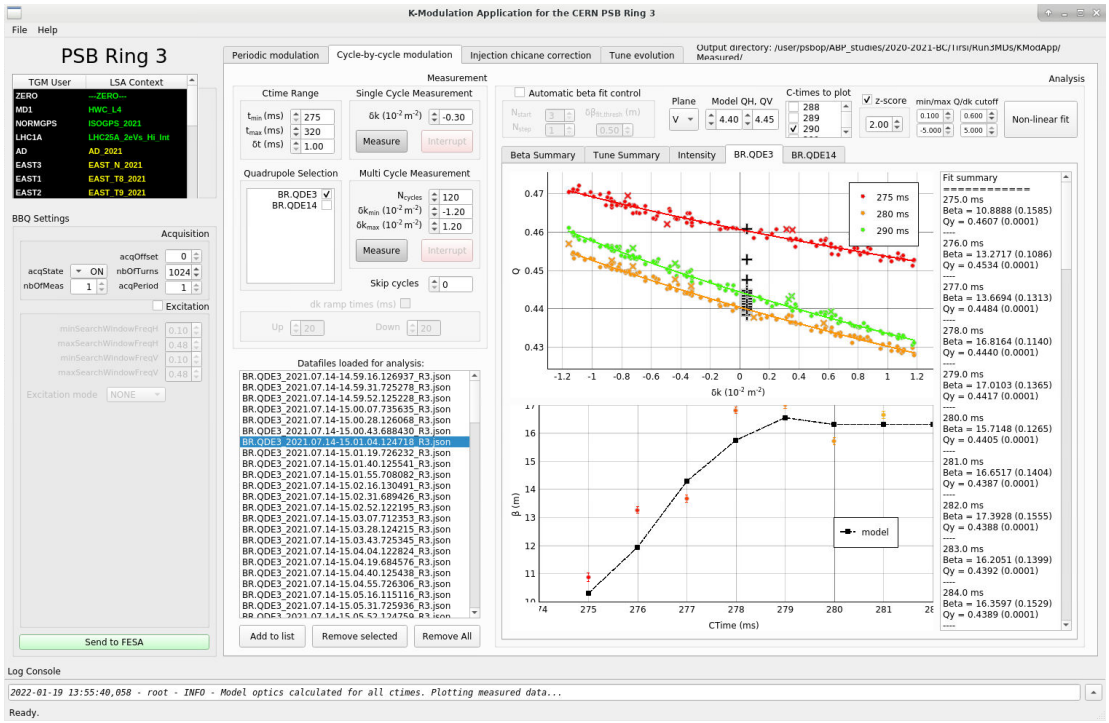

Figure 3.14: Screenshot of the main window of the k-modulation application in the PSB.

screenshot of the main window for the PSB ring 1 is shown in Fig. 3.14.

The k-modulation application allows a number of different functions. In the cycle-by-cycle modulation, the k-setting (δk) is applied along a time interval during the cycle (static) and the tune is measured multiple times during that interval. The number of cycles to measure for different k-settings or the β error tolerance (as defined in section 3.2.3) can be specified. A periodic (sinusoidal) k-modulation setting and measurement is also possible. The periodic k-modulation allows the β-function measurement within one cycle of the PSB but only after the fall of the injection chicane in which there are no more dynamic effects that can change the optics. Finally, this application allows corrections of the tune ('tune flattening') that can be not only due to the injection chicane errors but also due to any other perturbations.

The tune measurement is not performed by the k-modulation application itself, but it communicates with the FESA class of the BBQ system (see Chapter 2.2.4). The minimum interval at which the tune measurement can be performed is every 1 ms. This limits the tune measurement to only five times during the fall of the injection chicane. Furthermore, during these 1 ms intervals, the β-beating changes considerably, and so the uncertainty in the calculated β-functions is expected to be relatively large. Finally, to avoid any dependence on the relative phase advance between QDE3 and QDE14, during the k-modulation measurement each of the two quadrupoles was modulated individually.

3.3.2 2021 measurements

The first beam commissioning of the PSB after LS2 took place in the beginning of 2021. The initial working point of the LHC-type beams was set at $(Q_x, Q_y) = (4.38, 4.43)$. The β-beating measurements at injection with k-modulation were first performed on a non-accelerating cycle (flat-bottom). Following the progress of the RF-team, the measurements were repeated on a nominal (energy-ramp) cycle. The transition from the flat-bottom to the nominal cycle was slowed down by the non-ideal behavior of the current regulation of the defocusing quadrupoles. The encountered strong tune oscillations at the beginning of the cycle made the k-modulation measurement very difficult. Only after the improvement of the power converter regulation [47], the β-beating measurement could take place. This section will focus only on the nominal cycle, since the results from the flat-bottom cycle are very similar.

A typical k-modulation measurement at QDE3 of the PSB ring 3 is shown in Figure 3.15. The different colors correspond to different times during the fall of the chicane. The reconstruction of the vertical β-functions is done by fitting the measured $(\delta k, Q_y)$ pairs with Eq. (3.7). The fluctuation of the tune measurement is of the order of $5 \cdot 10^{-3}$, which is higher than initially predicted, and thus more than 100 different cycles, i.e. different k-settings, were needed to get a precision in the β-function of less than 0.2 m. The programmed vertical tune is constant at the value of $Q_y = 4.44$, but at $\delta k = 0$ the actual tune is perturbed due to the focusing errors from the injection chicane. Beam losses start to appear for set vertical tunes higher than $Q_y = 4.45$. K-modulation data were acquired for the quadrupole QDE3 and all of the four PSB rings. The results for the different PSB rings are very similar.

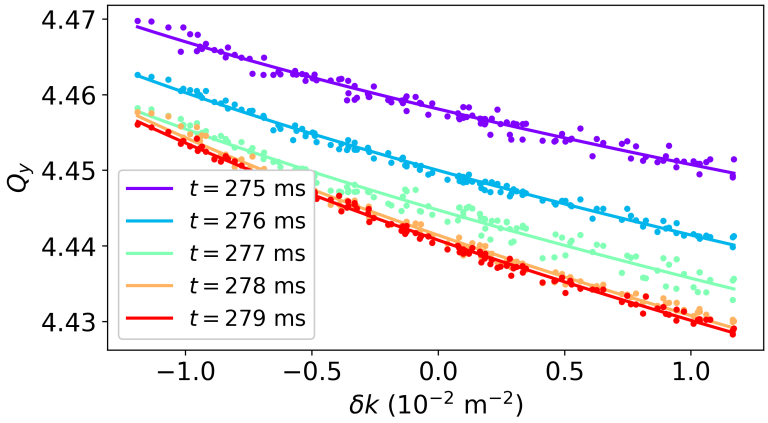

Figure 3.15: K-modulation data for ring 3 of the PSB. Each color corresponds to a different time of the cycle after injection.

The average β-function at the positions of QDE3 and QDE14 as a function of time is shown on the left plot of Fig. 3.16. The different colors correspond to measurement from the different PSB rings. The black line represents the β-distortion due to the injection

chicane perturbations, as expected from the model of Fig. 3.1 at the working point of $(Q_x, Q_y) = (4.39, 4.44)$, for which the measurements were performed. After $t = 280$ ms, the chicane has been fully collapsed and so the β-function should remain constant and equal to the unperturbed value (which in this case is 16.26 m). On the right plot of Fig. 3.16, the local β-beating of the same dataset is plotted as a function of time.

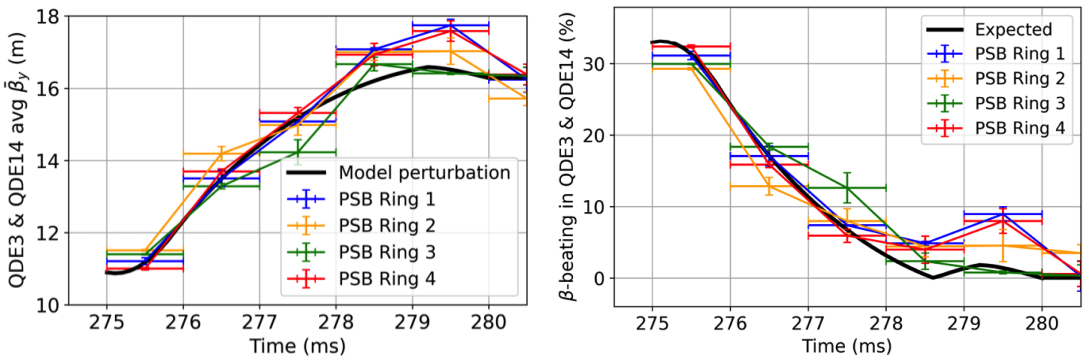

Figure 3.16: Local perturbation in the $\bar{\beta}_y$ of QDE3 and QDE14 (left). Local β-beating at QDE3 and QDE14 (right).

The agreement between the expected and the measured distortion in the optics, within the uncertainty of the measurement, is excellent. This suggests that the modelling of the injection chicane error sources and the machine lattice is very good. Some ring-to-ring differences are also observed, with the external rings appearing to have larger than expected values for the β-beating between 278 ms and 280 ms where the sextupolar component is more dominant than the edge focusing. This could be caused by stronger eddy currents at the magnets of these rings.

The measured local β-beating was interpolated to the response matrix, as described in section 3.2.2, and the dynamic β-beating correction was calculated and applied to QDE3 and QDE14. Furthermore, the tune perturbations caused by the injection chicane were also improved by applying additional corrections to all the focusing and defocusing quadrupoles of the PSB. The 2021 dynamic correction functions are shown in Figure 3.17.

After the correction was applied, the local β-beating was then once more measured, in a similar way as before. The result is shown in Fig. 3.18. On the left graph, it can be observed that the vertical β-functions are roughly constant, with values very close to the unperturbed value, throughout the entire duration of the injection chicane decay. This clearly shows the effectiveness of this approach for the minimization of the β-beating around the machine, which is shown on the right graph. The β-beating dropped from more than 30% to values smaller than 3%.

The β-beating correction functions have been calculated for a specific working point. Measurements and simulations show that for small tune changes, the sensitivity of the correction on the exact tune is not significant. Thus, the same dynamic β-beating correction has been used for all vertical tunes up to $Q_y = 4.47$ and only the tune

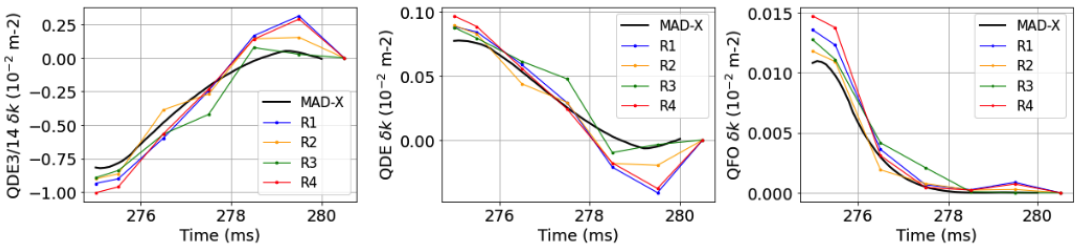

Figure 3.17: The β-beating dynamic correction functions for QDE3 and QDE14 (left), the tune correction applied in all QDEs (center) and the tune correction applied in all QFOs (right).

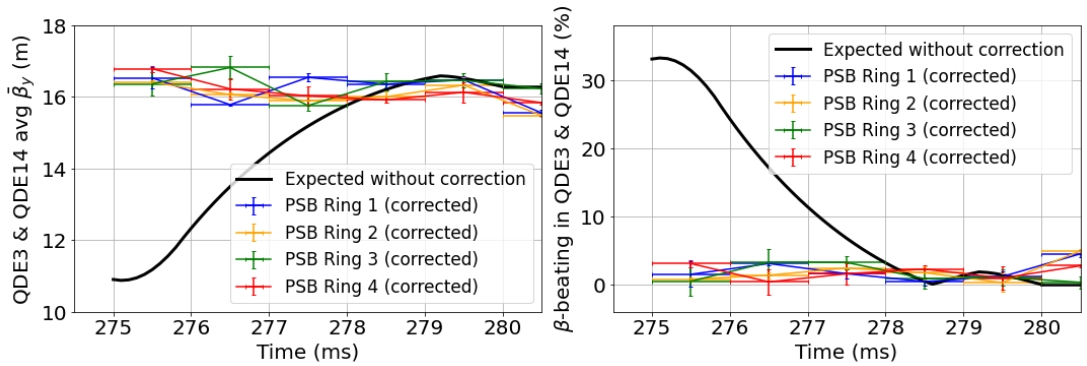

Figure 3.18: Local perturbation in the $\bar{\beta}_y$ of QDE3 and QDE14 after the correction (left). Local β-beating at QDE3 and QDE14 after the correction (right).

correction has been adjusted accordingly for each working point. In order to approach even closer to the half-integer resonance and eventually cross it, the injection chicane perturbation must be corrected iteratively. Another set of measurements was followed in order to calculate and apply a second iteration of correction functions, but this did not give noticeable improvements. The correction of the half-integer resonance excited by error sources other than the injection chicane was also applied.

3.3.3 2022 measurements

Following the Year-End Technical Stop (YETS) of 2021, the LHC injectors accelerators restarted gradually in January 2022. The injection β-beating measurement and correction was repeated once more, with similar results. Figure 3.19 shows the tune and local β-beating as a function of time, after the dynamic correction functions were recalculated and applied. The tune perturbations have been minimized (left graph) and the residual β-beating after the correction is again of the order of 3% (right graph).

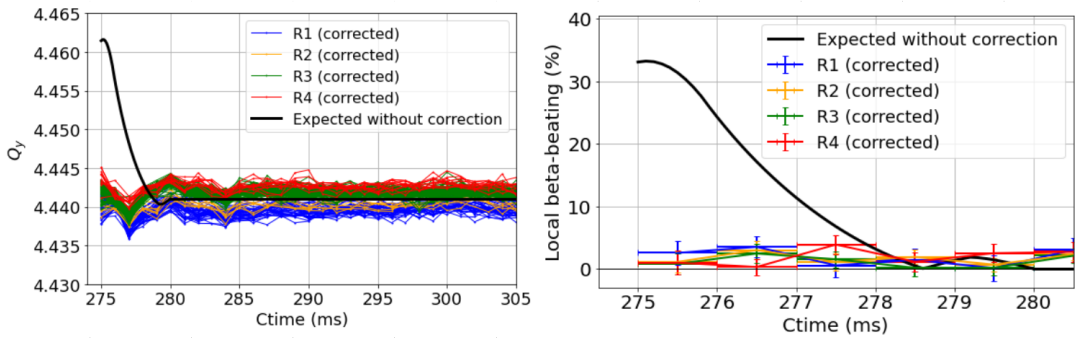

Figure 3.19: Vertical tune (left) and local β-beating (right) as a function of time after the correction (2022 measurements).

3.4 Impact on Beam Parameters

The need for the PSB to operate close to the half-integer resonance is due to the fact that the beams at injection energies suffer from a large space charge tune spread. Above a certain intensity, particles from the beam core reach the strong resonances at the integer tunes $Q_{x,y} = 4.0$ causing an increase in the emittance. By moving the working point further away from the integer, i.e. closer to the half-integer resonance, the emittance increase for the same intensity becomes smaller. Thus, larger intensities can be accumulated for the same emittance, resulting in a beam with a higher brightness.

3.4.1 Intensity

In order to observe the effect of the corrected β-beating, the beam intensity was measured near injection for different vertical betatron tunes. In the PSB, the beam intensity is measured with BCTs (see section 2.2). Figure 3.20 shows the beam intensity for different vertical tunes with (green bars) and without (red bars) the β-beating correction. For tunes far from the half-integer resonance, the effect of the correction is insignificant, since the β-beating is very small. When the half-integer is approached, the β-beating increases considerably and if not corrected it leads to beam losses. At the vertical tune of $Q_y = 4.46$ more than 25% of the beam intensity is lost, while for $Q_y = 4.47$ the beam is lost completely. With the correction enabled, the beam fully survives for tunes much closer to the half-integer resonance.

The highest set working point at which the beam was stable was for a tune set at $Q_y = 4.475$. Setting the tunes to even higher values, the beam is fully lost even with the β-beating correction enabled. In reality, due to calibration errors in the quadrupole magnets, the set and the actual (measured) tune differ by approximately 0.01. Therefore, the beam remains stable up to $Q_y \approx 4.485$, much closer to the unstable region of the half-integer resonance.

Although the beam intensity is stable for $Q_y \approx 4.485$, at this vertical tune the beam suffers from large non-Gaussian tails, especially for higher intensities. The vertical

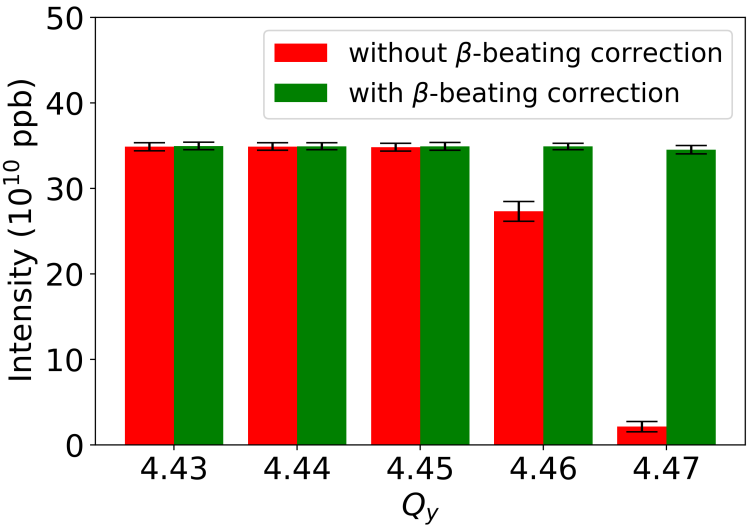

Figure 3.20: Intensity with (green) and without (red) the injection chicane dynamic β-beating and tune correction applied as a function of the set vertical tune.

chromaticity, which is uncompensated, drives particles to the half-integer resonance and thus beam halo can be created. For this reason, operationally the tune is set to $Q_y = 4.45$ or $Q_y = 4.46$.

3.4.2 Emittance

The emittance was also measured for various vertical tunes at flat-top energy, before extraction. The transverse beam profiles were measured with a wirescanner (WS). For the calculation of the emittance, the model β-function and the dispersion were assumed, while the momentum spread ($\delta p/p$) was measured using longitudinal tomography. A Gaussian fit was applied to all profiles. The measurements were performed with a beam close to the LIU intensities (approximately $300 \cdot 10^{10}$ ppb) at which the interaction of the beam with the resonances is enhanced.

Figure 3.21 shows the horizontal (left) and the vertical (right) emittance for three vertical tunes, with and without the β-beating correction enabled. In the horizontal plane, the emittance remains constant between 1.8 to 1.9 μm $\cdot$ rad, as expected. In the vertical plane, the emittance becomes smaller when moving away from the integer resonance. For this particular intensity, for a tune increase of 0.02, the emittance decreased by approximately 0.2 μm $\cdot$ rad. The effect is less pronounced for lower intensities.

It is important to mention that non-Gaussian overpopulated tails are observed in the vertical beam profiles of the beam and their origin is not yet fully understood. The shape of the transverse profiles and their evolution along the cycle is the subject of the next chapter.

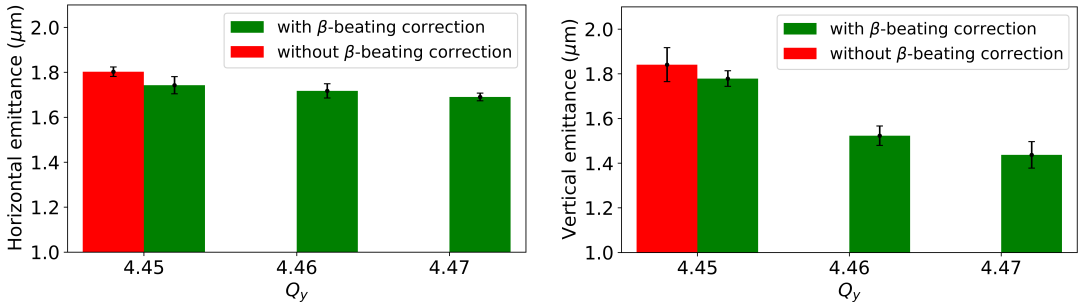

Figure 3.21: Horizontal (left) and vertical (right) emittances as a function of the vertical tune close to extraction ($t = 770$ ms). The emittances without the β-beating correction are shown only for $Q_y = 4.45$, since for the other vertical tunes there are significant losses which distort the profiles.

3.4.3 Brightness

In the PSB and the rest of the LHC injectors, the figure of merit which characterizes the performance of the LHC beams is the beam brightness, defined as the ratio of the intensity over the emittance (eq 2.8). The beam brightness is an an essential parameter for the LHC injectors as it represents how dense are the particles within the bunch. The higher the brightness, the higher the luminosity of the LHC and therefore more collisions take place per unit time. The aim of the LIU project was to upgrade all the LHC injectors in order to be able to deliver beams with double the brightness compared to pre-LS2 runs, as required by the HL-LHC project.

Figure 3.22 summarizes recent brightness measurements for different configurations and compares them with the brightness curve before the LIU upgrades (orange), for which at an intensity of $300 \cdot 10^{10}$ ppb the emittance is approximately 3.5 μm. The data presented in blue were acquired after the LIU upgrades, during the initial phase of the beam commissioning (March 2021), when the injection chicane β-beating correction, the resonance compensation schemes and the tune evolution were not yet fully optimized. The beam brightness in this initial phase was already very close to the LIU specifications, with an emittance of 1.8 μm for an intensity of $300 \cdot 10^{10}$ ppb.

The latest results (August 2021), including the injection chicane beta-beating correction, the optimised compensation schemes of the third and fourth order resonances, and the working point and tune evolution optimisation (higher tune plateau at injection and Q_x=4.40, Q_y=4.46), are shown in green. At an intensity of $300 \cdot 10^{10}$ ppb, the emittance is smaller by approximately 0.2 μm compared to the data of March 2021 (blue). It can be seen that the brightness can exceed the LIU target (black dashed line), as was predicted from the simulations (Fig. 3.13). The brightness results of 2022 are almost identical.

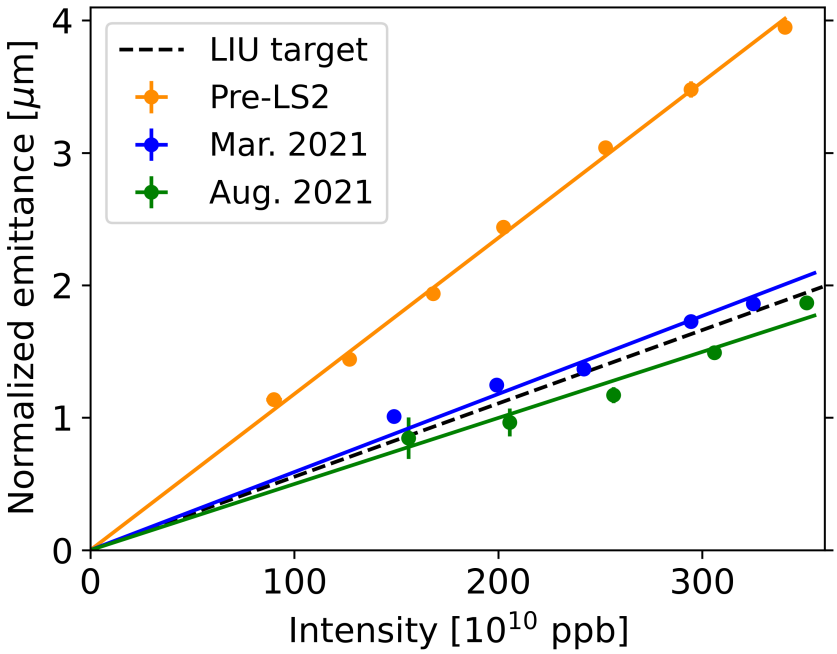

Figure 3.22: PSB brightness curves (emittance versus beam intensity) in ring 3. Data before the LIU upgrades in orange, early commissioning stages after LIU upgrades in blue (March 2021), optimized brightness in green (August 2021) and LIU target with the black dashed line.

3.5 Summary and Conclusions

A strong vertical β-beating is induced by the magnets of the H^- injection chicane after the LIU upgrades in the PSB. A method to identify and dynamically correct this β-beating was presented. This method consists of using k-modulation to measure the induced optics distortion at the positions of two individually powered quadrupoles and then to interpolate these values to a model-based response matrix. The method was employed during the PSB beam commissioning after the LIU upgrades. The injection chicane β-beating was measured at the expected levels and then corrected using the defocusing quadrupoles QDE3 and QDE14. The correction allowed a stable operation of the beam with working points closer to the half-integer resonance $2Q_y = 9$. This mitigated the interaction of the beam with the systematic resonances of the PSB at the integer tunes ($4Q_x = 16$ and $4Q_y = 16$) through the space charge tune spread, thus reducing the emittance and increasing the brightness of the LHC beams.

The brightness performance of the PSB exceeding the LIU target is a very important achievement that not only represents the success of the LIU upgrades but also shows how good is the understanding and modelling of the accelerator. This accomplishment has encouraged additional optimization studies to further improve the correction of the

focusing perturbations and to raise the vertical tune above the half-integer resonance with the goal to increase the beam brightness even further. This work is presented in detail in Chapter 6.

Chapter 4

Optimization of the Transverse Beam Profiles

4.1 Modelling of Particle Distributions

Following the implementation of the LIU project, the PSB delivered beams that were well within the project's requirements. The optimization of the resonance compensation schemes [22] and tune evolution along with the beta-beating compensation contributed to an increased beam brightness, going beyond the initial predictions. The shape of the particle distributions in the transverse planes is very important for the calculation of the beam emittance and eventually the beam brightness. In most cases, the transverse particle distributions follow Gaussian ("normal") shapes. The standard deviation of these distributions (1σ) define the horizontal and vertical RMS beam sizes σ_x and σ_y. The normalized emittance is then calculated using:

$$\epsilon_{x,y} = \frac{\sigma_{x,y}^2}{\beta_{x,y}} \beta_r \gamma_r, \tag{4.1}$$

where $\beta_{x,y}$ is the β-function at the location of which the $\sigma_{x,y}$ was measured and β_r, γ_r the relativistic factors of the beam. The case in which dispersion is not zero and the transverse motion is coupled to the longitudinal motion is discussed in section 4.7.

In some cases, the particle distribution might slightly differ from a Gaussian shape. For example, it has been observed that the high-brightness beam profiles of the PSB have tails that differ from the ones of a Gaussian distribution. In this study, we will refer as "beam core" the particles that fall below 1σ of a Gaussian distribution and "beam tails" the particles that go beyond 1-2σ. In the PSB, overpopulated beam tails (compared to Gaussian tails) appeared to be present mostly in the vertical plane both at injection and at extraction energies. In an attempt to understand the origin and evolution of the observed tails, systematic profile measurements were performed for different machine and beam configurations using Wire Scanners (WS).

To characterize bunch profiles that follow a non-Gaussian shape, the q-Gaussian function (see Appendix B) was used. The q-Gaussian is a generalized Gaussian function

that incorporates a parameter q to model the weight of the distribution's tails. For $q = 1$, the q-Gaussian distribution coincides with a Gaussian distribution, for $1 < q < 3$ the distribution's tails are overpopulated compared to a Gaussian, while if $q < 1$ the tails are underpopulated. For example, for $q = 1.5$ approximately 7.5 % of the beam particles fall outside an Gaussian distribution with similar σ (see Figure B.3). The q-Gaussian function has been used in the past to model non-Gaussian beam profiles in the LHC [48]. The advantage of the q-Gaussian function is that with a single parameter it covers both Gaussian and near-Gaussian shapes and can be easily implemented in a code to fit measured beam profiles. Throughout this thesis, the q-factors that are the result of fitting measured profiles with a q-Gaussian function will be used as an observable for the beam tail population.

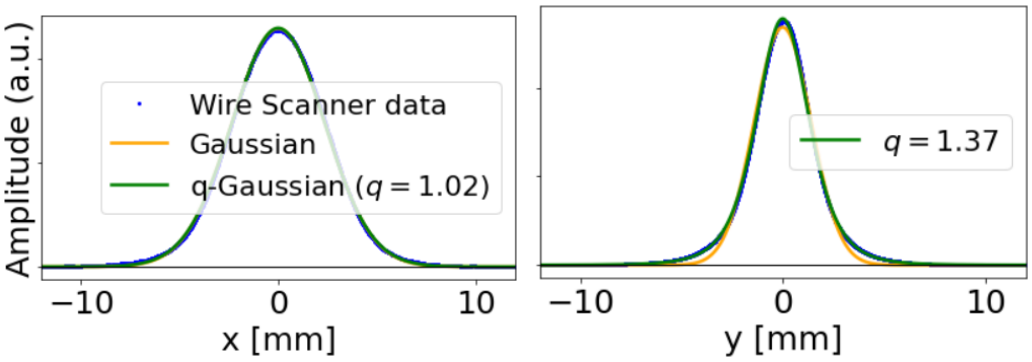

Figure 4.1: Ring 3 horizontal (left) and vertical (right) beam profiles of an LHC25-type beam close to extraction ($t = 770$ ms) in blue, Gaussian and q-Gaussian fits in orange and green respectively.

Figure 4.1 shows an example of the transverse beam profiles close to extraction of the PSB Ring 3 for a bunch population of $N_b \approx 270 \cdot 10^{10}$ protons. The profiles are modelled with a Gaussian (in orange) and a q-Gaussian distribution (in green). It can be seen that in the vertical plane (right) the tails are overpopulated with a corresponding q-factor of 1.37, while in the horizontal plane (left), the tails follow closely a Gaussian distribution ($q \approx 1.0$).

Overpopulated beam tails can lead to beam losses in the downstream machines of the accelerator complex and eventually reduce the beam brightness. In order to investigate the possible sources of beam tail enhancement and to eventually improve the quality of the delivered beams, a measurement campaign was initiated. Beam profiles were acquired for different beam intensities, working points and energies during the acceleration cycle. This chapter presents the results of these measurements and the comparison to simulations [49]. The way the WS impacts and reconstructs the beam distribution is also addressed. Although mostly profiles from the PSB ring 3 will be shown, the results are similar in the other PSB rings.

4.2 Beam Tails at Injection

Non-Gaussian beam tails are observed already at injection energies of the PSB. A typical vertical beam profile close to injection, for a low bunch population of $N_b \approx 10 \cdot 10^{10}$ protons, is shown in Fig. 4.2. At this beam intensity, the space charge tune spread is expected to be smaller than 0.02. The working point of this measurement is set to $(Q_x, Q_y) = (4.17, 4.23)$, which is a resonance free region, up to the fourth order of resonances. Still, under these beam conditions, the beams are overpopulated, with a q-factor of 1.5. Note that the tail population is not symmetric with respect to the beam core. At low beam energies, heavier tails are observed on one side of the profile compared to the other. This effect has been seen in previous studies [50], and suggest that the main contributor for this is the measuring instrument itself. For this reason, an attempt to quantify and remove the undesired effects that the WS causes to the beam profile was first made and is presented in the following section.

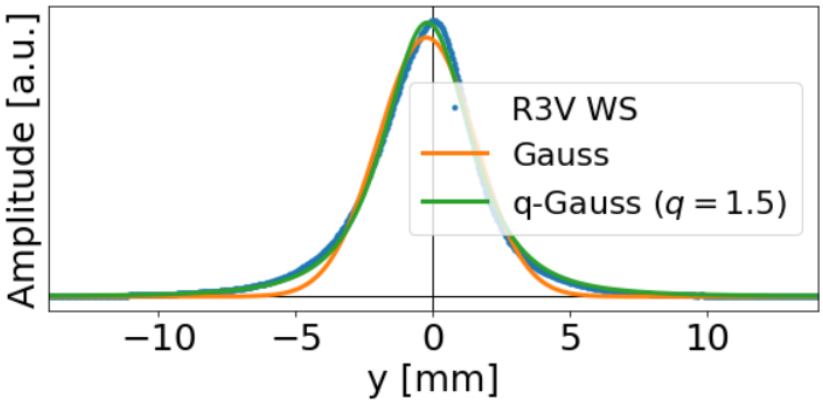

Figure 4.2: Ring 3 vertical beam profile of an LHC25-type beam close to injection ($t = 290$ ms) in blue, Gaussian and q-Gaussian fits in orange and green respectively.

4.3 Scattering on the Wire of the Instrument

The transverse beam profile measurement is performed in the PSB with a Wire Scanner (WS) which was briefly discussed in Section 2.2.3. Figure 4.3 shows an illustration of a WS measurement in the vertical plane. The thin carbon wire (orange line) physically rotates and intercepts the beam (black dots) as it circulates the accelerator. The wire rotation is much slower than the beam revolution. During the wire rotation, the beam does thousands of revolutions and thus its particles interact with the wire multiple times. The beam-wire interaction generates secondary particles (purple lines) that create a detectable signal. The beam profile is reconstructed by plotting the wire vertical position (y-position) versus the detectable signal that is proportional to the number of the beam particles the wire interacted at each turn (i.e. proportional to the vertical

beam density). The clockwise rotation of the wire is usually referred as the 'IN' scan and the anti-clockwise rotation of the wire as the 'OUT' scan. In the PSB, the WS measurement can be performed only twice within the cycle: once with the 'IN' scan and once with the 'OUT' scan.

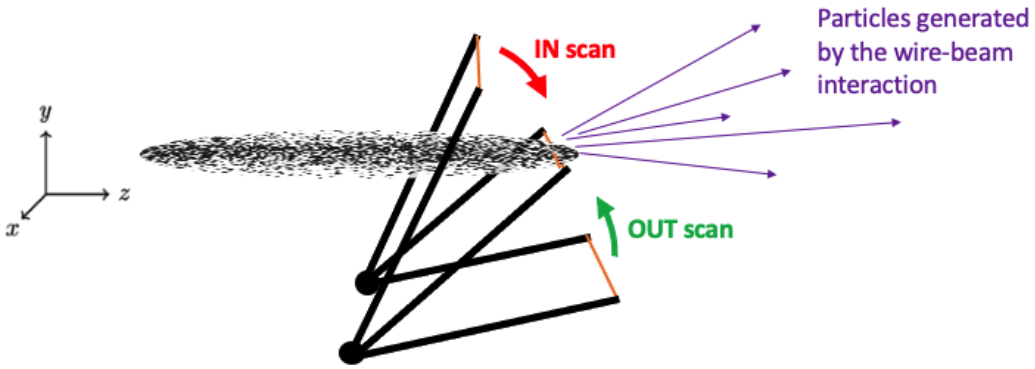

Figure 4.3: Illustration of the profile measurement performed with a WS. The thin wire (in orange) physically rotates and intercepts the beam (black dots). The generated particles from the beam-wire interaction (purple arrows) create a detectable signal. The 'IN' scan corresponds to the clockwise rotation of the wire and the 'OUT' scan to the anti-clockwise.

The turn-by-turn beam-wire interaction can be strong enough that may deflect the particle from its nominal orbit. This process is approximated with the 'Multiple Coulomb Scattering' [51] in which the beam particles intercepting the wire at each turn undergo many small-angle deflections. This results in the change of the phase space angle of the beam particles without necessarily changing their energy and position. Overall, this scattering process will induce an increase in the emittance and modify the particle distribution. In the context of understanding the observed overpopulated tails, the effects of the wire to the beam were studied at the injection energy of the PSB using both measurements and simulations.

4.3.1 Simulation model of the scattering

In order to study the effects of the WS on the beam, a model that simulates the wire scan process was implemented. In this model, the PSB lattice is simplified to a one-turn map using the optics ($\beta_{x,y}$, $\alpha_{x,y}$, $Q_{x,y}$, D_x) at the position of the vertical WS (at 11L1). The beam is represented by a matched 2D particle distribution with fixed emittances ($\epsilon_{x,y}$) and momentum spread ($\delta p/p$). The distribution can follow a normal (Gaussian) distribution or have overpopulated/underpopulated tails (q-Gaussian). The moving wire is described by three parameters: a 1D array that corresponds to its vertical position (y-position) turn after turn during the scan, its average width (d_w) and its RMS scattering angle (Θ_{RMS}).

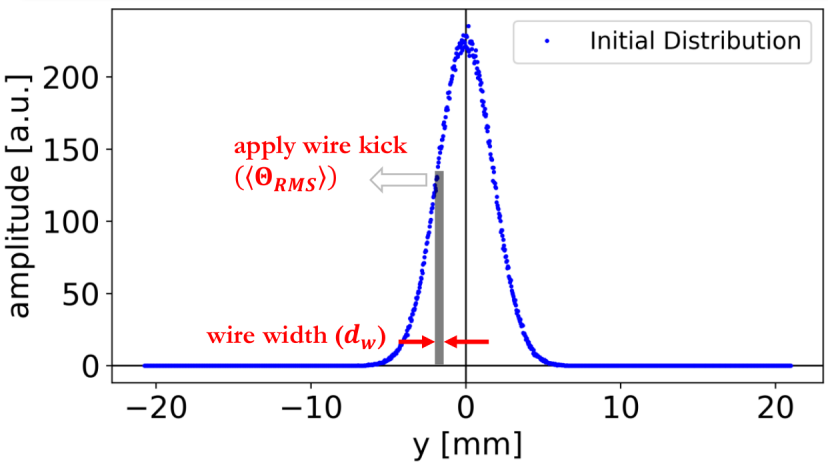

Figure 4.4: Illustration of the scattering process of the simulated wire scan. Turn-by-turn, the particles of an initial distribution (blue points) that intercept with the wire width (gray area) receive a momentum kick Θ_{RMS}.

The simulation of the scattering process is highlighted in Figure 4.4. The initial beam distribution (in blue) is tracked for many turns using the one-turn map of the PSB. Turn after turn, the simulated moving wire is vertically displaced with a certain speed. The particles that are intercepting with the moving wire at each turn (gray area in the graph) are scattered with an angle distribution because of the Coulomb scattering. The angle distribution is a normal distribution with $\sigma = \Theta_{RMS}$. The process is repeated until the full scan is completed. At the injection energy of the PSB, the wire scan takes more than 3000 turns to be performed. The interaction between the beam particles and the wire causes an increase in the beam size as it is explained in the following sections.

4.3.2 Scattering model benchmarking with measurements

The simulation parameters of the wire scattering are the wire displacement (or the wire speed), the wire width and the RMS scattering angle. To get a better understanding of the scattering effects from the simulations, these parameters have been calibrated using real profile measurements.

To get a realistic value for the wire displacement in the simulation is fairly straightforward. The difference between two consecutive wire position points in data of the real WS measurement is the actual wire displacement during that beam revolution. Thus, the wire displacement in the simulations is set to exactly the wire displacement of the measurement. The wire displacement is not uniform during the scan, meaning that the speed of the wire is not exactly constant.

For the purpose of finding realistic values for the wire width and scattering angle, a small experiment was performed in the PSB. On a non-accelerating cycle, the vertical profile was measured at $t = 500$ ms with the OUT scan. In this case, the IN scan was performed at $t = 270$ ms which is before the beam injection in the PSB. The OUT

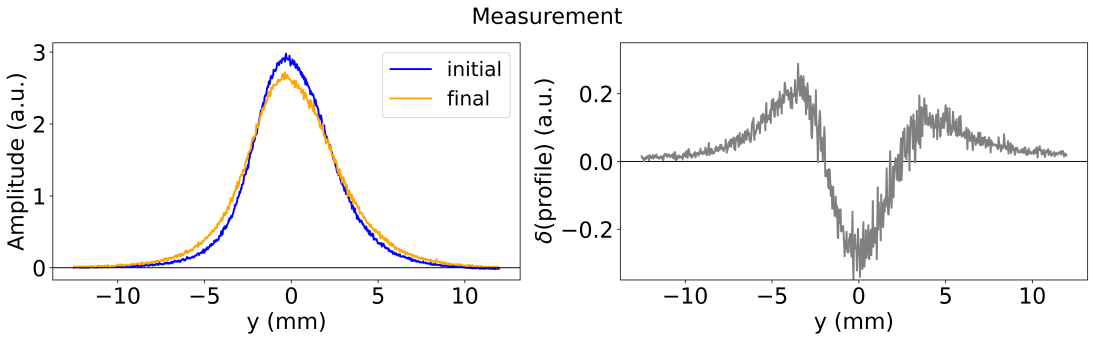

Figure 4.5: Left: measurement of the WS OUT scan without the IN scan (blue) and OUT scan with the IN scan (orange). The profiles have been averaged over multiple shots. Right: relative difference between the two profiles.

scan is shown on the left graph of Figure 4.5 in blue (initial). Then, the vertical profile was measured once more at $t = 500$ ms with the OUT scan, but this time the IN scan was performed at $t = 300$ ms, after the beam was injected. This profile, shown in the same graph in orange, is grown due to the effect of the IN scan. The relative difference between the two profiles, which is shown in the right graph of Figure 4.5, is the result of only the IN scan.

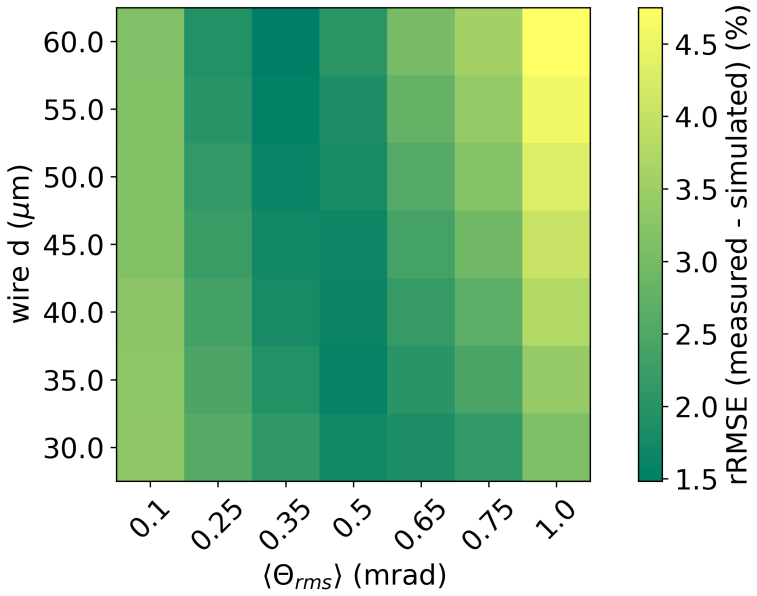

Figure 4.6: Parameter scan to benchmark the wire width and scattering angle of the simulated wire scanner.

The same experiment was repeated using the simulation model, with multiple values

of the wire width and the RMS scattering angle. As in the measurements, the OUT scan was simulated, with and without having performed an IN scan beforehand. The relative differences between the two profiles were computed and then compared to the relative differences of the measurement.

Figure 4.6 shows a parameter scan of the wire width and the scattering angle used in simulations. The horizontal axis shows the different values for the scattering angle that were used in the simulation and the vertical axis the different wire widths. The color corresponds to the relative Root Mean Squared Error (rRMSE) between the measured and simulated relative differences of the profiles:

$$rRMSE = \sqrt{\frac{\sum_{i=0}^{N}(y_{i,sim} - y_{i,meas})^2}{N\sum_{i=0}^{N} y_{i,meas}^2}}. \tag{4.2}$$

The rRMSE is used as a metric of similarity between measurement and simulation. The lower the RMSE is, the better the measured relative difference between the profiles (right graph of Figure 4.5) can be reproduced by the simulations.

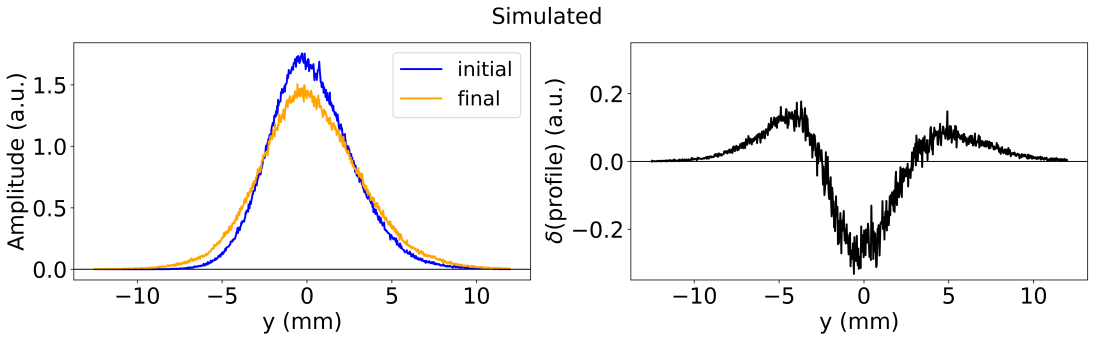

Figure 4.7: Left: simulation of the WS OUT scan without the IN scan (blue) and OUT scan with the IN scan (orange) for $d = 35$ μm and $\langle\Theta_{rms}\rangle = 0.5$ mrad. Right: relative difference between the two profiles.

The parameters that better match the measurements were 35 μm for the wire width and 0.5 mrad for the scattering angle. The simulated profiles for these parameters are shown in Figure 4.7 on the left and their relative differences on the right (in black). These relative differences are compared in Fig. 4.8 with the relative differences from the measurement (in grey) and are almost identical.

A second parameter scan was repeated around the values of 35 μm and 0.5 mrad with an increased resolution. The optimal parameters that were found in this second scan were $d_w = 38$ μm and $\Theta_{RMS} = 0.47$ mrad. These parameters will be used for the rest of the study. The wire width is very close with independent estimations which give a value of 34 μm.

The scattering angle value is valid only for the injection beam energy. For higher energies, the effect of the WS to the beam is expected to decrease and so the scattering angle will be smaller. Measurements for higher energies were not performed.

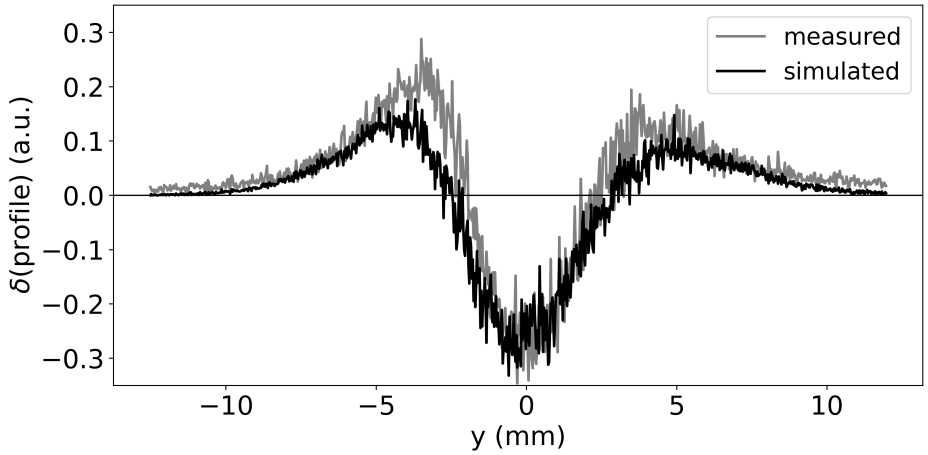

Figure 4.8: Relative differences between the measured profiles of Figure 4.5 versus the relative differences between the simulated profiles of Figure 4.7.

4.3.3 Beam effects of the scattering

The calibrated simulation model of the wire scan was used to study the different effects induced by the wire scattering. The asymmetric tail population of the measured profiles is well explained by the way the WS reconstructs the profile from its acquired signals. Figure 4.9 shows a simulation of an initial distribution, in blue, and the grown distribution after the simulated wire scan, in red. As mentioned before, the WS signal is proportional to the number of beam particles that the wire interacted with at each turn (proportional to the beam particle density). In this example, the simulated wire scan is performed from the negative y-values to the positive y-values ('left to right'). For the first few hundreds of turns, the WS signal coincides with the initial distribution. While the scan advances, more particles are being scattered by the wire, and the beam size dynamically increases. Towards the end of the scan, the beam size has already grown and so the WS signal coincides with the final grown distribution. This is why the signal recorder by the WS lies in between the initial and final distribution and will appear asymmetric with respect to the center.

Quantitative calculations are also possible with the calibrated simulation model of the wire scan. Figure 4.10 shows the normalized emittance increase $\delta\epsilon$ of the final distribution as a function of the normalized emittance of the initial distribution, as calculated using the simulation model. For the injection energy of the PSB, the emittance increase is constant and equal to approximately 0.35 $\mu\text{m} \cdot \text{rad}$. Since the emittance increase is constant, initial profiles with a low emittance will appear more asymmetric (since the relative growth in the profile is larger). Furthermore, the $\delta\epsilon$ seems to be independent of the shape of the initial distribution as it follows a similar trend even if the initial distribution has overpopulated tails of $q \approx 1.5$ (orange line). This result is valid only considering the simulation model and parameters that have been assumed

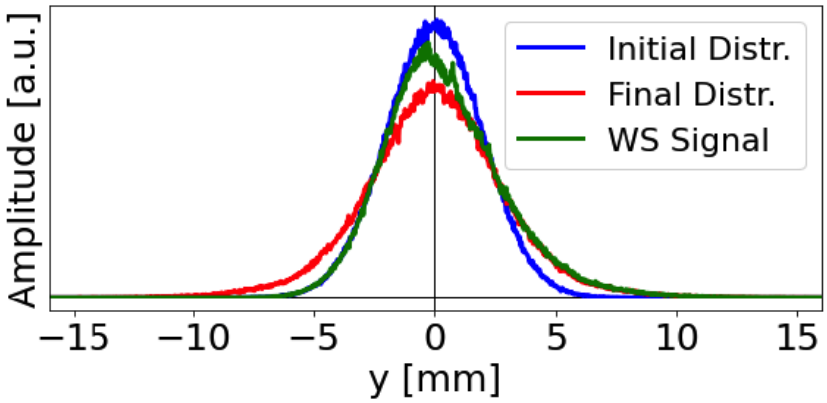

Figure 4.9: Simulation of the scattering effect of the wire to the beam. Initial distribution in blue, final grown distribution in red and simulated WS signal in green.

and are in a good agreement with the profile measurements. The analytical estimation of the emittance increase during the wire scanner measurement takes the form [51]:

$$\delta\epsilon_{x,y} = \frac{\pi d_w f_{\text{rev}}}{4v_{\text{wire}}}\frac{1}{2}\beta_{x,y}\Theta_{RMS}(\beta_r\gamma_r), \tag{4.3}$$

with d_w being the wire width, f_{rev} the beam revolution frequency, v_{wire} the wire speed, $\beta_{x,y}$ the Twiss β-function at the position of the wire scanner and β_r, γ_r the relativistic factors. For the beam parameters considered here, and for a wire speed between 20-25 ms^{-1}, this formula predicts an increase of $\delta\epsilon_y \approx 0.37$-$0.47$ $\mu\text{m}\cdot\text{rad}$.

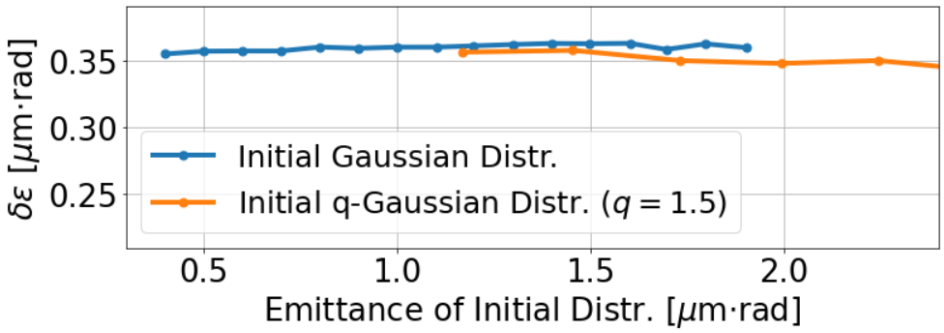

Figure 4.10: Emittance increase due to the WS scattering for an initial Gaussian (blue) and q-Gaussian (orange) distribution. Result from simulations.

Finally, the simulations showed that the beam tails seen not to be enhanced by the WS, meaning that particle distributions that already had tails before the wire scan, had similar or even less tails after the wire scan as well. Figure 4.11 shows such an example. The q-factor of the initial distribution is shown in blue for different beam sizes. The initial distribution is defined with having overpopulated tails ($q \approx 1.5$). The q-factor of

the final distribution, after the simulated wire scan, is plotted in red. This q-factor has only dropped to $q \approx 1.43$ which still corresponds to overpopulated tails. The green curve shows the q-factor of the simulated WS signal, which is also slightly below $q = 1.5$.

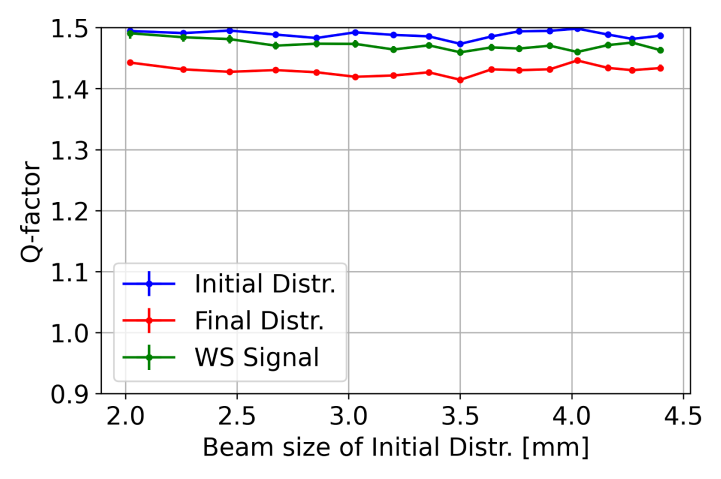

Figure 4.11: q-factor of the initial, final and WS signal distributions for different beam sizes. Result from simulations

All the estimations are valid only for the injection energy of the PSB at 160 MeV. At higher energies the WS scattering effects are expected to be smaller [51].

4.4 Comparison with the Linac4 Distribution

The study of wire scattering on the beam allowed the removal of the profile growth and asymmetries induced by the WS from the measured profile at injection (Fig. 4.2). This was done by iteratively finding an initial distribution that, when performing the wire scan using the simulation model, gives a WS signal identical to this measured profile. The initial distribution is symmetric, has a smaller RMS beam size and constitutes an improved reconstruction of the real particle distribution at the injection of the PSB. This is plotted in Fig. 4.12 in green. The profile still has tails that are overpopulated ($q \approx 1.54$).

Although the asymmetry of the tails is explained by the WS scattering, the tails themselves are not yet justified. For this reason, a comparison with the Linac4 distribution was needed. Thanks to the available profile monitors in the Linac4 transfer line, a realistic particle distribution could be reconstructed and used in simulation studies. Such a reconstructed particle distribution was tracked using PyORBIT for approximately 15 thousand turns in the PSB lattice model. The 15 thousand turns correspond approximately to the time period from injection at $t = 275$ ms to $t = 290$ ms of the PSB operational cycle. At $t = 290$ ms the WS measurement is performed in the PSB (green profile of Fig. 4.12). The tracking simulation was performed at the same

beam intensity ($N_b \approx 10^{10}$ ppb) and the same working point as of the measurement, $(Q_x, Q_y) = (4.17, 4.23)$ (resonance-free region). The space charge calculations and the foil scattering were also included in the simulation.

The result from tracking of the vertical profile is shown in Fig. 4.12 in purple with a corresponding $q \approx 1.46$. This profile is compared with the measured distribution in the PSB, of which the undesired WS effects have been removed, as described in the previous paragraphs. It can be observed that the two profiles have almost identical tails ($q \approx 1.5$ in both cases). This suggests that the vertical tails observed close to injection, for a low beam intensity and resonance free working point, seem to be mainly due to the injected distribution from Linac4.

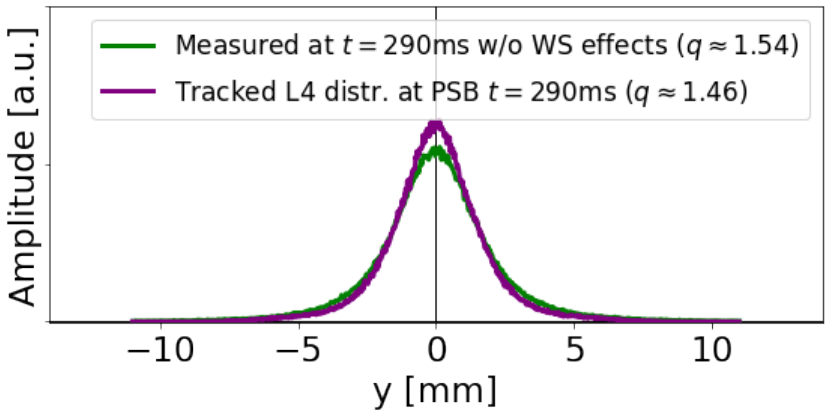

Figure 4.12: Comparison between Linac4 profile (purple) and PSB measured profile at $t = 290$ ms without the WS effects (green).

4.5 Impact of Intensity and Working Point

The vertical beam tails change when the beam intensity increases or the working point changes. Figure 4.13 shows how the q-factor of the vertical beam tails at injection decreases as the beam intensity increases, for the working point of $(Q_x, Q_y) = (4.17, 4.23)$. The acquired profiles have been averaged over five identical measurements and the error-bars represent the standard deviation of the applied q-Gaussian fits. While the intensity increases, the tune spread induced by space charge becomes stronger because the beam has initially the same transverse emittance at injection. Thus, low action particles that have the strongest space charge detuning, cross the resonance at integer tune $Q_y = 4$ causing an emittance growth (red points). Large amplitude particles do not interact with these resonances, leaving therefore the beam tails unchanged. Overall, the beam tails appear to become smaller (q-factor decreases) because the beam profile is dominated by the increased emittance of the beam core.

Resonances and space charge are closely linked with the beam tails. In fact, space charge induced periodic resonance crossing can result in losses, emittance growth or

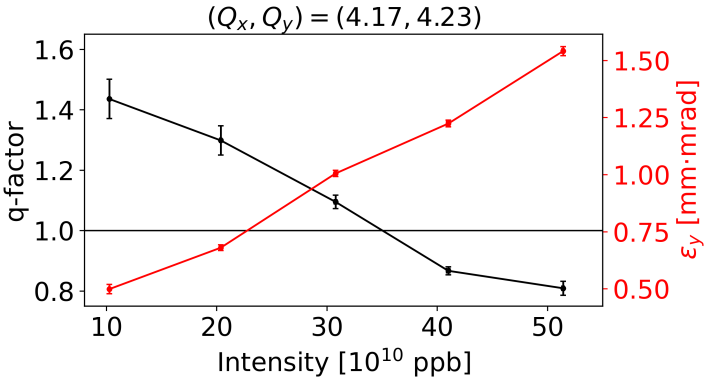

Figure 4.13: q-factor (black) and normalized emittance (red) of the vertical beam profiles at $t = 290$ ms as a function of the beam intensity. The tunes are constant at $(Q_x, Q_y) = (4.17, 4.23)$.

enhancement of the beam tails [25]. As shown in Figure 2.6, resonances up to fourth order are observed in the PSB. Although a global resonance compensation scheme has been developed through experimental and analytical studies, it is not possible to perfectly compensate all the resonances simultaneously.

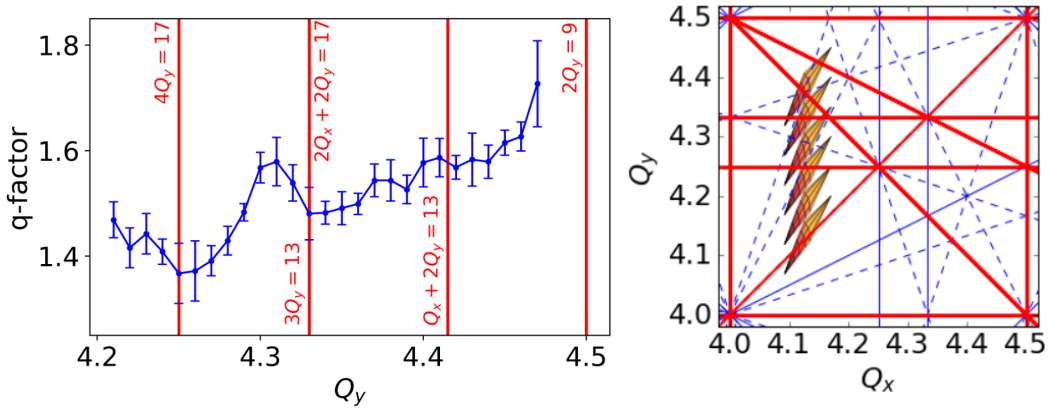

Figure 4.14: q-factor of the vertical profiles at $t = 290$ ms as a function of the vertical tune (left) and tune diagram (right). The beam intensity and the horizontal tune are kept constant.

Figure 4.14 shows how the tails change when injecting at different working points. Here, the beam intensity is fixed at $N_b \approx 20 \cdot 10^{10}$ ppb, as well as the horizontal tune at $Q_x = 4.17$. The tune diagram on the right shows some of the observed resonances in the PSB highlighted in red. An analytical estimation of the space charge tune spread, for the beam parameters used, was calculated using PySCRDT [52] and plotted at some of the different injected vertical tunes. The graph on the left shows the dependence of

the q-factor of the vertical profiles with respect to the vertical tune. For higher working points, the tails generally become stronger with the q-factor ranging between 1.3 and 1.7. A possible explanation for this is that for higher vertical tunes the beam may interact, through the space charge detuning, with multiple resonances at the same time.

4.6 Beam Tails Along the Cycle

In operational conditions, the high-brightness beams are injected in the PSB at the working point of $(Q_x, Q_y) = (4.40, 4.45)$ in order to mitigate the beam degradation from the strong space charge effects at injection energy. While the beam is accelerated and the space charge tune shift decreases, the tunes are dynamically changed towards the extraction working point $(Q_x, Q_y) = (4.17, 4.23)$ (top part of Fig. 4.15). The different resonances are crossed at different times and energies, which adds more complexity to the dynamics.

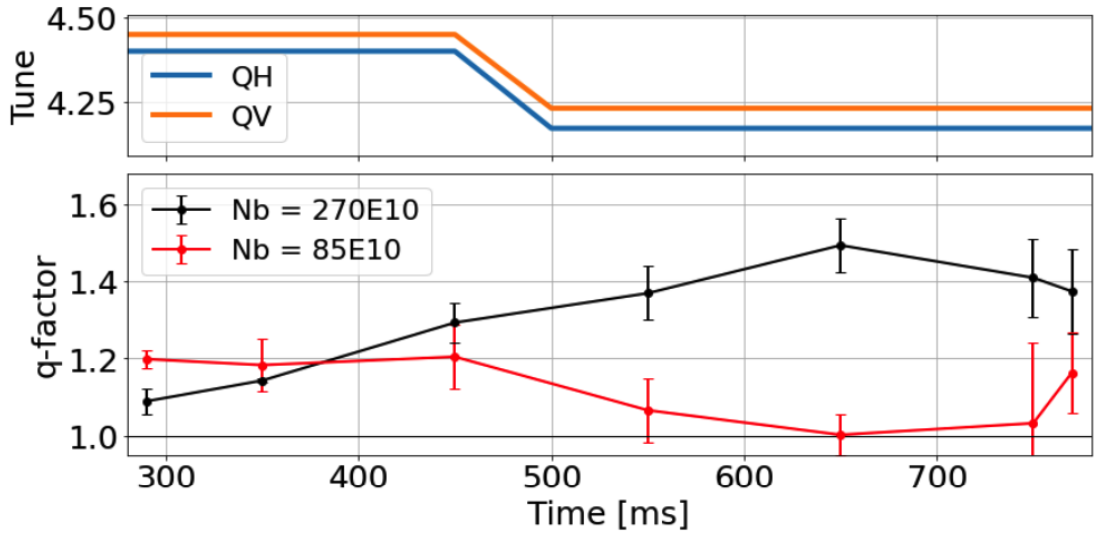

Figure 4.15: Tunes (top) and q-factor of the measured vertical profiles (bottom) along the PSB cycle for two different beam intensities ($N_b \approx 85 \times 10^{10}$ ppb and $N_b \approx 270 \times 10^{10}$ ppb). The profiles have been measured multiple times and their corresponding q-factors have been averaged. The WS effects have not been removed because at these intensities the emittance is dominated by the foil scattering blow-up (the effects are much weaker nevertheless at higher energies than the flat-bottom 160 MeV).

The result on the tails of all these mechanisms combined is shown in the bottom part of Fig. 4.15. The q-factor of the vertical profiles is plotted throughout the PSB cycle for two different beam intensities. For a relatively high intensity of the LHC-type beams ($N_b \approx 270 \cdot 10^{10}$ppb) the tails are enhanced throughout the cycle. The q-factor grows from 1.1 at injection, to almost 1.5 near extraction. For a lower intensity ($N_b \approx 85 \cdot 10^{10}$ppb), the tails remain almost unchanged. The q-factor is approximately

at 1.2 both at injection and extraction. The evolution of the vertical tails is not the same for the two intensities. This demonstrates how the interplay between space charge and resonances can have overall a quite different result on the population of the transverse profiles.

Different means for reducing the tail population and optimizing the beam accumulation of the operational LHC-type beams have been considered [53]. In order to minimize interaction with the 3$^{\text{rd}}$ and 4$^{\text{rth}}$ different tune evolution scenarios have been applied. For example, the working point was lowered from $(Q_x, Q_y) = (4.40, 4.45)$ to $(Q_x, Q_y) = (4.37, 4.28)$. This way the $3Q_x = 13$ resonance, that is excited in all rings (see Fig. 2.6), is avoided. The lowering of the working point comes with the cost of possibly inducing some emittance blow-up from the integer resonances, when trying to have high brightness beams. Furthermore, the rate at which the tunes dynamically change from the injection working point to the extraction working point has been made faster which also minimizes interaction with the resonances. The minimization of the resonance interaction has reduced the tail content with minor impact on emittances (some ring-per-ring variations) [53].

4.7 Horizontal Profiles

So far, only the vertical beam profiles have been treated. This is because the horizontal profiles appear without overpopulated tails (left graph of Figure 4.1). However, this does not exclude the presence of non-Gaussian tails because of the non-zero dispersion present in the PSB. Dispersion couples the transverse and longitudinal motion and results in an increase of the horizontal phase space that the beam occupies. The motion of particles in the horizontal plane is given by the sum of the betatronic and the dispersive motion:

$$x = \sqrt{\epsilon_x \beta_x} cos\left(\psi_x\right) + \frac{\delta p}{p} D_x \tag{4.4}$$

Assuming that the betatronic motion is independent of the dispersive motion (i.e. ϵ_x and $\delta p/p$ are independent random variables), the probability density function (p.d.f.) of the combined motion is the convolution of the p.d.f. of the two:

$$f_{total} = f_b * f_d \tag{4.5}$$

If both betatronic and dispersive distributions are Gaussians with mean and standard deviation (μ_b, σ_b) and (μ_d, σ_d) respectively, then the total distribution is also Gaussian:

$$f_b^G(\mu_b, \sigma_b) * f_d^G(\mu_d, \sigma_d) = f_{total}^G\left(\mu_b + \mu_d, \sqrt{\sigma_b^2 + \sigma_d^2}\right) \tag{4.6}$$

Therefore, the horizontal beam size is:

$$\sigma_x = \sqrt{\epsilon_x \beta_x + D_x^2 \left(\frac{\delta p}{p}\right)^2_{RMS}}, \tag{4.7}$$

In the majority of cases, this simple Gaussian subtraction is used for the emittance calculation in the horizontal plane. If either the betatronic or the dispersive distribution are not Gaussian, the total distribution will also not be Gaussian. To address the shape and the tail content of the horizontal profiles, one needs first to deconvolute the dispersive part.

In the PSB, in order to mitigate the space charge effects at injection, a double harmonic RF system is used to flatten the bunch profile and decrease the peak line density. Thus, the longitudinal (dispersive) distribution follows more a parabolic shape rather than a Gaussian. A parabolic dispersive profile will reduce the tails of the measured distribution [54]. Therefore, a Gaussian betatronic distribution would appear in the measuring instrument with underpopulated tails. Also, a betatronic distribution with overpopulated tails would appear with Gaussian tails in the measuring instrument. This was confirmed experimentally in the PSB. Figure 4.16 shows the q-factor of the horizontal profiles near extraction of the PSB ($t = 770$ ms) for a beam intensity of $N_b \approx 50 \times 10^{10}$ ppb as a function of the RMS momentum spread. For an RMS momentum spread of $\delta p/p \approx 1.4 \times 10^{-3}$ (nominal value of the LHC-type beams), the measured horizontal profiles appear with even slightly underpopulated tails ($q < 1$). As the momentum spread decreases, and the contribution of the parabolic dispersive distribution becomes less significant, the q-factor of the measured profiles grows (the tails become more populated). For example, a 25 % reduction in the RMS momentum spread increased the q-factor from 0.95 to 1.05. Although smaller reduction of the RMS momentum spread was not possible, the data have been linearly fitted and the fit has been extrapolated to RMS $\delta p/p = 0$ (no contribution from the dispersive distribution). In that case, the q-factor reaches values of ≈ 1.4 which is similar to what is observed in the vertical plane but this is just an estimation. The dependence of the horizontal shape in terms of q-factor might not be linear for smaller $\delta p/p$ values.

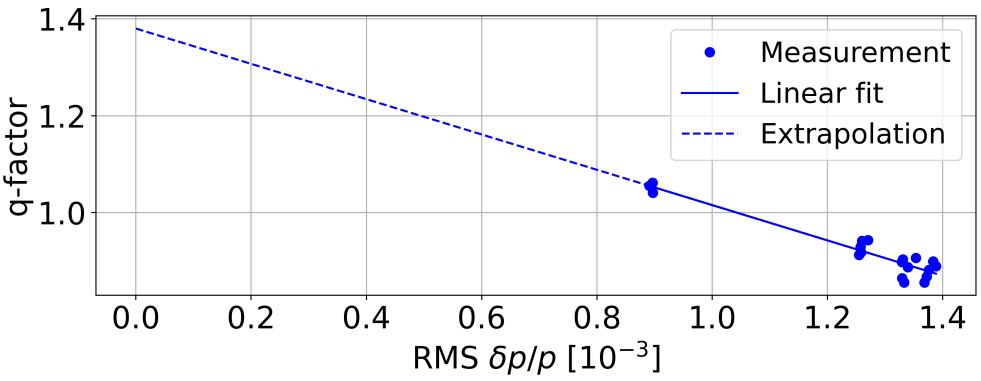

Figure 4.16: q-factor of the measured horizontal profiles at extraction ($t = 770$ ms) of the PSB for different values of the RMS momentum values (dispersive contribution). The blue solid line represents a linear fit of the measured data and the blue dashed line an extrapolation of the fit to zero momentum spread.

To get a more quantitative study on the horizontal tails in the PSB, a deconvolution algorithm is needed. Such algorithms have been used in past studies [54], but they always assumed that at least one of the three distributions (measured, betatronic and dispersive) is Gaussian. More generic algorithms need to be developed, but this is beyond the scope of this thesis.

Chapter 5

Characterization of the Half-Integer Resonance

5.1 Motivation

In Chapter 3 it was shown that operation at working points with higher tunes mitigates the emittance growth induced by the interaction of the beam with resonances in the presence of space charge detuning, notably close to the integer tunes. This contributed to an improved beam brightness. Ideally, injection at even higher vertical tunes, above the half-integer resonance $2Q_y = 9$, could mitigate the emittance growth from the space charge effects even more. However, in this scenario, to reach the extraction working point $(Q_x, Q_y) = (4.17, 4.23)$, the half-integer resonance needs to be dynamically crossed during the acceleration cycle. The dynamic crossing of resonances is a common practice in the PSB operation for the higher order and relatively weak third and fourth order resonances. The half-integer resonance is much stronger and more difficult to control. Thus crossing it can lead to particle losses and/or emittance growth and reduce the beam brightness.

In this context, a series of studies were initiated in order to characterize the effects of space charge when crossing the half-integer resonance. These effects can considerably change with respect to the resonance strength, the crossing speed, the space charge tune spread, the chromaticity and many more factors. The eventual goal was to experimentally study and understand the beam behaviour in these conditions and to find the optimal configuration to increase the delivered brightness.

After the LIU upgrades, the PSB is very well suited for performing these kind of studies. The multi-turn H^- injection scheme allows producing a large variety of transverse emittances and beam intensities, which enables the control of the space charge tune footprint. In addition, the recently implemented tune control system [55] allows machine operation in a wide range of working points below and above the half-integer resonance and also the dynamic change of tunes along the acceleration cycle with good precision. Finally, the identification and compensation of resonances up to fourth order has been extensively studied in the PSB [22]. As a result, the half-integer resonance can

be compensated to a good extent, but can also be excited in a controlled manner by deliberately degrading the resonance compensation scheme.

In this Chapter, the experimental results of the half-integer resonance crossing in the presence of weak and strong space charge are reported. All experimental results are compared to space charge tracking simulations using the PSB simulation models described in section 2.7.

5.2 Vertical Half-Integer Resonance $2Q_y = 9$

5.2.1 Correction and excitation

The control of the vertical half-integer resonance is the first and most important step of these studies [56]. The PSB is equipped with a set of multipole corrector magnets (quadrupoles, sextupoles and octupoles) that are used for the compensation of the naturally excited resonances. The vertical half-integer resonance $2Q_y = 9$ is compensated by two families of normal quadrupole correctors, as illustrated in Fig. 5.1. The first family consists of quadrupoles in the fourth and in the twelfth period of the machine (QNO412) and the second family of quadrupoles in the eighth and sixteenth period (QNO816). The half-integer resonance driving term (see Appendix A.3) generated by the QNO412 family is orthogonal with respect to the driving term of the QNO816 family. The quadrupole pairs within the families have opposite current polarities so that they do not change the overall tune of the machine but constructively excite the corresponding half integer resonance driving term.

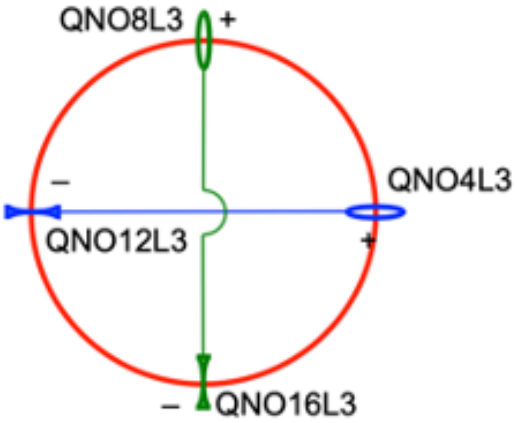

Figure 5.1: An illustration of the two orthogonal families of quadrupole correctors used for the compensation of the half-integer resonance. The first family consists of quadrupoles QNO4L3, QNO12L3 (referred as QNO412 family) and the second family consists of QNO8L3 and QNO16L3 (referred as QNO816). The signs represent the corresponding polarities of the quadrupoles.

The optimal strength of the quadrupoles that cancels the driving term of the naturally

excited half-integer resonance is determined experimentally. The orthogonality of the orientation of the correctors' driving terms ensures that a driving term with any phase and amplitude can be constructed, within the magnet current limitations. By varying the currents of the two families, a configuration can be found at which the beam losses while crossing the resonance are minimized. At this configuration, the driving term created by the quadrupole families cancels the driving term of the naturally excited half-integer resonance. Residual beam losses of the order of 2 % are present even in the optimal configuration of strengths. The reasons for this are not fully understood. The compensation of the half-integer resonance and all the following studies have been performed at the flat-bottom energy of the PSB (160 MeV).

To reveal the physical processes that the beam undergoes during the resonance crossing, the half-integer resonance has been first compensated and then deliberately excited. The excitation is done by slightly changing the strengths of QNO412 and QNO816 with respect to their optimal compensating value. This way, the resonance has a finite width that is strong enough to have a measurable effect on the beam, but not too strong (like the naturally excited resonance) so that the beam is lost completely and it cannot be studied. If not explicitly mentioned otherwise, it will be assumed that the half-integer resonance is always excited by changing the current of the QNO816 family by $\delta I_{816} = -2A$ from its compensation value. This corresponds to an integrated focusing strength of $\delta(k_1 l_{816}) = -6.2 \times 10^{-4}$ m^{-1}.

5.2.2 Resonance width measurement

The particle motion can be unstable not only exactly at the resonance condition, but also for tunes with a finite distance around a resonance. The width of this area is known as the resonance stopband width. Inside the half-integer stopband the particle motion is unstable: the amplitude of the betatron oscillations grows exponentially and losses occur. The stronger is the resonance excited the larger is the growth rate. Outside but near the half-integer stopband, the motion is stable but the growth in amplitude of the betatron oscillations (β-beating) can drive particles to large amplitudes and thus, due to the limited machine aperture, lead to losses. The β-beating grows exponentially while the tune approaches the half-integer resonance (Fig. 3.3). Furthermore, the space charge detuning can further extend the tune region in which losses are observed.

For the characterization of the stopband width, the half-integer resonance was excited by $\delta I_{816} = -2$ A. In order to minimize the effects coming from the space charge detuning and the β-beating, a coasting beam with low intensity and small transverse emittances was used, shown in Fig. 5.2. The RMS-momentum spread was measured at $(\delta p/p)_{\mathrm{RMS}} \approx 10^{-3}$ and the maximum space charge detuning was analytically estimated to be $\delta Q_y^{SC} \approx -3 \cdot 10^{-3}$ ('Type A' of Table 5.1).

The stopband width δQ_w of the half-integer resonance $2Q_y = 9$ was measured by dynamically crossing the resonance from above ($Q_y > 4.5 \rightarrow Q_y < 4.5$) and from below ($Q_y < 4.5 \rightarrow Q_y > 4.5$) with different crossing speeds while monitoring the beam intensity. Figure 5.3 shows the measured vertical tunes (top) and the normalized beam

Type	N_b [10^{10} ppb]	ϵ_x/ϵ_y [μm]	$\delta p/p$ [10^{-3}]	$\delta Q_x^{SC}/\delta Q_y^{SC}$ [-10^{-3}]	Longitudinal
A	2.5	1.0/0.7	≈ 1.0	$\approx 2.0/3.0$	Coasting
B	4.0	2.9/10.0	1.0	$\approx 1.2/0.6$	Coasting
C	40	1.0/0.7	1.36	$\approx 40/50$	Coasting

Table 5.1: Some of the different beam types used in the half-integer experiments.

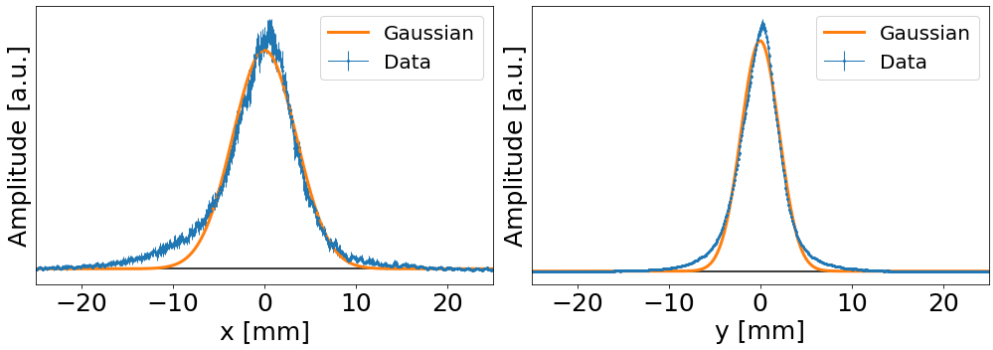

Figure 5.2: Horizontal (left) and vertical (right) beam profile used in the half-integer stopband width measurements. The profiles are measured with a wire scanner. The asymmetric tails in the measurement are associated with the scattering of the beam due to the crossing wire (see section 4.3). The estimation of the space charge detuning has been computed analytically assuming Gaussian distributions (orange). A small error is induced by the non-Gaussian tails.

intensity (bottom) evolution during the crossing of the resonance from both directions. The different colors correspond to the three different crossing speeds. The tune is measured using the BBQ system and the intensity using the BCT. To reduce statistical uncertainties, the intensity was measured for multiple cycles for each of the different crossings. The solid lines represent the mean intensities while the shaded areas the standard deviation (1σ).

When the beam is near the resonance, losses are recorded. The losses range between 80-100 % when crossing from above and 20-60 % when crossing from below. While the average losses are lower when crossing from below, the uncertainty of the intensity after crossing the resonance is much larger, especially for the lower crossing speeds. This observation is discussed in more detail in section 5.8. Fewer particles are lost for faster crossing speeds, as expected.

The beam intensity for the different crossing scenarios is plotted in Fig. 5.4 as a function of the vertical tune. It can be observed that when crossing from below, the beam loss stops at approximately $Q_y = 4.5005$, independently of the crossing speed. Similarly, when crossing from above, the beam loss stops at approximately $Q_y = 4.4965$. At these tune values the beam intensity is stable and thus they define an upper limit of the stopband boundaries. Therefore, for this particular excitation, the stopband width

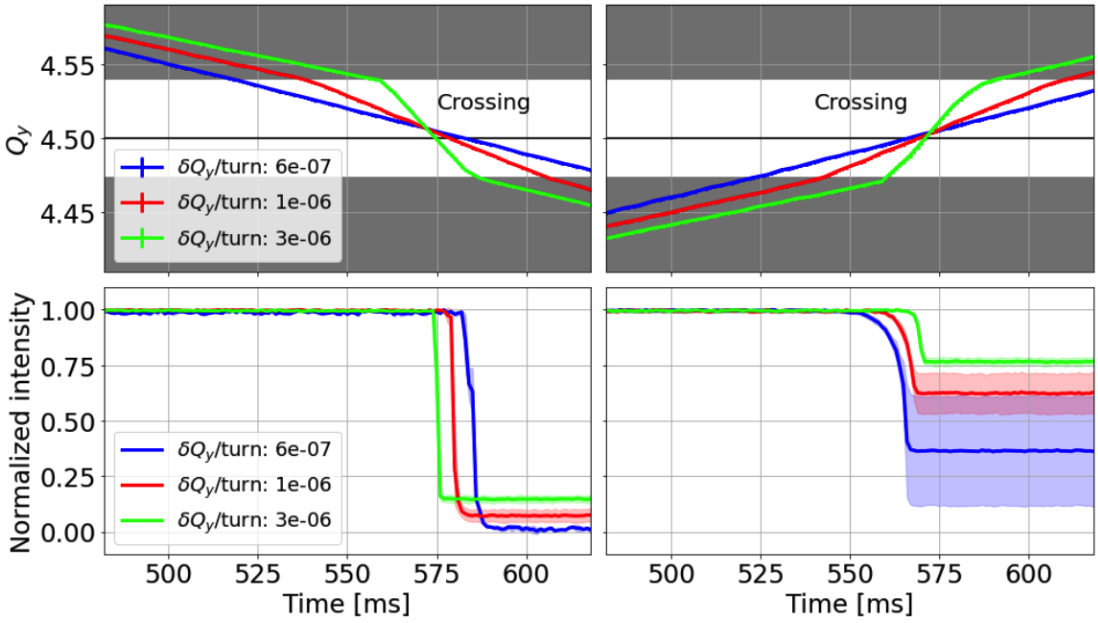

Figure 5.3: Evolution of beam losses when crossing the half-integer resonance with three different crossing speeds (different colors) from both directions (from below and above). A coasting beam with a very slow space charge is used.

should be at most $\delta Q_w \approx 4.5005 - 4.4965 = 0.0040$. Depending on the crossing speed, the beam spends a few thousands of turns inside the stopband.

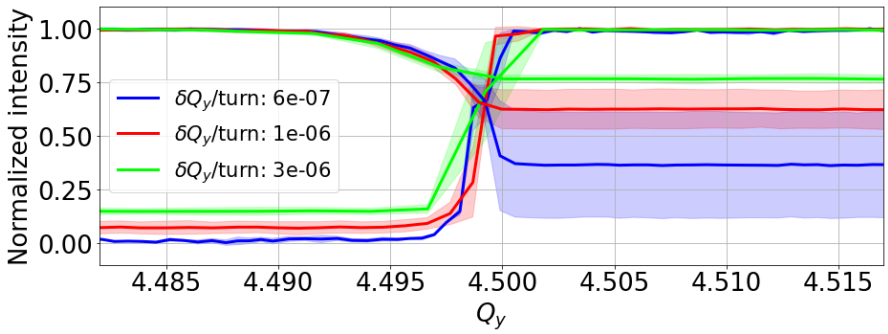

Figure 5.4: Half-integer stopband width measurement for $\delta I_{816} = -2$ A.

It is worth mentioning that attempts to cross even faster or even slower were made. While it is possible to apply dynamical tune changes that are faster, the intensity acquired by the BCT is limited to every 1 ms interval, in which the vertical tune changes considerably. This results to a loss in resolution of the vertical tune, making it impracticable to distinguish the upper limits of the stopband boundaries. Nevertheless, the losses are again much lower for faster crossing speeds. For dynamical tune changes that

are slower, the beam is fully lost and the same analysis cannot be performed.

Analytical estimations of the half-integer stopband can be found in literature [19, 6]:

$$\delta Q_w^{\mathrm{an}} = \frac{1}{2\pi}\left|\oint \beta(s)p(s)e^{-i(2n+1)\phi(s)}ds\right|, \tag{5.1}$$

where p is the perturbation strength, β the beta-function at the location of the perturbation, n the integer part of the tune and ϕ the phase advance over the betatronic tune. Considering that the half-integer resonance is perfectly compensated and the only excitation driving term comes from the $\delta I_{816} = -2$ A of the QNO816 family, this formula gives a value of $\delta Q_w^{\mathrm{an}} \approx 0.0012$. This width is well within the upper boundaries that were defined experimentally. Note that the experimentally determined stopband width is expected to be larger than the analytical prediction, due to residual resonance excitation not taken into account in the calculation as well as the detuning from space charge.

5.2.3 Applying stronger excitations

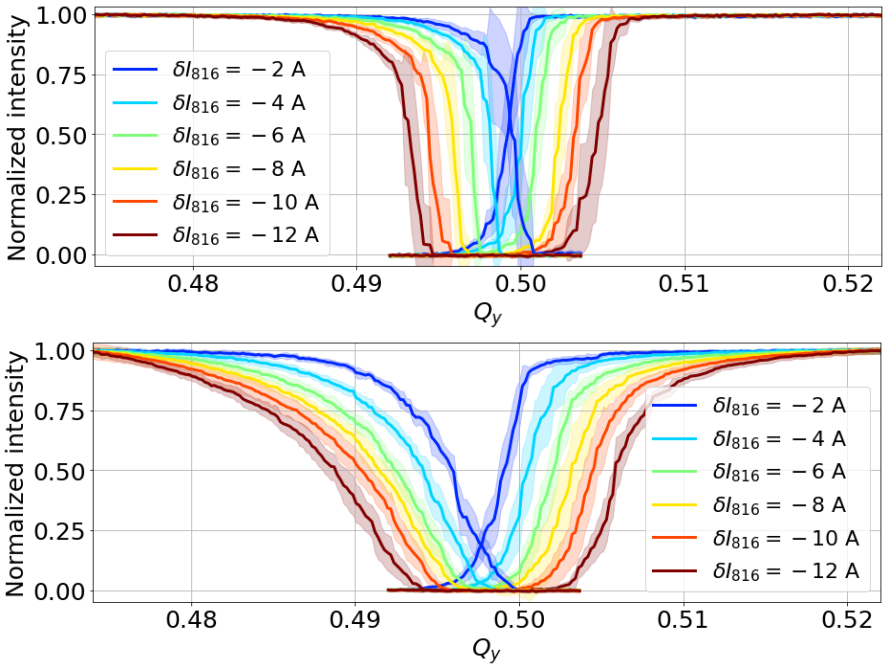

Figure 5.5: Beam intensity as a function of the vertical tune for different amplitudes of the half-integer excitation. In the top plot the beam of Fig. 5.2 was used, while in the bottom plot the beam of Fig. 5.6.

An effort was made to measure the half-integer stopband width for different excitation amplitudes using the same method as above. The resonance was again crossed from both

directions and the beam intensity was monitored. The results are summarized in Fig. 5.5. The different colors correspond to different excitation amplitudes of the resonance while in all cases the crossing speed was the same.

At the top plot of Fig. 5.5, the beam of Fig. 5.2 was used (low intensity and small transverse emittances). The points in which the losses stop while crossing the resonance, that previously represented the boundaries of the stopband, cannot be determined here since the beam is fully lost for all of the stronger excitations. Thus, it is not possible to assess the stopband boundaries like this.

Instead of searching for the tune in which the beam exits the stopband and the loss stops, one could try and specify the tune in which the beam enters the stopband and the losses start. What complicates the situation in this case is that the losses, instead of abruptly starting at some tune (the tune in which the beam enters the stopband), increase gradually over a range of tunes. This behaviour is more evident when approaching the half-integer resonance from below ($Q_y < 4.5$) and could be associated with the β-beating that can cause slow losses.

The last argument can be further supported by the bottom plot of Fig. 5.5. Here, the same experiment as before was performed but with a beam that has low intensity and much larger vertical emittance ('Type B' of Table 5.1). This beam, which is shown in Fig. 5.6, was deliberately blown-up by applying an injection mis-steering and enabling octupoles to induce filamentation in the transverse plane. The vertical particle distribution almost fills the acceptance of the PSB, making the sensitivity of the losses to the β-beating much higher.

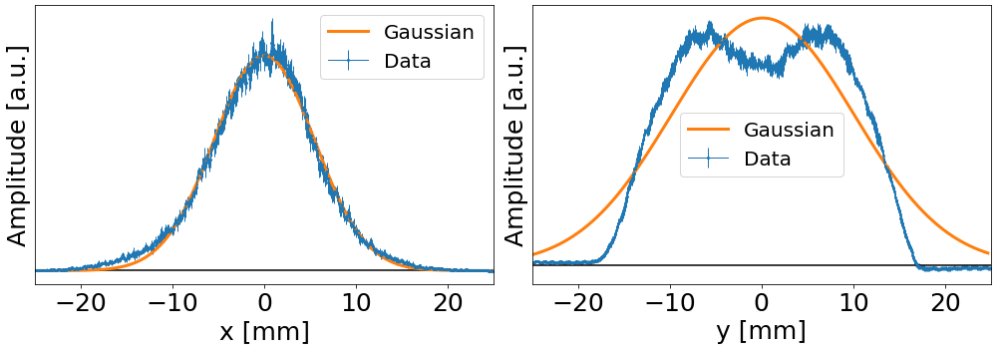

Figure 5.6: Horizontal (left) and vertical (right) beam profile that have been deliberately grown to fill the acceptance.

The losses during the crossing that are shown in the bottom plot of Fig. 5.5 start much earlier than the top plot of the same figure, despite the fact that the stopband size should be the same, and are even more gradual. This can be attributed to the beta-beating as even a weak perturbation in the optics can induce measurable losses due to the large beam size.

Although the stopband width cannot be strictly determined for stronger excitations, one can define the resonance width at which the losses increase above a specified thresh-

old as a function of the excitation strength. This was only done for the low intensity and small transverse emittances (Fig. 5.2) to minimize the contribution of the beam loss from β-beating. Figure 5.7 shows the tunes at which the 5 % loss level is reached for the different excitation strengths. The analytical estimation of the stopband width, using Eq. 5.1, is plotted with green and is always within the boundaries at 5 % losses. The dependence of the stopband width to the excitation strength is almost linear as it is expected from the analytical formula. Further simulation studies are needed in order to relate the observed differences.

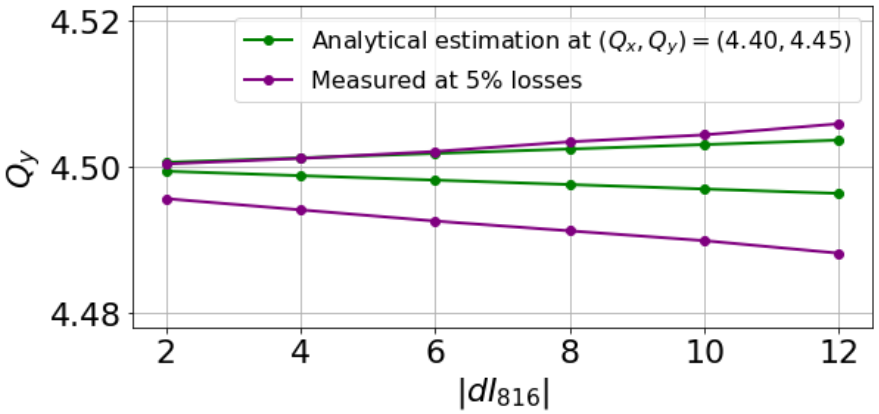

Figure 5.7: Tunes at which 5 % losses are observed in the top plot of Fig. 5.5 as a function of the current shift of the QNO816 family (purple). Comparison to analytical estimations of the stopband width (green).

5.3 Adiabatic Crossing of a Coasting Beam

The vertical half-integer resonance $2Q_y = 9$ was dynamically crossed from above with different beam parameters and different crossing speeds. The studies that will follow were concentrated on crossing the half-integer from above, due to the possible operational interest of the PSB. A crossing of the half-integer from below is briefly discussed in section 5.8. Furthermore, most of the half-integer crossing experiments were performed at the PSB injection energy of 160 MeV. Beams with different transverse emittances and beam intensities were used for the experiments. The number and the length of the pulses that are injected from L4 can be easily adjusted to produce intensities that range from one to a few hundreds 10^{10} protons per bunch (ppb). Furthermore, by controlling the number of turns the circulating bunch goes through the injection foil and also the injection missteering, the transverse emittances can vary from 0.5 to 10 mm·mrad.

The cases of bunched or unbunched (coasting) beams are studied separately as well as the cases with natural and compensated vertical chromaticity. In this section, the crossing of a coasting beam with compensated vertical chromaticity will be discussed. The coasting beam has the advantage that no synchrotron oscillations occur. In this case,

there is no periodic resonance crossing, as described in Section 2.5. The coasting beam was produced by injecting a long pulse from L4, that almost fills the PSB circumference, and then by keeping all the RF cavities switched off. The pulse fully debunches after only 500 turns which corresponds to approximately 0.5 ms after injection.

The dynamic crossing of the half-integer resonance was also reproduced in simulations. The PTC-PyOrbit code was used for tracking particles for thousands of turns in the model PSB lattice of MAD-X and at the energy of 160 MeV. The model machine aperture was included in the simulations. The dynamic crossing of the half-integer resonance was programmed by ramping the strengths of the focusing and defocusing quadrupoles in PTC as a function of the number of turns. 6-D particle distributions were generated using 200 thousand macroparticles with transverse and longitudinal parameters very similar to the measurements (emittances, intensity, bunched/coasting, momentum spread, chromaticity). A 2.5D self-consistent PIC algorithm was used as a space charge solver [43]. The observation point for all the phase space plots of the simulation was the location of the vertical Wire Scanner at which the measurements were performed.

5.3.1 Particle trapping

The stability of the particle motion near a resonance depends on the distance of the working point from the resonance and also the amplitude detuning. Here, the detuning of the particles comes mainly from the space charge defocusing, which is amplitude dependent and results in a tune spread. The tune spread induced by chromaticity is negligible here since the vertical chromaticity is compensated.

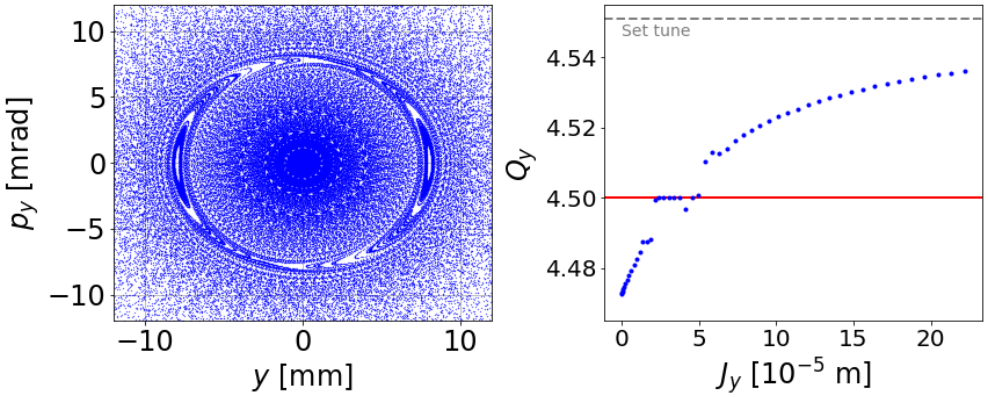

Figure 5.8: Left: simulation of the resonance pattern of the phase space in the vicinity of the half-integer resonance. Right: amplitude detuning from the space charge defocusing. The set working point is denoted with the grey dashed line and the excited half-integer resonance with the red solid line.

The presence of tune spread can create resonance patterns in the trajectory of the

particles in the phase space. An illustration of such a pattern is given in Fig. 5.8. On the left graph the vertical phase space is shown and on the right graph the vertical tune as a function of the particle phase space amplitude (i.e. action J_y). The set tune is shown with the grey line at $Q_y = 4.55$ and the excited half-integer resonance with the red line at $Q_y = 4.5$. Particles with small amplitude get a larger detuning than particles with larger amplitude. The phase space is structured by a central stable part that is surrounded by the two resonance islands. The boundary between the central part and the resonance islands is called separatrix. The number of the islands depends on the order of the resonance (here second order) and their size on the resonance strength and detuning gradient [25]. The amplitude at which the islands appear depends on the amplitude of the particles that fall into the resonance stopband due to the amplitude detuning. In this example, particles between $0.3 \times 10^{-5} < J_y < 0.6 \times 10^{-5}$ meters are locked into the half-integer resonance, particles with $J_y < 0.3 \times 10^{-5}$ meters fall below the resonance and particles with $J_y > 0.6 \times 10^{-5}$ meters fall above the resonance. In the dynamic crossing of the resonance from above with a coasting beam, the resonance islands will appear in the center of the phase space and will dynamically move towards larger amplitudes.

A dynamic resonance crossing was performed experimentally in the PSB. The half-integer resonance was deliberately excited by $\delta I_{816} = -2$ A which gives a stopband width of less than $\delta Q_w \approx 0.0040$, as discussed Section 5.2.2. The resonance was dynamically crossed from above ($Q_y > 4.5$) by changing the vertical tune and keeping the horizontal tune constant ($Q_x = 4.15$). Figure 5.9 shows the measured vertical tune as a function of time. The tune is measured every 4 ms using the BBQ system. The crossing is relatively slow (adiabatic crossing [26]). At the injection energy of the PSB, one millisecond corresponds to approximately 1000 revolutions around the ring. Here, the tune change per turn (crossing speed) is approximately $\delta Q_y/\text{turn} = 0.65 \times 10^{-6}$. The vertical chromaticity has been experimentally minimized using the available sextupole correctors.

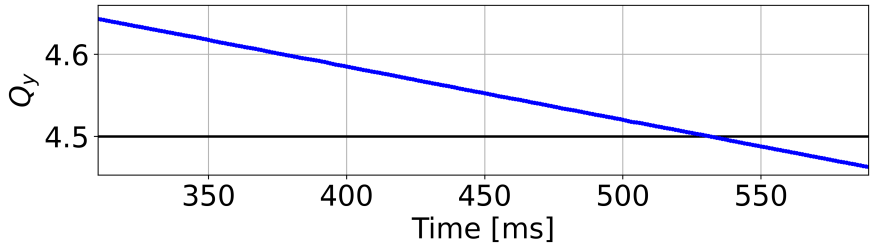

Figure 5.9: Measured vertical tune during the dynamic crossing of the half-integer.

A coasting beam of an intensity $N_b \approx 40 \times 10^{10}$ ppb, $\epsilon_x \approx 1$ μm and $\epsilon_y \approx 0.7$ μm was used ('Type C' of Table 5.1). The space charge tune spread was estimated to be $\delta Q_y^{SC} \approx -50 \times 10^{-3}$ which is more than 12 times larger than the width of the stopband (in absolute value). The beam was fully lost after the crossing of the half-integer resonance. The vertical beam profile was measured with the WS at $t = 515$ ms, before losing the

beam. The measured profile is shown in Fig. 5.10. It is observed that approximately 10 % of the total particles populate two regions outside the main beam core. These two beamlets correspond to the particles that have been trapped in the resonance islands of the half-integer resonance during the adiabatic crossing of the resonance.

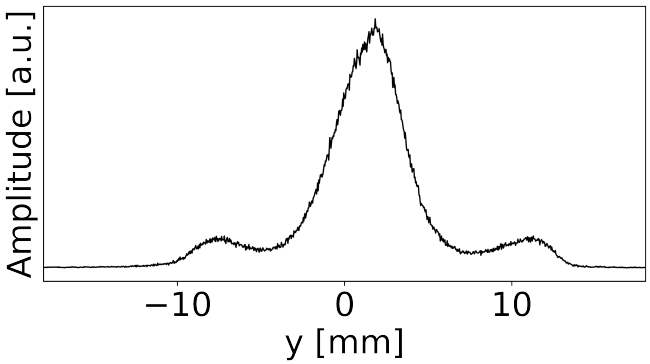

Figure 5.10: Vertical beam profile measurement with trapped particles in the half-integer resonance islands.

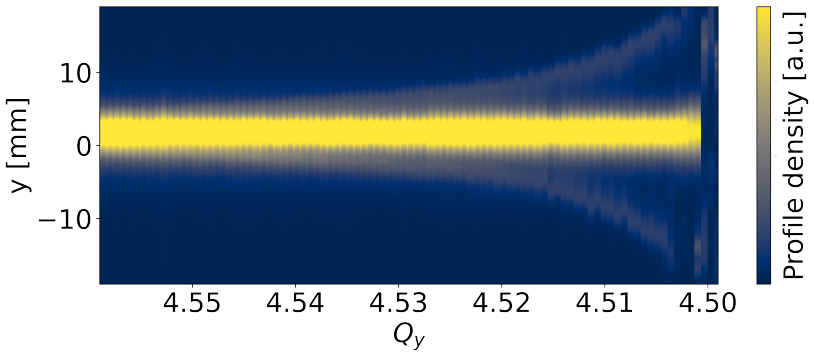

Figure 5.11: Evolution of the vertical beam profile as a function of the tune when dynamically crossing the resonance. The profiles have been measured with a WS.

The vertical beam profiles were measured multiple times during the half-integer resonance crossing. These profiles are plotted in Fig. 5.11. Here, the horizontal axis corresponds to the measured tune, the vertical axis to the y-position and the color to the density of the measured profiles, which are measured with the WS every millisecond. It is reminded that the WS takes more than 3000 turns to perform the scan (see section 4.3). For $Q_y > 4.55$ ms, the beam is far from the resonance and the profiles follow a near Gaussian distribution. While the beam moves closer to the half-integer resonance, particles from the beam core, that have the stronger detuning, are trapped in the resonance islands. As the tune ramp continues ($Q_y < 4.53$), the resonance islands move adiabatically to larger amplitudes, along with the particles that have been trapped

(two beamlets). The space charge forces gradually become weaker and the tune shift decreases. While the beam continues to approach the half-integer resonance, the islands continue to move outwards until particles hit the machine aperture and are lost ($Q_y \approx 4.503$ ms). Just over one or two milliseconds after, the beam core is lost as well. The reasons why this loss of the beam core particles occurs are discussed extensively in the next section.

The measurement of the profile evolution has not been performed during one cycle of the PSB. Instead, each profile measurement comes from a different PSB cycle with the same beam and machine configurations (similar beam intensities, emittances, crossing speed, chromaticity correction). Thus, the plots of Fig. 5.11 are composed by combining the profile measurements from all the different PSB cycles. Although the reproducibility of the PSB is excellent, there are always some fluctuations in the injection efficiency and the beam intensity, which result to the 'jittering' seen in the islands of Fig. 5.11.

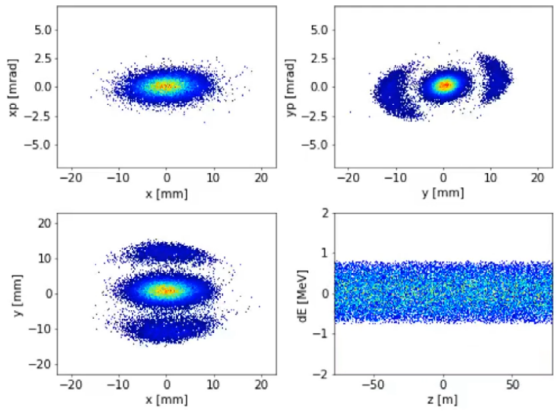

Figure 5.12: Half-integer trapping in simulations. Top left: horizontal phase space. Top right: vertical phase space (the trapped particles in the resonance islands are visible around the beam core). Bottom left: real space. Bottom right: longitudinal phase space (coasting beam). The color corresponds to the particle density.

The particle trapping during the adiabatic crossing of the half-integer from above has been reproduced in simulations. A distribution with similar beam parameters as of the measurement, but with slightly smaller space charge, was tracked for approximately 100 thousand turns and the vertical tune was ramped from $Q_y = 4.65$ to $Q_y = 4.45$. Figure 5.12 shows the phase space of the tracked particles at a fixed distance from the resonance. The horizontal and vertical phase spaces are plotted on the top left and right, respectively, the real x-y space on the bottom left and the longitudinal phase space on the bottom right. The two resonance islands (beamlets) along with their trapped particles are visible in the vertical phase space.

In Fig. 5.13, the profile evolution from the simulation is plotted, similarly to Fig. 5.11. To mimic the time that the WS takes to perform the profile measurements, here the tracked particles are not plotted turn-after-turn but they are averaged over a few thousands of turns. As in the measurements, the resonance islands move outwards in a very

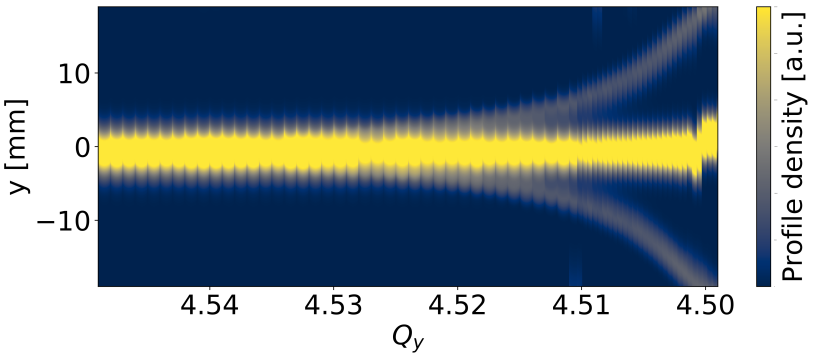

Figure 5.13: Simulation of the evolution of the beam profile as a function of the tune when dynamically crossing the resonance.

similar way. Hoever, in contrast to the measurement, here the beam core survives. Nevertheless, after the islands are lost, the beam core starts to oscillate in the vertical plane around $y = 0$. A possible explanation for this is the way the particles in the islands are scraped on the machine aperture. Small asymmetries in the way particles are lost can create an asymmetric potential between the island beamlets and the beam core.

In the previous simulation example, the space charge is slightly weaker compared to the measurements. The simulation was repeated with a stronger space charge and the result is highlighted in Fig. 5.14. On the left hand side, the phase space and real space are shown for tracked particles at a fixed distance from the half-integer. In contrary to Fig. 5.12, the population between the two beamlets in the vertical phase space is significantly different. Approximately 20 % of the total particles populate one of the islands and only 1 % the other. While the half-integer is crossed and the islands move towards larger amplitudes, the beam core also starts to deviate from the center $y = 0$. The asymmetry in the population forces the beam core to move outwards. On the right hand side, the vertical profile evolution from the same simulation is plotted. As before, the profiles are averaged over a few thousands of turns. Since the vertical tune is close to 0.5, the vertical phase space rotates and, at the same s-position, it appears as it is reflected (oscillates) turn-by-turn with respect to $y = 0$. The two beamlets that appear in the profile evolution graph are essentially result of the profile averaging and the turn-by-turn reflection of the heavy populated island. The deviation of the beam core from the center appears at approximately $Q_y = 4.505$ as a "splitting". In reality, the beam core does not split but oscillates around $y = 0$. The "splitting" is an effect of the WS profile reconstruction (here mimicked with the profile averaging). In this simulation case with stronger space charge, the full beam is eventually lost, as in the measurements.

The WS profile reconstruction not only was mimicked in the simulations with the profile averaging but also modelling by like a flying wire with realistic width, speed and impact on the beam (as described in Section 4.3.1). The top graph of Fig. 5.15 shows a simulation of the vertical profile measurement with a WS, when the half-integer is crossed with a strong space charge beam. The horizontal bottom axis corresponds to

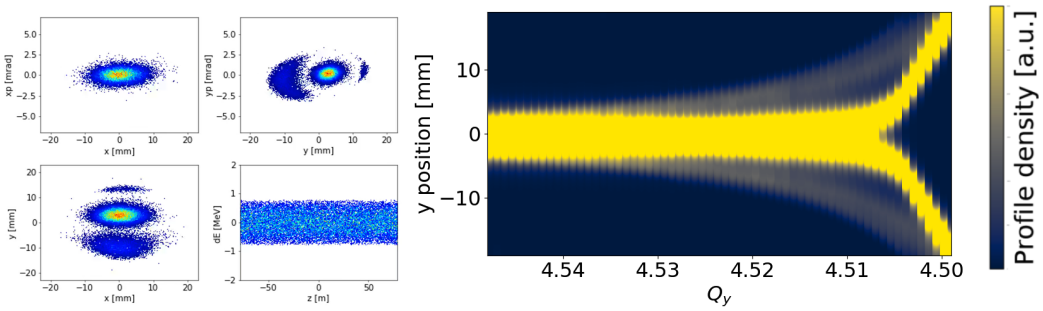

Figure 5.14: Simulation of the half-integer crossing with stronger space charge. Left: phase sapce and real phase space of the tracked particles at a fixed distance from the resonance. In the vertical phase space (top right subplots) the asymmetric population in the islands is shown. Right: profile evolution in simulation.

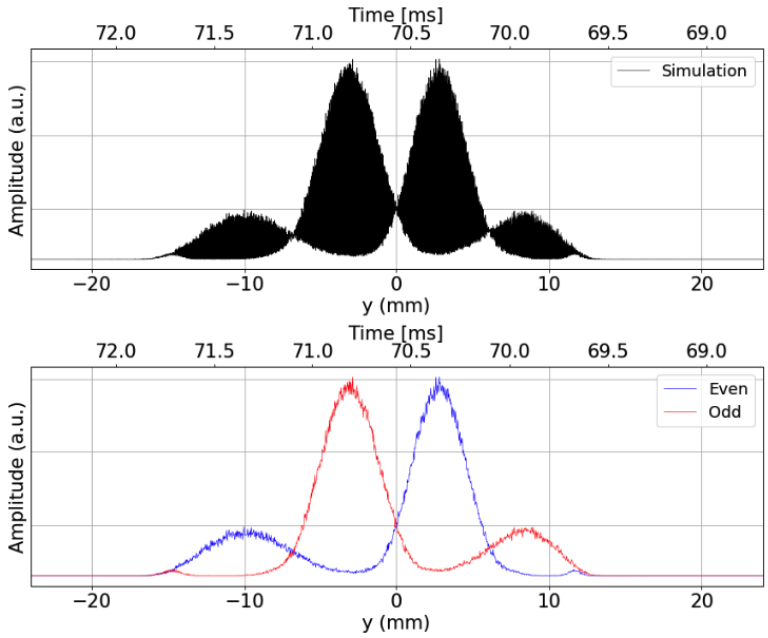

Figure 5.15: Top: simulation of a WS measurement of the vertical beam profile when crossing the half-integer with strong space charge at which the asymmetric population of the islands appears. The horizontal bottom axis corresponds to the wire position, the horizontal top axis the time of the scan (the wire speed is known) and the vertical axis the wire scanner signal. Bottom: the same measurement but plotting odd and even turns with different colors.

the wire position and the horizontal top axis the time that passes while the wire scans the beam (the wire speed is known). The vertical axis is the WS signal amplitude, which is proportional to the number of particles the wire intercepts at each turn. The

scan is performed from right to left approximately between the times 69 and 72 ms of the simulated beam storage. The beam core "splitting" can be seen between 70.2 and 71.2 ms. As explained before, this corresponds to an oscillation of the beam core with respect to the $y = 0$ with a frequency (tune) of 0.5. Indeed, by plotting the WS signal amplitude points with different colors turn-by-turn (blue for even turns and red for odd turns), as shown in the bottom graph of Fig. 5.18, the signal is deconvoluted. In the blue curve, the beam core is seen between $y = -2$ and $y = 8$ mm, the heavily populated beamlet between $y = -15$ and $y = -5$ mm and the lightly populated island is barely visible between $y = 11$ and $y = 12$ mm. After one turn, due to the phase space rotation at the tune of about 0.5, this topology is reflected to the red curve.

5.3.2 Beam effects for strong space charge

In the previous section, experimental observations of the particle trapping during the half-integer resonance crossing were shown. For relatively weak space charge, the tracking simulations were reproducing very well the measurements. For stronger space charge the beam was fully lost after the crossing, both in measurements as well in simulations. The mechanism that leads to these observations is not very well understood.

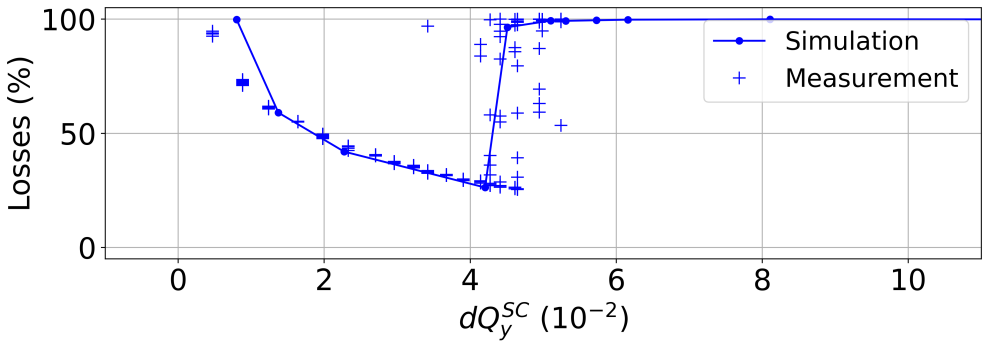

Figure 5.16: Beam losses as a function of the estimated space charge detuning (in absolute value) when adiabatically crossing the half-integer resonance. The blue crosses represent the experimental data points and the blue circles connected with solid lines the results from simulations.

To get insights on the beam dynamics in these special conditions, the beam intensity was monitored when slowly crossing the half-integer resonance using a coasting beam. This was done both experimentally and in simulations using a coasting beam with constant emittances and momentum spread, but different intensities (and therefore different space charge detuning). Figure 5.16 shows the beam losses after the crossing as a function of the space charge detuning in absolute value (denoted as dQ_y^{SC}). The blue crosses represent experimental data points and the blue circles (connected with solid lines) the results from simulations. The agreement between the two is excellent.

For weak space charge ($dQ_y^{SC} < 0.01$), the full beam is lost because the space charge detuning is not large enough to stabilize the particle motion and most of the particles end up in the unstable region of the resonance. When the detuning from space charge increases ($0.01 < dQ_y^{SC} < 0.04$), stable resonance islands appear in the phase space that trap particles. In this case, the losses are associated with the scraping of islands that have moved outwards and hit the machine aperture. As the gradient of the space charge detuning increases, less particles are trapped and fewer losses are observed. Beyond a certain space charge detuning ($dQ_y^{SC} > 0.04$) the beam is again fully lost. This region will be referred to as the 'strong space charge regime'.

The asymmetry of the particle population of the two resonance islands shown already in Fig. 5.14 seems to be the reason for destabilizing the beam core and thus losing the particles in the simulations. Figure 5.17 shows a simulation of the vertical phase space at a fixed tune distance from the resonance, for four different space charge detuning settings. On the top left graph the case of very weak space charge is shown. Here, because the detuning is small, no stable region appears in the center of the phase space and thus all particles are lost. The top right and bottom left graphs show two cases in which the trapping occurs (similar to Fig. 5.12). Finally, the bottom right graph shows a typical phase space portrait of the strong space charge region. The population of the two islands is very asymmetric. Here, the beam is fully lost within only a few thousands of turns (one or two milliseconds).

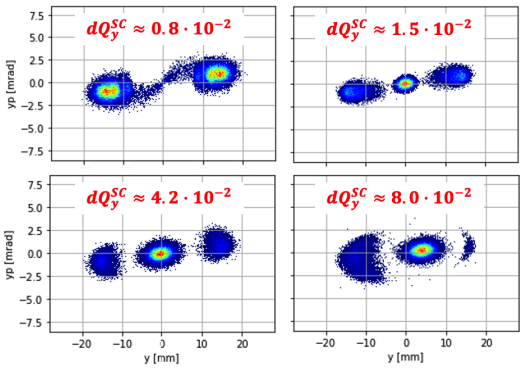

Figure 5.17: Vertical phase space for different strengths of space charge.

The reason why in the simulations the trapping of particles in the islands becomes asymmetric above a certain space charge threshold is not fully understood. Nevertheless, in order to get experimental evidence of the beam behaviour in this strong space charge region, multiple WS profile measurements were performed only a few milliseconds before losing the beam. What makes the measurement complicated is the time that the wire scan takes to be performed, as already described in the previous section. This time is not negligible for fast dynamic effects, such as the ones observed in simulations at which the beam is lost within a few milliseconds. Nevertheless, useful information can be extracted by carefully treating the WS data.

The top graph of Fig. 5.18 shows a vertical profile measurement with the WS when the

half-integer is crossed with an estimated space charge detuning of $\delta Q_y^{SC} \approx -50 \times 10^{-3}$ ('strong space charge regime'). The profile was measured before the beam was lost. Similarly to Fig. 5.15, the horizontal bottom axis corresponds to the wire position and the horizontal top axis the actual time that passes while the wire scans the beam (the wire speed is known). The vertical axis is the WS signal in arbitrary units. The scan is performed from right to left and approximately between the cycle times 630 and 633 ms. Between 630.5 and 632 ms, two peaks are clearly observed. This part is almost identical with what was simulated in Fig. 5.15. By plotting with different color the odd and even turns (bottom graph of Fig. 5.18), as in simulations, the WS signal is deconvoluted because of the fractional tune of 0.5 and the beam core oscillations, here with respect to the closed orbit at $y = 3$ mm, are evident. This is an experimental observation of an oscillatory process that is very similar to the one observed in simulations. On the other

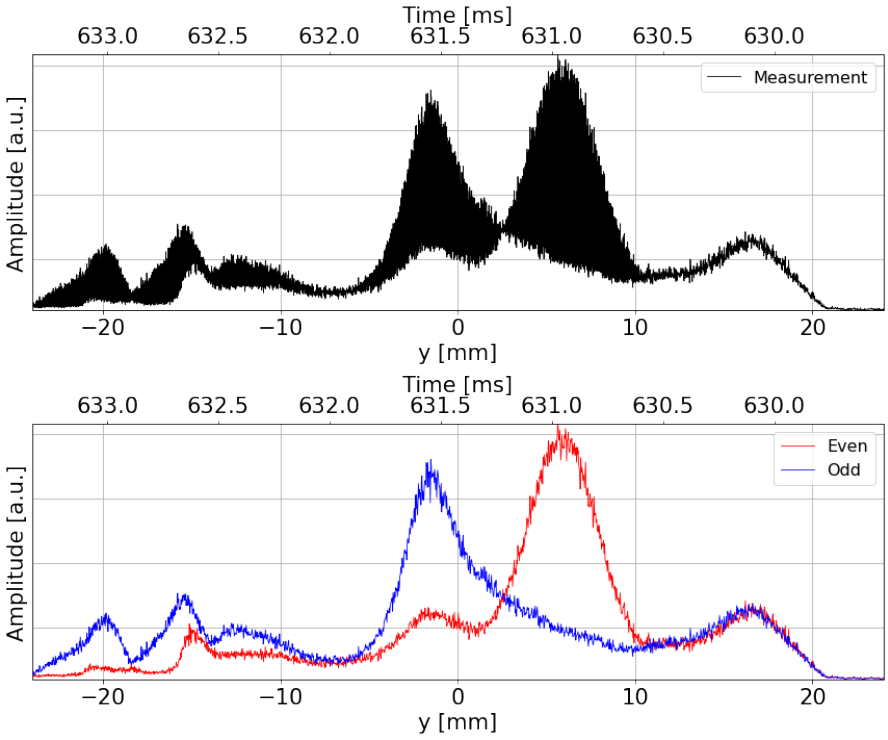

Figure 5.18: Top: example of a WS measurement of the vertical beam profile when crossing the half-integer resonance with strong space charge and just before the beam is lost. The horizontal bottom axis corresponds to the wire position, the horizontal top axis to the time of the scan (the wire speed is known) and the vertical to the wire scanner signal. Bottom: the same measurement but plotting odd and even turns with different colors.

hand, clear evidence for an asymmetric population of the two resonance islands were not found experimentally so far. By focusing on the WS signal between 629.5 and 630.5 ms of the bottom graph of Fig. 5.18, two equally populated islands seem to be present.

Finally, by the end of the scan, between 632.5 and 633.5 ms, some additional peaks are also recorded. At this point of the scan, the dynamical process that has induced these oscillations has resulted to most particles being already scraped by the machine aperture. The beam intensity has dropped almost to zero and only a few remaining residual particles are recorded. It is worth noting that by measuring with the WS at the exact same time span and with the same beam and machine conditions, the images can differ significantly. This is because the dynamical effects under these special beam conditions (strong space charge, slow crossing, etc.) are very fast and very sensitive to the exact initial beam parameters. It was observed for example, that the exact time span at which the beam is lost depends on fluctuations on the injected beam intensity. Nevertheless, images similar to the one with the two alternating peaks could be found every 10 or 15 measurements.

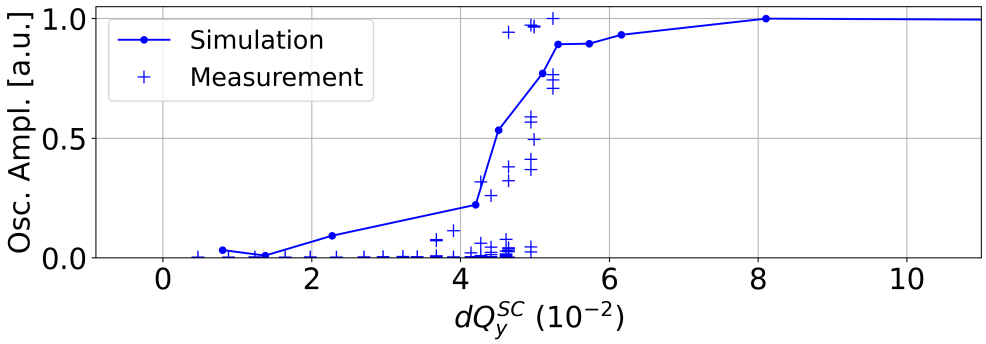

Figure 5.19: Measured maximum amplitude of a turn-by-turn pickup of the vertical beam position as a function of the space charge detuning in absolute value (blue crosses) while crossing the half-integer. Maximum transverse displacement of the vertical beam centroid when reproducing the same crossing in simulations (blue circles connected with solid lines).

Measurements with a turn-by-turn transverse position pickup were also performed while slowly crossing the half-integer resonance with a coasting beam. The blue crosses in Fig. 5.19 show the maximum amplitude of the pickup (in arbitrary units) as a function of the absolute value of the space charge detuning dQ_y^{SC}. The blue circles (connected with solid lines) represent the maximum transverse displacement of the vertical beam centroid when reproducing the same resonance crossing in tracking simulations, for which the following observations are made: For a very weak space charge ($dQ_y^{SC} < 0.01$) no oscillations are observed. When the space charge detuning increases ($0.01 < dQ_y^{SC} < 0.04$), the trapping occurs. The loss of the two beamlets of the resonance islands in the machine aperture, gives rise to small oscillations. When the space charge detuning increases even more ($dQ_y^{SC} > 0.04$), the population in the two islands is very asymmetric and this destabilizes the beam core before even the beamlets are lost. On the experimental side, the maximum vertical centroid displacement of the beam that is recorded with the turn-by-turn pickup follows a similar trend, although the agreement is not as good as the one

of Fig. 5.16. The oscillations that are recorded by the pickup are very fast with a rise time of less than 500 turns, as in the simulations.

The analysis presented so far suggest that the phenomenology of the beam behaviour when crossing the half-integer resonance with strong space charge is quite similar between the measurement and simulations. The loss pattern, the beam centroid pattern and the phase space projection in the vertical plane (measured with the WS) are almost identical. The asymmetry of the phase space population in the islands observed in the tracking simulations was not found experimentally. Furthermore, the mechanism which gives rise to these asymmetries in the simulation is not yet clear. This does not exclude the possibility of this effect being an artifact of the simulation and thus a general statement cannot be made.

5.3.3 Beam manipulations near the half-integer

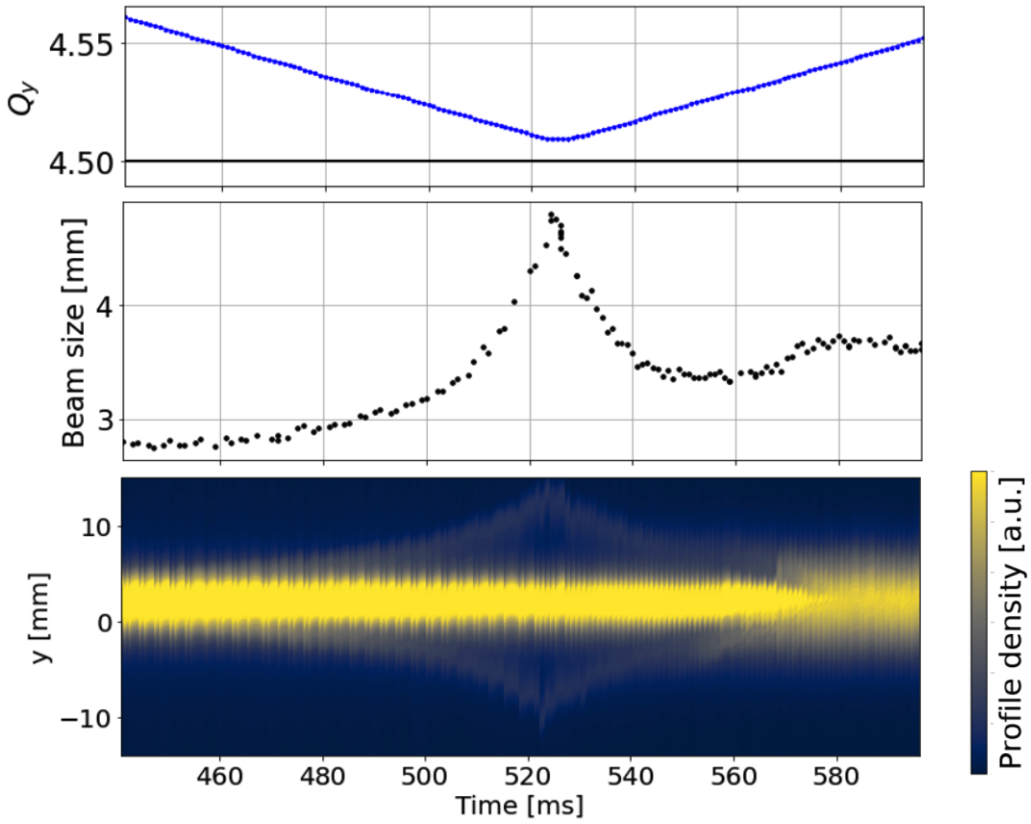

Figure 5.20: Top: vertical tune evolution as a function of time. Middle: vertical RMS beam size as a function of time. Bottom: vertical beam profile evolution as a function of time. While the half-integer is approached, the beam islands move outwards. When the tune is moved away from the half-integer, the beam islands move towards the center until they collapse with the beam core.

Other manipulations of the trapped particles in the half-integer resonance islands were also performed experimentally with a coasting beam. In Fig. 5.20, the half-integer resonance is again adiabatically approached, but just before the machine tune enters the stopband, the tune is moved away from the resonance (top plot). This results in the islands, along with the trapped particles (beamlets), first moving outwards. After the tune ramp changes slope, the islands move inwards, towards the beam core (bottom plot), and they become smaller. The particles that fall out of the islands fill the phase space around the beam core and the initial particle distribution cannot be restored. The collapse of the islands to the center results in a distribution with an RMS beam size increased by approximately 1 mm (middle plot).

Another process that was analyzed was the rotation of the phase space. This was performed by changing the phase of the exciting resonance driving term. Similarly to before, the half-integer resonance was excited using the two orthogonal quadrupole families (QNO412 and QNO816), the resonance was adiabatically crossed from above and the vertical profile was measured always at a specific distance from the resonance. However, instead of having a constant excitation at $\delta I_{816} = -2$ A, the phase of the excitation driving term was changed to different values by changing the current of the quadrupole families, as shown in the left plot of Fig. 5.21. The excitation amplitude was kept constant at $\delta I = \sqrt{\delta I_{816}^2 + \delta I_{412}^2} = -5$ A. This results to the rotation of the resonance phase space along with the resonance islands and the trapped beamlets. This rotation is shown in the right plot of Fig. 5.21.

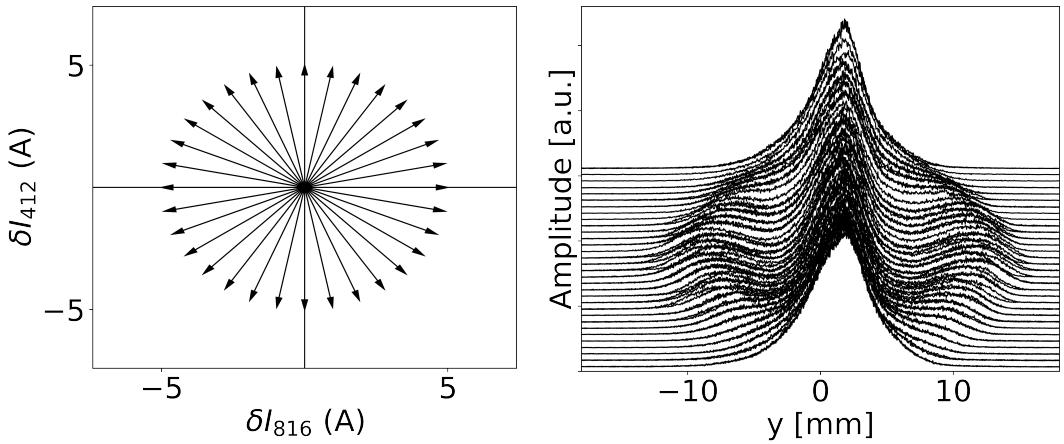

Figure 5.21: Left: illustration of the different driving terms used to excite the half-integer resonance (same amplitude and different phases). Right: measured vertical beam profiles with the WS at a fixed distance from the half-integer, plotted as a mountain range for different settings of the resonance excitation phase. The rotation of the driving term results to the phase space rotation

The trapped particles in the islands of the measured vertical profiles rotate around the beam center. For some excitation phases, the islands will not appear in the measured

profiles. This is because they are covered by the beam core in the projection onto the physical vertical plane measured by the WS. For a full rotation of the excitation driving term, the islands make a half-rotation. When reducing the intensity, and therefore the space charge, the islands become weaker and are closer to the beam core at the same distance from the resonance.

It is worth mentioning that this was one of the first experiments that were performed in this study. The ability to create an excitation driving term with any phase, allows to align the islands in such a way that they appear at the location of the profile monitor (here the WS). The excitation $\delta I_{816} = -2$ A and $\delta I_{412} = 0$ A was intentionally chosen for this reason.

5.4 Changing the Crossing Speed

The effect of the half integer resonance on the beam changes when crossing the resonance with different speeds. Figure 5.22 summarizes the macroscopic effects of the crossing speed on the beam. Here, the space charge detuning is approximately $\delta Q_y^{SC} \approx -30 \times 10^{-3}$. For a slow (adiabatic) crossing, like in the scenarios discussed so far, the probability of particles getting trapped in the moving islands is high [25]. Therefore, the islands are populated with plenty of particles that get carried outwards until they hit the machine aperture. This results to beam losses. In the graph, this is the case for crossing speeds that are lower than $\delta Q_y/\text{turn} \approx 60 \cdot 10^{-6}$. If the crossing is fast (non-adiabatic), the moving islands still capture particles but now there is a high probability that they will cross the separatrix and get unlocked from the resonance. This process results to an emittance growth without considerable losses. In the graph, this corresponds to crossing speeds higher than $\delta Q_y/\text{turn} \approx 60 \cdot 10^{-6}$.

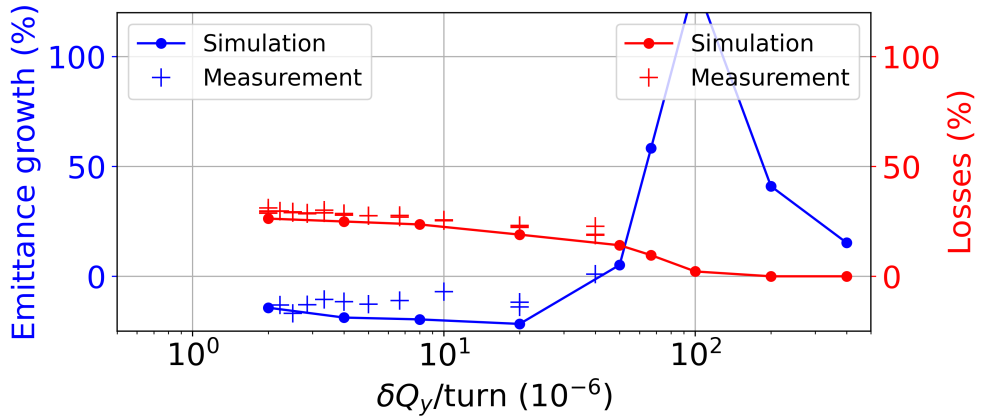

Figure 5.22: Emittance growth (blue) and beam losses (red) as a function of the crossing speed for a fixed space charge strength. The crosses represent experimental data and the circles (connected with solid lines) results from simulations.

In the same figure, the experimental data are plotted with the crosses and agree very well with the simulations. Unfortunately, tune changes faster than $\delta Q/\text{turn} \approx 50 \cdot 10^{-6}$ are too aggressive for the power converters of the PSB quadrupoles and cannot be achieved. Therefore, the non-adiabatic region cannot be reached experimentally for this configuration.

The limit between the adiabatic and non-adiabatic resonance crossing depends strongly on the size of the resonance islands. For bigger islands, the speed at which the crossing becomes non-adiabatic is larger. The size of the islands itself depends mostly on how strong is the resonance but also on the detuning gradient that is induced by space charge [24]. For $\delta Q_y^{SC} \approx -4 \cdot 10^{-2}$ and the resonance excited at $\delta I_{816} = -2$ A, a non-adiabatic crossing occurs for speeds higher than $\delta Q_y/\text{turn} \approx 60 \cdot 10^{-6}$, which corresponds to a crossing over approximately 4 ms. For the operational case of the PSB, at which the half-integer resonance is compensated and the tune gradient from space charge is much stronger, this speed will be much lower.

5.5 Effects of Chromaticity

Up to this point, the chromatic effects have been neglected because the vertical chromaticity had been corrected close to zero. The natural chromaticity in the vertical plane of the PSB is approximately $\xi_y \approx -1.60$ and the RMS momentum spread is roughly $\delta p/p \approx \pm 1.4 \cdot 10^{-3}$. This leads to a chromaticity induced tune spread of $\delta Q_{y,RMS}^{chrom} \approx \pm 0.01$, which is comparable to the space charge tune spread considered in this study here.

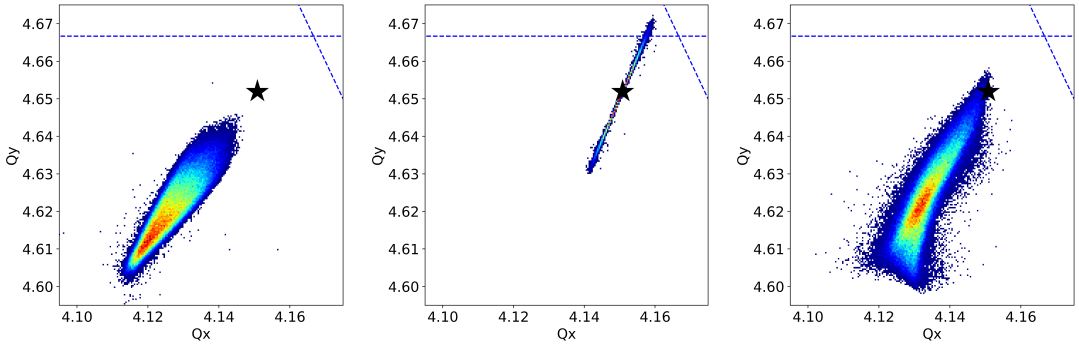

Figure 5.23: Space charge induced tune spread (left), chromaticity induced tune spread (center), tune spread from both space charge and chromaticity (right). In all cases the color code indicates the density of particles (red for high density of particles, blue for low density), and the particle tunes are obtained from the one turn phase advance from tracking. The set working point is shown with the black star.

Figure 5.23 shows how chromaticity can change the tune footprint induced by space charge. On the left tune diagram, the space charge induced tune shift of the individual particles is plotted. Since this tune shift is amplitude dependent, during the half-integer

crossing from above, stable islands appear which move outwards, as it was shown in the previous paragraphs. In the middle tune diagram, the tune spread induced by chromaticity is plotted. This depends on the momentum offset of individual particles and not on the particle transverse amplitude. Finally, in the right tune diagram, the combined tune spread of the two effects is plotted. In this case, particles with a specific momentum offset will see the resonance at different transverse amplitude than particles with a different momentum offset. For each value of the momentum offset, the resonance islands, if they appear in the phase space, will be at a different transverse amplitude.

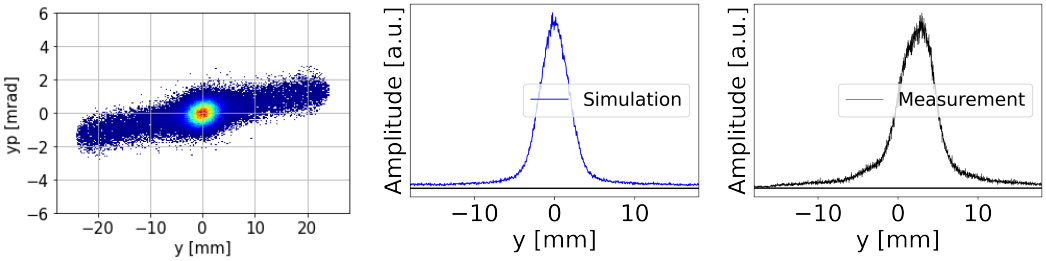

Figure 5.24: Left: vertical phase space of a coasting beam when crossing the half-integer with natural chromaticity (result from tracking simulation). Center: vertical beam profile of the phase space on the left. Right: vertical profile measured with a WS in similar beam conditions.

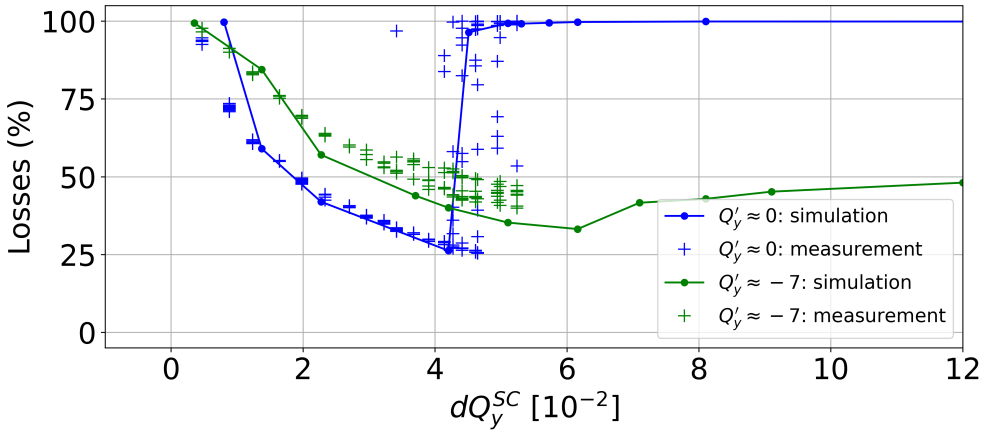

Figure 5.25: Beam losses as a function of the estimated space charge detuning in absolute value when adiabatically crossing the half-integer resonance for corrected (blue; same as Fig. 5.16) and natural (green) chromaticity. The crosses represent the experimental data points and the circles connected with solid lines the results from simulations.

Figure 5.24 shows the result of the combined space charge and chromaticity detuning when the beam crosses the half-integer resonance. The appearance of the islands at multiple amplitudes (for different momentum offsets) is revealed in the simulations as a

population of particles in a strip of the phase space. The middle plot shows the projection of the vertical phase space in the y-axis (i.e. the beam profile). The strip of particles is seen in the profile as large tails that reach the machine aperture. This profile is in a very good agreement with the real measured profile shown in the right plot, which has very similar beam characteristics.

Chromaticity seems to mitigate the strong losses, which were observed for the strong space charge detuning without chromaticity (see Section 5.3.2). Figure 5.25 compares the beam losses as a function of the space charge detuning for the cases of corrected (blue points; shown also in Fig. 5.16) and natural (green points) chromaticity. When chromaticity is kept natural, the beam remains stable for stronger space charge detunings. For $dQ_y^{SC} > 5 \cdot 10^{-2}$, with corrected chromaticity the full beam is lost, while with natural chromaticity the losses remain lower than 50 %.

5.6 Adiabatic Crossing of a Bunched Beam

In the analysis presented so-far, only coasting beams have been considered, which have a constant line density. The particles of a coasting beam still have an energy spread which nevertheless remains unchanged for individual particles. On the other hand, particles in bunched beams perform synchrotron oscillations. In the PSB with single harmonic RF, bunched beams usually have parabolic line densities. Individual particles oscillate in both the longitudinal position and energy (momentum) coordinates. The space charge detuning of a single particle depends on the bunch line density at its longitudinal position and therefore, due to the synchrotron motion, it modulates. This results in the periodic resonance crossing, as described in Section 2.5.

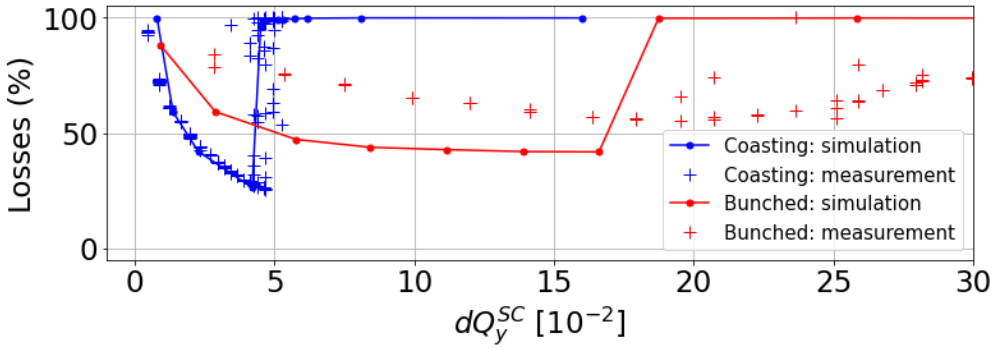

Figure 5.26: Beam losses as a function of the estimated space charge detuning in absolute value when adiabatically crossing the half-integer resonance from above for coasting (blue; same as Fig. 5.16) and bunched (green) beams. The crosses represent the experimental data points and the circles connected with solid lines the results from simulations. The vertical chromaticity is compensated.

Figure 5.26 compares the beam losses as a function of space charge for the cases of coasting (blue points; shown also in Fig. 5.16) and bunched (green points) beams. Here

the chromaticity is compensated in the vertical plane. In case of bunched beams, the losses are higher compared to the losses of the coasting beams. Also, the agreement between measurement (red crosses) and simulation (red circles/line) is not as good: approximately 10 % more particles are lost in the measured data. It is noted that in the case of the bunched beams, the emittances were not measured for each injected beam intensity, like it was done for the coasting beams, due to the limited available machine time. For the estimation of the space charge detuning for the bunched beams, it has been assumed that the emittance follows the same dependence on intensity as the one of the coasting beams. These estimations might thus not be as accurate. This could partially explain the disagreement between the measurement and simulation for $dQ_y^{SC} > 15 \times 10^{-2}$. Additional measurements are planned once the PSB restarts its operation in 2023, but this is beyond the scope of this thesis.

5.7 Systematic Scans

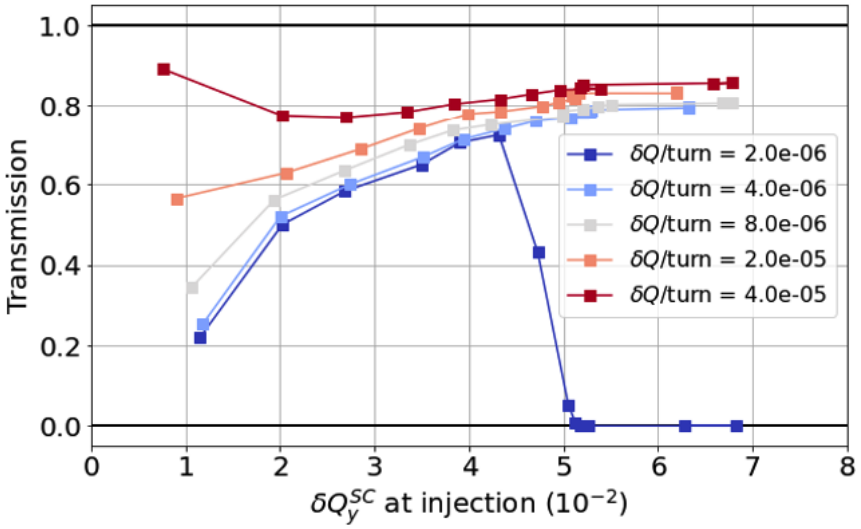

Figure 5.27: Transmission as a function of the space charge detuning dQ_y^{SC} for a coasting beam. The different colors correspond to different crossing speeds with blue being the slowest and red being the fastest crossing.

Systematic measurements were performed regarding the crossing of the half-integer resonance in order to derive scaling diagrams. Figure 5.27 shows the beam transmission of a coasting beam after crossing the half-integer as a function of the maximum space charge detuning. To estimate the space charge detuning, the beam intensity, the transverse emittances and the momentum spread were measured before the crossing. The estimations were done with PySCRDT [52]. The different colors correspond to different crossing speeds with blue being the slowest and red being the fastest crossing. It can be

seen that when crossing faster the transmission is better. For the slowest crossing (blue), above a certain space charge threshold, the transmission goes to zero. This is the case analyzed extensively in Section 5.3.2. For the faster crossing speeds, the transmission slightly increases with space charge due to the increase of the detuning gradient. As described in Section 5.4, the crossing is adiabatic in all cases in the sense that the trapping in the resonance islands always occurs (an emittance reduction due to the beam losses was measured in all cases)

Similar systematic scans for bunched beams were attempted but not completed due to the limited available machine time. Figure 5.28 shows the beam transmission of a bunched beam after crossing the half-integer resonance as a function of the beam intensity at injection (before the crossing). As before, the different colors correspond to different crossing speeds with blue being the slowest and red being the fastest crossing. The behaviour is similar to before: the transmission is better for faster crossings. Here, the data are not plotted as a function of the space charge detuning, because the emittances were not measured for the different beam intensities due to the 2022 year-end technical stop of the PSB. The systematic scan is planned to be completed in the 2023 run of the PSB, but this is beyond the scope of this thesis.

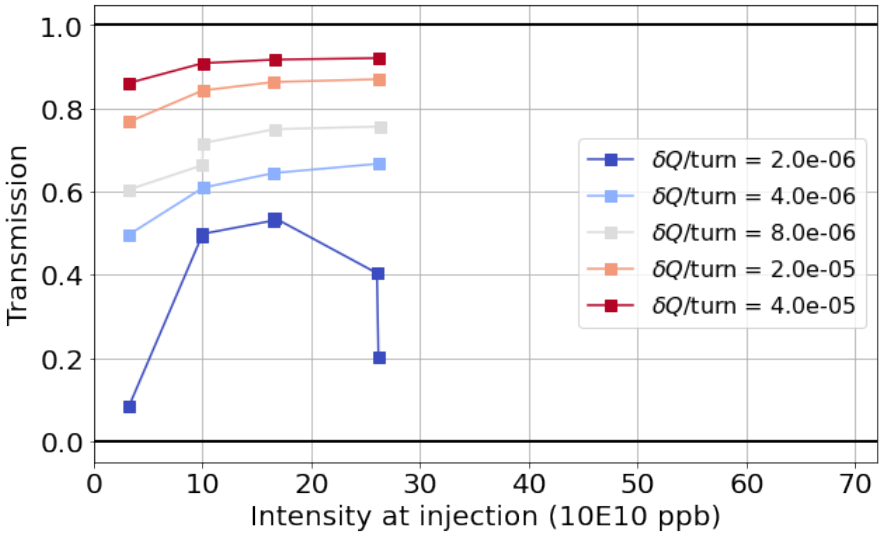

Figure 5.28: Transmission as a function of the space charge detuning dQ_y^{SC} for a bunched beam. The different colors correspond to different crossing speeds with blue being the slowest and red being the fastest crossing.

5.8 Crossing the Half-Integer from Below

The half-integer resonance crossing experiments discussed above were focused on dynamically crossing the resonance from above (from values $Q_y > 4.5$ to values $Q_y < 4.5$), due to the possible beam brightness gain for the PSB when increasing the vertical tune. A

few experiments were performed with dynamically crossing the half-integer from below (from values $Q_y < 4.5$ to values $Q_y > 4.5$), as discussed in the following. In this case, the dynamical evolution of the phase space is different. Figure 5.8 illustrated the phase space structure of a coasting beam near the half-integer resonance. It was discussed how the resonance islands will move towards larger amplitudes while the beam dynamically crosses the resonance from above. In the opposite crossing, the movement of the islands is reversed: they will appear at large amplitudes and, as the set tune Q_y increases and crosses the half-integer, the islands will move towards the beam center.

This effect was measured experimentally in the PSB for a coasting beam at injection energy (160 MeV) and was compared to tracking simulations. The top graphs of Fig. 5.29 show the measured vertical beam profiles at different vertical tunes ($Q_y = 4.47$, 4.52, 4.55 and 4.57) during the dynamic crossing of the half-integer resonance from below. This dynamic crossing was reproduced in tracking simulations with similar beam characteristics. The vertical phase spaces at the different vertical tunes as obtained in the simulations are shown in the bottom graphs of Figure 5.29. When the set tune and thus all beam particles have tunes below the resonance (left graph), its vertical profile follows a near Gaussian shape as no particles are inside the resonance islands. As the vertical tune increases, the resonance islands move towards the center of the phase space until they reach the boundary of the particle distribution. Particles get trapped in the islands or cross the separatrix and move towards larger amplitudes (beam profile and phase space of $Q_y = 4.52$). While the crossing continues, the islands become smaller and collapse to the center. The particles that had been trapped by the islands or that had been moved to larger amplitudes now fill the phase space resulting in emittance growth (beam profile and phase space of $Q_y = 4.55$ and $Q_y = 4.57$). The asymmetries observed in the measured profiles are associated with both the effect of the wire scattering, described in detail in section 4.3, and the non-negligible time it takes for the scan to be performed, described in detail in sections 5.3.2 and 5.3.1.

The emittance growth was systematically measured along the tune ramp. The top graph of Fig. 5.30 shows the measured vertical tune as a function of time during the dynamic crossing of the half-integer resonance from below. The crossing is done adiabatically over 100 ms, which corresponds to approximately 100 thousand revolutions at the injection energy of the PSB. The half-integer resonance was excited with the usual $\delta I_{816} = -2$ A shift in current of the QNO816 family, the vertical chromaticity was compensated and a coasting beam with an intensity of $N_b \approx 40 \times 10^{10}$ ppb, $\epsilon_x \approx 1.1$ μm, $\epsilon_y \approx 1$ μm and $\delta Q_y^{SC} \approx -40 \times 10^{-3}$ was used. The bottom graph shows with the blue crosses the measured vertical emittance as a function of the tune. The vertical emittance grows linearly between $Q_y = 4.5$ and $Q_y = 4.545$ while dynamically crossing the resonance to a value of approximately $\epsilon_y \approx 2.3$ μm. This behaviour is not reproduced very well in the simulation model, shown with the red line, in which the emittance growth is non-linear and faster (between $Q_y = 4.52$ and $Q_y = 4.535$). However, the initial emittance of the simulation was slightly smaller compared to the measurement. Despite the quantitative differences, the emittance growth measured in the PSB is qualitatively reproduced in simulations and has the same order of magnitude.

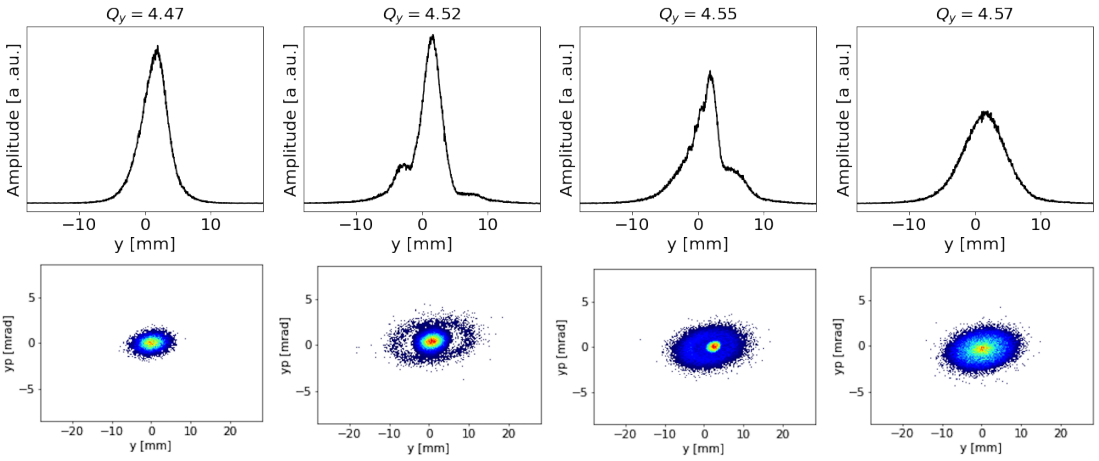

Figure 5.29: Top: vertical beam profile measurements with the WS at different tunes during the dynamic crossing of the half-integer resonance from below (wire scan is performed from the positive y-values to the negative y-values). Bottom: snapshots of the vertical phase space (at the same tunes as the top graphs) when reproducing the same dynamic crossing in tracking simulations with PyOrbit.

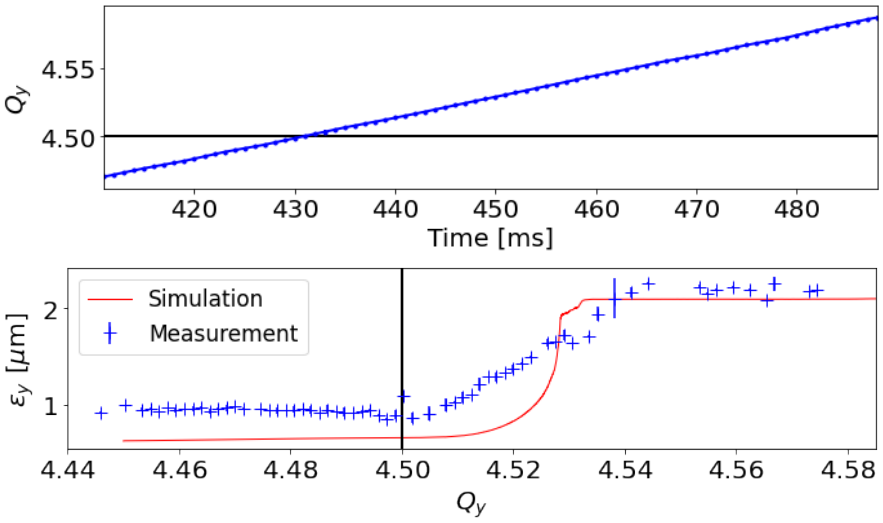

Figure 5.30: Top: measured vertical tune as a function of time when dynamically crossing the half-integer resonance from below. Bottom: measured vertical emittance (blue crosses) and emittance from simulation (red line) as a function of the vertical tune.

It is noted that the emittances were not measured during one cycle of the PSB but instead each data point comes from a different PSB cycle with the same beam and machine configurations (similar beam intensities, emittances, crossing speed, chromaticity correction). The bottom graph of Fig. 5.30 is composed by combining the emittance

measurements by all the different PSB cycles.

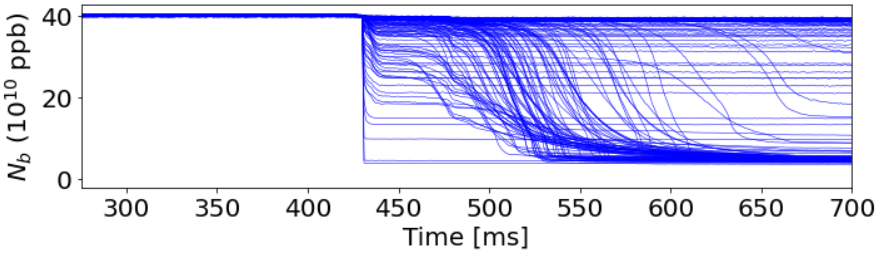

Figure 5.31: Measured beam intensity evolution for the different PSB cycles when crossing the half-integer. The transmission fluctuates considerably.

It is important to mention that the beam transmission fluctuated considerably between the different PSB cycles while dynamically crossing the half-integer resonance from below. Although the cycles were identical with respect to each other, for some cycles the beam transmission would be almost 100 %, for some cycles would be between 90 % and 20 % and for some cycles would even go as low as 5 %. This effect is shown in Fig. 5.30 and was observed also in the stopband width measurement (see Fig. 5.3). The origin of these losses is not understood. The emittances shown in Fig. 5.30 concern only the cycles in which the transmission was 98 % or better, not the cycles that had higher losses.

Chapter 6

Operation Above the Half-Integer Resonance

6.1 Crossing under Operational Conditions

In the previous chapter, the half-integer resonance crossing was characterized in a variety of precisely controlled beam and machine conditions. Systematic measurements were presented with coasting and bunched beams, compensated and natural chromaticity and different crossing speeds. The results were compared to tracking simulations. In all cases the half-integer resonance was deliberately excited and its stopband width was measured experimentally.

The characterization of the half-integer resonance effects are of operational interest for the PSB. An injection above the half-integer resonance could further mitigate the space charge induced blow-up at low energy. By minimizing the beam degradation during the dynamic crossing of the half-integer resonance, this could result to an increased beam brightness.

The operational beam conditions of the PSB are more complicated than the cases that were studied separately in the previous chapter. The beams are injected at $t = 275$ ms and after only 1-2 ms the acceleration starts and it finishes just before extraction at $t = 805$ ms. Thus, the space charge tune spread dynamically decreases during the cycle. The beams are bunched and to reduce the peak line density, and therefore the space charge detuning, the beams are injected in a double harmonic bucket. The bunch shape dynamically changes to a single harmonic parabolic distribution along the cycle. Still, at injection the space charge tune spread exceeds $\delta Q_{x,y}^{SC} = -0.5$, and so, to avoid beam degradation by the integer resonances, the working point is usually at $(Q_x, Q_y) = (4.40, 4.45)$. The working point is dynamically changed to $(Q_x, Q_y) = (4.17, 4.23)$ within the cycle. Multiple 3^{rd} and 4^{th} order resonances are dynamically crossed during the tune change, which are nevertheless compensated to a very good extend [22]. Finally, the horizontal and vertical chromaticity is kept natural.

Figure 6.1 shows a possible scenario for the injection above the half-integer resonance under operational beam conditions. The black solid line represents the vertical tune Q_y

as a function of time. In this example the beam is injected above the half-integer resonance $2Q_y = 9$ which is shown as a red line. The injection working point is denoted as $Q_y = Q_1$. The beam is injected at $t = 275$ ms and stays above the half-integer until $t = t_1$. This time needs to be relatively long so that the space charge tune spread has decreased enough (due to the energy increase which is shown in blue) before dynamically crossing the resonance. On the other hand, by staying above the resonance for a long time, beam degradation may occur due to the periodic resonance crossing as usually a residual resonance excitation cannot be avoided even after compensating the resonance. The time t_1 can correspond to hundreds of thousands of revolutions which can induce measurable emittance increase or tail formation. The optimal value for t_1 needs to be found experimentally. After, the half-integer resonance is dynamically crossed as fast as possible in order to minimize particle trapping. A second tune plateau follows at $Q_y = Q_2$ below the resonance until the time $t = t_2$. Finally the tune ramps down to the extraction value $Q_y = 4.23$ and the beam crosses the higher order resonances. The horizontal tune Q_x is kept constant at 4.40 (below the half-integer resonance) until $t = t_2$ at which point it ramps down to the extraction value $Q_x = 4.17$

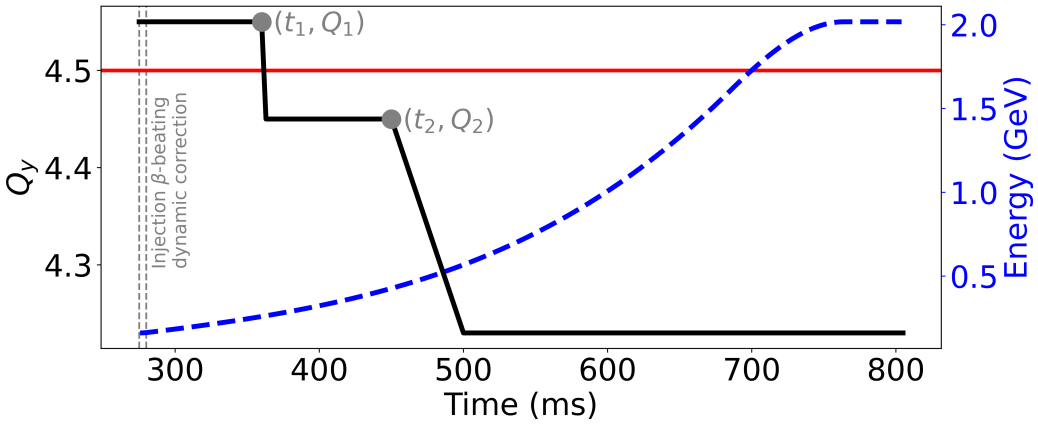

Figure 6.1: Example of a vertical tune evolution as a function of time for an injection above the half-integer resonance. The red line represents the half-integer resonance, the tune plateau above the half-integer resonance is at $Q_y = Q_1$ until time $t = t_1$, a fast dynamic crossing of the half-integer follows and the tune plateau below the half-integer is at $Q_y = Q_2$ until time $t = t_2$. The beam energy is shown with a blue dashed line in the secondary vertical axis.

6.2 Optimization of the Half-Integer Crossing

A number of parameters require optimization in the previous crossing scenario in order to minimize the beam degradation. For example, the optimal injection tune plateau at $Q_y = Q_1$ (until time $t = t_1$) might change with beam intensity. The half-integer

resonance compensation that minimizes the stopband width might need to be revised. These parameters have been optimized experimentally and will be presented in the following paragraphs. The other parameters, like the second tune plateau at $Q_y = Q_2$ (until time $t = t_2$) or the compensation of the 3rd and 4th order resonances, have remained fixed in this analysis.

There are mainly two sources of errors that excite the half-integer resonance in the PSB. The injection chicane perturbations, discussed in detail in Chapter 3, is one of them. Although these localized focusing errors are fast (they last only 5 ms after injection), at the same time they are very strong and can have significant impact on the beam, as shown in Fig. 6.2. The left graph shows different dynamic corrections of the injection chicane perturbations applied in QDE3 and QDE14 (similar to Fig. 3.17) in the real machine. The right graph shows the vertical profiles measured with the WS at $t = 280$ ms (right after the injection chicane collapse), for the working point of $(Q_x, Q_y) = (4.40, 4.55)$ and color-coded based on the different dynamic corrections of the left graph. It can be seen that when the injection chicane dynamic correction is reduced close to zero (blue colors), the profiles are heavily distorted: particles are lost (the profile area is reduced) and very strong tails are formed. The dynamic correction that best compensates the injection perturbations and minimizes the beam tails is in the region with the orange colors. This was the dynamic correction that was used during the half-integer crossing.

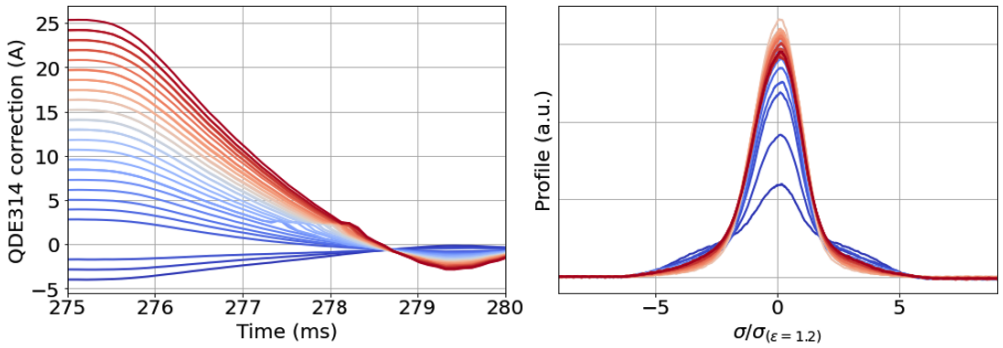

Figure 6.2: Left: different dynamic corrections of the injection chicane perturbations applied in QDE3 and QDE14 of the PSB. Right: impact of the measured vertical profile at $t = 280$ ms (color-coded based on the different dynamic corrections).

The second source of errors that excites the half-integer is much weaker than the injection chicane perturbations but it is not localized. It is the combination of random focusing errors of the different quadrupoles of the PSB and possibly feed-down effects from higher order multipoles. A systematic correction of these errors, as described in Section 5.2.1, has been made only at the injection energy of the PSB. The behaviour of the half-integer resonance at higher energies (e.g. the early part of the acceleration ramp) has not yet been studied.

Figure 6.3 shows an experimental technique that was used to minimize the strength of the half-integer resonance based on beam losses. On the left graph, a relatively

slow crossing was set in the vertical tune (to increase the sensitivity on losses) and the beam intensity was recorded between points 'A' and 'B' (before and after the crossing). This measurement was repeated with different configurations of the two orthogonal quadrupole corrector families QNO816 and QNO412. The current of the quadrupole correctors is shown in the horizontal and vertical axis of the right graph and the color of the points corresponds to the recorded losses between 'A' and 'B'. With this method, the point with the minimal losses is found at approximately $I_{\mathrm{QNO816}} = -3.0$ A and $I_{\mathrm{QNO412}} = 7.1$ A. The beam losses at this point are approximately 4 %. Obviously, if the crossing of the half-integer is faster, the losses become less than 1 %.

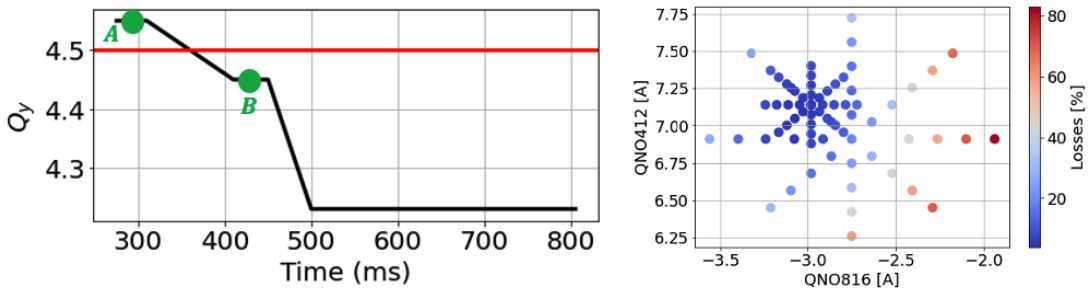

Figure 6.3: A method for experimentally compensating the half-integer resonance based on losses. Left: tune evolution for a slow crossing of the half-integer. Right: losses before (point 'A') and after (point 'B') the crossing for different configurations of the QNO816 and QNO412 correctors (right).

A second technique was used to experimentally compensate the half-integer resonance based on the shape of the vertical beam profiles. Instead of crossing the half-integer resonance, a long tune plateau above the resonance is programmed between $t = 275$ ms and $t = 450$ ms as shown in the left graph of Fig. 6.4. Due to the space charge detuning, particles with large synchrotron oscillation amplitudes will perform periodic resonance crossing and slowly drift towards larger amplitudes and the profiles will be distorted. This distortion can be characterized by the q-parameter of the q-Gaussian function. The vertical profiles are measured with the WS in points 'A' and 'B': at the beginning of the cycle and after they have spent hundreds of thousands of turns on the resonance. This measurement is repeated for multiple configurations of QNO816 and QNO412 and all the profiles are then fitted with the q-Gaussian function. The left picture shows the q-factor of the profiles at point 'A' (green) and at point 'B' (red) as a function of the QNO816 current while QNO412 was fixed. It can be seen that there is a tail population increase between profiles in point 'A' and point 'B' (q-factor increases between green and red points) due to the periodic resonance crossing. This generation of tails is minimized at approximately $I_{\mathrm{QNO816}} = -3.2$ A. Similar plots were made for other values of the QNO412 family. Both methods converge to the same configuration for QNO816 and QNO412 corrector currents, which suggests that this is the optimal compensation of the half-integer resonance that can be achieved.

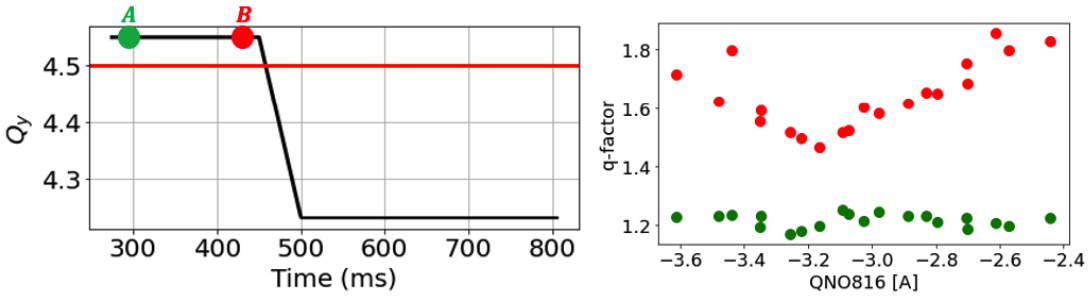

Figure 6.4: A method for experimentally compensating the half-integer resonance based on the shape of the vertical profiles. Tune evolution for a plateau above the half-integer (left) and q-factor of the q-Gaussian fit of the vertical profiles of point 'A' (green) and point 'B' (red) (right).

The second method can enhance the sensitivity of the compensation since no losses are needed in order to find the minima in the scan of the quadrupole currents. It is then an improved method compared to the more traditional one based on beam losses. This method also shows how the q-factor from the q-Gaussian fit of the measured profiles can be a good observable for such profile distortions. Figure 6.5 shows two examples of the measured profiles and their corresponding q-factors. The left corresponds to the vertical profiles between point 'A' and point 'B' of Fig, 6.4 for $I_{\mathrm{QNO816}} = -2.5A$ and the right for $I_{\mathrm{QNO816}} = -3.2A$ (optimal). It can be seen that even in the optimal configuration there is still some tail formation during the long tune plateau above the half-integer resonance, which means that the resonance is not compensated perfectly. For this reason, in practice the crossing needs to be as fast as possible and the tune plateau (t_1, Q_1) as short as possible. Finally, it should be noted that already at injection the profiles have some overpopulated tails (q-factor for point 'A' is approximately 1.2), as discussed in Chapter 4, and ther are thus not perfectly Gaussian.

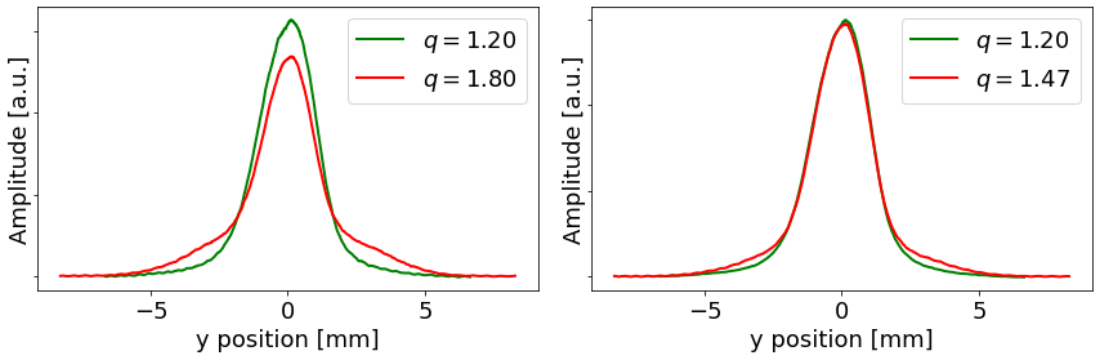

Figure 6.5: Measured profiles between point 'A' and point 'B' of Fig. 6.4 for $I_{\mathrm{QNO816}} = -2.5A$ (left) and $I_{\mathrm{QNO816}} = -3.2A$ (right). The corresponding q-factors are shown in the labels.

The Q_1 and t_1 parameters of the vertical tune ramp were also optimized. Figure 6.6 shows the vertical q-factors of the vertical beam profiles (left graph) and the vertical beam emittance (right graph) for different values of Q_1 and t_1. The beam was injected at three different vertical tunes ($Q_1 = 4.52$, $Q_1 = 4.55$ and $Q_1 = 4.56$) and the half-integer crossing started at three different times ($t_1 = 300$ ms, $t_1 = 350$ ms or $t_1 = 400$ ms). Multiple measurements were performed for each case and the q-factors and emittances were averaged an plotted with the color-code shown on the right side of the two graphs. The beam intensity was kept fixed at $N_b = 165 \times 10^{10}$ ppb.

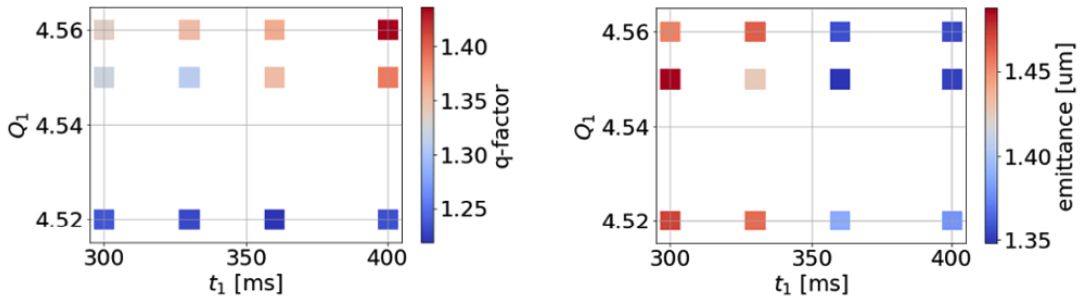

Figure 6.6: Left: q-factor of the vertical beam profiles for different three Q_1 values and three different t_1 values. Right: vertical beam emittance for the same (Q_1, t_1) pairs.

On the left graph of Fig. 6.6, it can be noticed that the longer the beam stays above the half-integer (larger t_1) the more the tails are populated (q-factor increases) and the emittance slightly decreases. This effect is similar for other beam intensities. On the other hand, the $Q_1 = 4.52$ gives lower tails (lower q-factor) and relatively similar emittances. For a higher beam intensity, injection at a higher verical tune is needed ($Q_1 = 4.55$ or $Q_1 = 4.56$) to have lower tails and lower emittances. Concerning the beam intensities of the high-brightness LHC beams, the pair $(t_1, Q_1) = (400, 4.55)$ was chosen as the best compromise between low tails and low emittances.

6.3 Impact on Beam Brightness

Following the optimizations of the half-integer resonance crossing, the brightness curve was measured at extraction of the PSB and compared to the optimal brightness when staying below the half-integer resonance. The latest brightness measurements in the PSB are shown in Fig. 6.7. The green data points represent the brightness when injecting below the half-integer resonance. To get beyond LIU target brightness, the injection chicane beta-beating correction and the resonance compensation scheme for the higher order resonances are needed, as discussed in Chapter 3. The blue data represent the brightness when injecting above and dynamically crossing the half-integer resonance. Here, the optimizations discussed in the previous section have been applied.

Two conclusions can be drawn from this figure. Firstly, although an extremely challenging exercise, the dynamic crossing of the half-integer resonance is feasible with

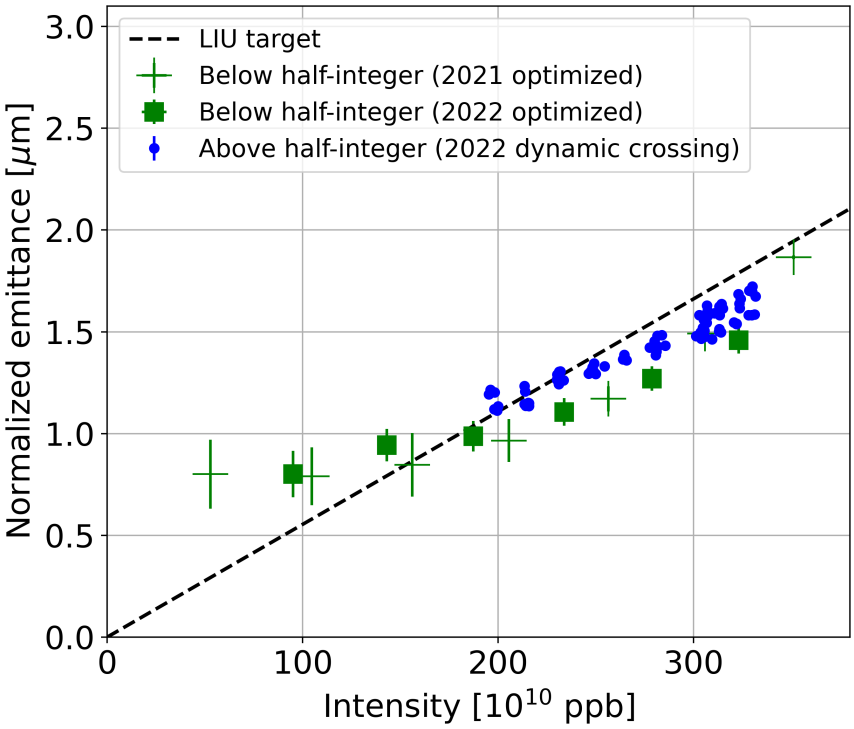

Figure 6.7: Brightness comparison from injecting below and above the half-integer resonance.

a very decent beam quality. The brightness still exceeds LIU target, with an average emittance (horizontal and vertical) of approximately 1.7 μm for a beam intensity of 320×10^{10} ppb, and the profile shapes are similar with the ones of injection below the half-integer. The second conclusion is that so far, by injecting above the half-integer resonance there is no observable brightness gain compared to the optimized scenario below the half-integer, at least for beam intensities up to 320×10^{10} ppb.

There are possible reasons that could explain the brightness performance of the PSB being the same below and above the half-integer. If the brightness is limited only by the space charge effects at injection as explained in Chapter 2, in order to reach this limit with the injection above the half-integer, much higher beam intensities might be needed. The injection above the half-integer could give a gain in intensity instead of the emittance. Unfortunately, higher intensities could not be tested due to high injection and capture losses as the injection and the beam capture had been optimized for tunes below the half-integer resonance. Although the optics do not change dramatically above the half-integer, higher losses were observed both when injecting and capturing the beam and the beam loss monitors would reject the beam. In future studies, the brightness should be re-measured with optimized beam injection and capturing. Furthermore, the only emittance gain that is expected is from the vertical profiles, since the horizontal tune

in the early part of the cycle has remained constant at $Q_x = 4.40$, below the horizontal half-integer resonance $2Q_x = 9$. To get an increased brightness, this tune might also need to be changed.

Chapter 7

Summary and Conclusions

The LIU project aimed at improving the injectors and eventually increasing the collision rate at the LHC. These major upgrades were carried out mostly during LS2 and were successfully completed by 2021. The PSB upgrades revolved around mitigating the space charge effects at injection. At high beam intensities, space charge drives particles through the detuning into the strongly excited resonances causing emittance blow-up. Because this effect reduces at higher energies, the injection energy of the PSB was increased within LIU (and also the extraction energy to reduce space charge effects in the PS). Furthermore, the multi-turn injection was replaced with an H^- charge-exchange system resulting in an essentially loss-free injection and allowing a far better control of the beam intensity and emittance.

The figure of merit for describing the performance of the injectors regarding the LHC beams is the beam brightness. The work performed within this thesis aimed at optimizing the brightness performance of the PSB by conducting a number of studies in the transverse planes: the correction of the injection chicane induced optics perturbations, the improvement of the transverse beam profiles and the dynamic crossing of the half-integer resonance.

In Chapter 3, it was shown that the H^- injection induces focusing errors that perturb the optics of the machine in the form of β-beating and tune distortions. These optics perturbations are strongly enhanced near the half-integer resonance. Operation with working points that are close to the half-integer resonance is however essential to further reduce the beam degradation due to space charge effects at injection. The optics perturbations were modelled in detail using the PSB model lattice and methods were developed to measure and dynamically correct these perturbations based on k-modulation. During LS2, these methods were tested extensively by numerous sensitivity simulation studies under realistic machine conditions and were found very robust and suitable for the PSB needs. Thereafter, they were implemented into an operational GUI application that was used during the 2021 and 2022 beam commissioning. The successful measurement and dynamic correction of the β-beating and tune at injection not only demonstrated how well the modelling of the accelerator was carried out, but also opened the way for optimizing the working point and tune evolution at injection. This contributed to

an increased beam brightness that exceeds the targets of the LIU project for the PSB, already in the first operational year after the implementation of the upgrades.

The control of the optics perturbations is of fundamental importance for any accelerator. Methods similar to the one developed for the PSB could be applied in other machines that suffer from localized focusing errors, like the ones of the H^- injection system. With the cost of only powering a few quadrupoles near the focusing errors and a tune measurement device, the β-beating can be measured and corrected even dynamically within the cycle.

In Chapter 4 the shape of the transverse beam profiles in the PSB was studied. This is the first systematic study in the LHC injectors regarding the non-Gaussian tails observed in the transverse profiles after the LIU upgrades. The non-Gaussian tails were modelled with the q-Gaussian function which uses the q-parameter to characterize the tail population. The tails were characterized experimentally for different working points and intensities and their formation mechanisms were associated in most cases with the periodic resonance crossing induced by the space charge detuning. Furthermore, the reconstruction of the profiles with the Wire Scanner and their impact on the beam was addressed using both measurements and simulations. The behaviour of the beam core (in terms of emittance growth) and the beam tails (in terms of asymmetric tails) at the injection energy of the PSB was well explained by the scattering induced by the beam-wire interaction. The wire scattering was reproduced in a detailed simulation model, the benchmarking of which with measured profiles, provided a method for estimating the wire width and scattering angle. Ways for accounting for the scattering effects due to the beam-wire interaction where developed with the use of the q-Gaussian function which resulted in an improved reconstruction of the measured profiles for the first time.

A big effort is presently ongoing at CERN to characterize the beam profiles and tail evolution not only in the PSB but along the whole injectors chain. Currently, the q-Gaussian function is used to model the transverse beam profiles in the PSB, PS and SPS and has provided plenty of insights regarding the tail enhancement mechanisms. The control of the shape of the transverse beam population is necessary for assessing the beam emittance, the beam brightness and eventually the luminosity in the LHC. Furthermore, the modelling of the beam-wire interaction provides an interesting framework for analyzing wire scattering effects on the beam that dynamically change over time. By going beyond the PSB parameter regime, one can study how a particle distribution and the macroscopic properties of a beam (emittance, intensity, etc.) evolve under time-varying but localized particle wire scattering.

In Chapters 5 and 6 the feasibility of operation of the PSB above the half-integer resonance was investigated. The upgrade of the PSB allowed the experimental characterization of space charge effects of the half-integer resonance crossing. A method to experimentally determine the half-integer resonance stopband was developed and the adiabatic trapping of particles of a coasting beam on the half-integer resonance islands was measured clearly for the first time. Furthermore, the effects of the different crossing speeds, chromaticity and periodic resonance crossing of bunched beams were also addressed in detail. All the measurements were accompanied by detailed space charge

tracking simulations and the agreement between the two was excellent in most of the cases. The understanding of these effects allowed for the injection above the half-integer resonance and the dynamic crossing during the acceleration cycle with minimal beam degradation. Although this is not currently used operationally, it was shown that the dynamic crossing is feasible with a beam brightness still exceeding the LIU targets.

There are some open points that still need to be addressed in future studies. The beam behaviour when adiabatically crossing the half-integer resonance using a coasting beam with very strong space charge is not fully understood. Phenomenologically, the beam displays similar effects under these conditions both in measurements and simulations (all the beam particles are lost and there is some kind of oscillatory motion being present), but the reasons for these effects are not completely clear. The PSB will restart in 2023 and more measurements are planned. The effects of space charge near the half-integer resonance are of general interest for any high-intensity accelerator at low energy. The flexibility of the PSB in terms of parameter regimes that it can reach, can contribute in further exploring the scaling laws of the half-integer resonance crossing (similar to the ones of Section 5.7) for different resonance strengths and possibly allow the dynamic crossing of the half-integer resonance for other accelerators as well.

Appendix A

Relevant Beam Dynamics Concepts

A.1 Quadrupolar perturbations

Analysis based on [6]. A quadrupole perturbation introduces a variation in the amplitude and the phase of the betatron oscillations, with the centre of the oscillations remaining the same as without the perturbation. The perturbed Hamiltonian is:

$$\hat{\mathcal{H}} = \frac{p_x^2}{2} + \frac{k_x}{2}x^2 + \frac{V_1(s)}{2}x^2 \tag{A.1}$$

which gives an equation of motion:

$$x'' + k_x(s)x = V_1(s)x. \tag{A.2}$$

V_1 can represent a quadrupole kick, a weak focusing or a multipole feed-down. The equation of motion in normalized coordinates $x_n = x/\sqrt{\beta_x}$ and $\psi_{nx} = \oint 1/(\beta_x Q_0)ds$ is:

$$\frac{d^2x_n}{d\psi_{nx}^2} + Q_0^2 x_n = V_1(s)Q_0^2\beta_x^2(s)x_n \tag{A.3}$$

with a homogeneous solution:

$$x_n^{(homo)} = \sqrt{2J_x}cos\left(Q_0\psi_{nx}\right) \tag{A.4}$$

A partial solution to the inhomogeneous equation can be found using the Green's function:

$$x_n^{(part)} = \int_0^{\psi_{nx}} V_1(\chi)Q_0^2\beta_x(\chi)^2 x_n(\chi)G(\chi)d\chi \tag{A.5}$$

$$G = \frac{\sqrt{2J_x}sin\left[Q_0(\psi_{nx} - \chi)\right]}{Q_0} \tag{A.6}$$

which depends on x_n. By substituting x_n with $x_n^{(homo)} \equiv x_{n,0}$, one can find the total solution as:

$$x_n^{(total)} \equiv x_{n,1} = x_{n,0} + x_n^{(part)}(x_{n,0}) \tag{A.7}$$

A solution of any order can be obtained recursively by using:

$$x_{n,i+1} = x_{n,0} + x_n^{(part)}(x_{n,i}) \equiv \sqrt{2J_x} cos\left(Q_0 \psi_{nx}\right) + x_n^{(part)}(x_{n,i}) \tag{A.8}$$

with $i = 0, 1, 2, ...$ For a small perturbation, the total solution will still have a form of a harmonic oscillation:

$$x_{n,i+1} = \sqrt{2J_x} cos\left(Q \psi_{nx}\right) \tag{A.9}$$

with $Q = Q_0 + \delta Q$. By combining eq. A.8 with eq. A.9, one can get algebraic equations for δQ that can be solved either numerically or analytically with the appropriate approximations.

For example, the first order equation for δQ after one turn ($\psi_{nx} = 2\pi$) is:

$$cos\left[2\pi(Q_0 + \delta Q)\right] = cos(2\pi Q_0) + Q_0 \int_0^{2\pi} \beta_x^2(\chi) V_1(\chi) cos(Q_0 \chi) sin\left[Q_0(2\pi - \chi)\right] d\chi \tag{A.10}$$

which when solved using the small-angle approximation for a weak perturbation, gives:

$$\boxed{\delta Q = -\frac{1}{4\pi} \oint \beta_x(s) V_1(s) ds - \frac{1}{4\pi sin(2\pi Q_0)} \oint \beta_x(s) V_1(s) sin\left[2Q_0(\pi - \psi_{xn}(s))\right] ds} \tag{A.11}$$

This shows that the quadrupole perturbation induces a tune shift that is proportional to the beta function at the position of the perturbation and also the strength of the perturbation V_1. The second term averages to zero over many turns but reveals that if the initial tune is equal to an integer or a half-integer, namely $Q_0 = n$ or $Q_0 = \frac{1}{2}n$ with $n \in \mathbb{Z}^*$, a resonance condition occurs and the beam gets unstable.

For stronger perturbations, or for tunes closer to an integer or a half-integer value, higher orders of eq. A.10 are needed. In second order of δQ, this equation becomes:

$$\begin{aligned} cos\left[2\pi(Q_0 + \delta Q)\right] = cos(2\pi Q_0) + \\ Q_0 \int_0^{2\pi} \beta_x^2(\chi) V_1(\chi) cos(Q_0 \chi) sin\left[Q_0(2\pi - \chi)\right] d\chi \\ Q_0^2 \int_0^{2\pi} \beta_x^2(\chi) V_1(\chi) \left(\int_0^{\chi} \beta_x^2(\zeta) V_1(\zeta) cos(Q_0 \zeta) sin\left[Q_0(2\pi - \zeta)\right] d\zeta \right) sin\left[Q_0(2\pi - \chi)\right] d\chi \end{aligned} \tag{A.12}$$

The second order approximation reveals that the beam gets unstable not only at exactly integer or half-integer tunes, but also in a region around these. This region is known as the resonance stopband. After expanding eq. A.12 to second order in δQ, it takes the form:

$$\begin{cases} cos\left[2\pi(Q_0 + \delta Q)\right] - 1 = -2\pi^2 \delta Q^2 + 2\pi^2 F_0 \delta Q + \frac{1}{8}\pi^2 (F_{2n}^2 - 4F_0^2), & \text{for } Q_0 \approx n + \delta Q \\ cos\left[2\pi(Q_0 + \delta Q)\right] - 1 = -2\pi^2 \delta Q^2 - 2\pi^2 F_0 \delta Q - \frac{1}{8}\pi^2 (F_{2n+1}^2 - 4F_0^2), & \text{for } Q_0 \approx n + \frac{1}{2} + \delta Q \end{cases} \tag{A.13}$$

where n is integer and:

$$F_0 = \frac{1}{2\pi} \oint \beta(s) V_1(s) ds \tag{A.14}$$

$$F_q = \frac{1}{\pi} \oint \beta(s) V_1(s) e^{-iq\psi_{nx}(s)} ds \tag{A.15}$$

If the r.h.s of eq. A.13 are greater than zero, the δQ is imaginary and the resonance condition occurs. This defines the boundaries of the stopband:

$$\begin{cases} \delta Q_{1,2} = \frac{1}{2} F_0 \pm \frac{1}{4} |F_{2n}| & \text{for } Q_0 \approx n + \delta Q \\ \delta Q_{1,2} = \frac{1}{2} F_0 \pm \frac{1}{4} |F_{2n+1}| & \text{for } Q_0 \approx n + \frac{1}{2} + \delta Q \end{cases} \tag{A.16}$$

and the stopband width is:

$$\begin{cases} W_1 = \delta Q_1 - \delta Q_2 = \frac{1}{2} |F_{2n}| & \text{for } Q_0 \approx n + \delta Q \\ W_{1/2} = \delta Q_1 - \delta Q_2 = \frac{1}{2} |F_{2n+1}| & \text{for } Q_0 \approx n + \frac{1}{2} + \delta Q \end{cases} \tag{A.17}$$

The quadrupolar perturbations cause also variations in the β-function. Following a similar analysis it can be shown that, in first order approximation, these perturbations take the form:

$$\boxed{\frac{\delta\beta_x(s)}{\beta_x(s)} = \frac{1}{2sin(2\pi Q_0)} \oint \beta_x(s_1) V_1(s_1) cos\left[2Q_0(\psi_{nx}(s) - \psi_{nx}(s_1) + \pi)\right] ds_1} \tag{A.18}$$

This variation is known as β-beating. The β-beating becomes infinite at the integer and half-integer tunes. In normalized coordinates, one finds that the β-beating frequency is twice the tune frequency:

$$\frac{d^2}{d\psi_{nx}^2} \left(\frac{\delta\beta_x}{\beta_x} \right) + (2Q_0)^2 \left(\frac{\delta\beta_x}{\beta_x} \right) = (2Q_0)^2 \frac{1}{2} \beta_x^2(s) V_1(s) \tag{A.19}$$

A.2 K-modulation

Analysis based on [57]. In linear approximation, the transfer matrix between points s_0 and s has the form of:

$$\begin{bmatrix} x(s) \\ x'(s) \end{bmatrix} = \begin{bmatrix} \mathcal{C} & \mathcal{S} \\ \mathcal{C}' & \mathcal{S}' \end{bmatrix} \begin{bmatrix} x(s_0) \\ x'(s_0) \end{bmatrix}. \tag{A.20}$$

where $\mathcal{C}' := \frac{d\mathcal{C}}{ds}$ and $\mathcal{S}' := \frac{d\mathcal{S}}{ds}$, and the Twiss parameters propagate as [5]:

$$\begin{bmatrix} \beta(s) \\ \alpha(s) \\ \gamma(s) \end{bmatrix} = \begin{bmatrix} \mathcal{C}^2 & -2\mathcal{C}\mathcal{S} & \mathcal{S}^2 \\ -\mathcal{C}\mathcal{C}' & \mathcal{C}\mathcal{S}' + \mathcal{S}\mathcal{C}' & -\mathcal{S}\mathcal{S}' \\ \mathcal{C}'^2 & -2\mathcal{C}'\mathcal{S}' & \mathcal{S}'^2 \end{bmatrix} \begin{bmatrix} \beta_0 \\ \alpha_0 \\ \gamma_0 \end{bmatrix} \tag{A.21}$$

So, for the beta function:

$$\beta(s) = \mathcal{C}^2 \beta_0 - 2\mathcal{C}\mathcal{S}\alpha_0 + \mathcal{S}^2 \gamma_0, \tag{A.22}$$

where α_0 β_0 and γ_0 are the Twiss functions at s_0. Inside a focusing quadrupole of length L and strength k_1 the elements of the transfer matrix are

$$\mathcal{C} = \cos\left(\sqrt{k_1}s\right) \tag{A.23}$$

$$\mathcal{S} = \frac{1}{\sqrt{k_1}}\sin\left(\sqrt{k_1}s\right) \tag{A.24}$$

The spatial average beta function inside a quadrupole is calculated to be:

$$\bar{\beta} := \frac{1}{L}\int_{s_0}^{s_0+L}\beta(s)ds = \beta_0 u_0 - \alpha_0 u_1 + \gamma_0 u_2, \tag{A.25}$$

where the u_i coefficients are:

$$u_0 = \frac{1}{2}\left(1 + \frac{sin\left(2\sqrt{k}L\right)}{2\sqrt{k}L}\right), u_1 = \frac{sin^2\left(\sqrt{k}L\right)}{kL}, u_2 = \frac{1}{2k}\left(1 - \frac{sin\left(2\sqrt{k}L\right)}{2\sqrt{k}L}\right). \tag{A.26}$$

Applying a small variation in the strength of the focusing quadrupole δk, then the one turn map is:

$$M_{rev}(Q+\delta Q) = M_{rev}(Q)\cdot M_{QF}^{thin}(\delta k) \equiv M_{rev}(Q)\cdot\begin{bmatrix}1 & 0\\ \mp\delta k L & 1\end{bmatrix} \tag{A.27}$$

where the minus sign is for a focusing and the plus sign for a defocusing quadrupole. The two matrices must have the same trace (Wronskian invariant), so:

$$2\cos\left[2\pi(Q+\delta Q)\right] = 2\cos\left(2\pi Q\right) \mp \beta_0\delta k L\sin\left(2\pi Q\right), \tag{A.28}$$

By approximating β_0 with $\bar{\beta}$ (thin quadrupole), the induced tune shift can be found as:

$$\boxed{\delta Q = \pm\frac{1}{2\pi}cos^{-1}\left(cos(2\pi Q) \mp \frac{\bar{\beta}\delta k L}{2}sin(2\pi Q)\right) - Q \overset{\delta Q \text{ small}}{\approx} \pm\frac{\delta k\beta_0 L}{4\pi}}. \tag{A.29}$$

The sign in front of cos^{-1} depends on how the tune shifts with δk. By modulating the quadrupole strength by δk and measuring the induced tune shift δQ one can have a measure for the β-function inside the quadrupole. This method is know as k-modulation.

A.3 Resonance Driving Terms

Analysis based on [58]. The second order Hamiltonian for a particle in a periodic focusing system, in the two transverse planes, takes the form in action-angle variables (J_x, ϕ_x):

$$\hat{\mathcal{H}} = \frac{1}{R}(Q_x J_x + Q_y J_y). \tag{A.30}$$

A general perturbation potential:

$$V(x, y, s) = V_{m_x m_y} x^{m_x} y^{m_y}, \tag{A.31}$$

where m_x and m_y are integers, takes the form in action-angle variables:

$$V(\phi_x, \phi_y, J_x, J_y; s) = \frac{1}{R} J_x^{m_x/2} J_y^{m_y/2} \sum_{j=0}^{m_x} \sum_{l=0}^{m_y} h_{jklm} e^{i[n_x \phi_x(s) + n_y \phi_y(s)]} \tag{A.32}$$

where:

$$h_{jklm} = \frac{R}{2^{N/2}} \binom{m_x}{j} \binom{m_y}{l} \oint \beta_x^{m_x}(s) \beta_y^{m_y}(s) V_{m_x m_y} e^{i(n_x \phi_x + n_y \phi_y)} ds \tag{A.33}$$

and:

$$m_x = j + k, \qquad m_y = l + m \tag{A.34}$$

$$n_x = j - k, \qquad n_y = l - m \tag{A.35}$$

$$N = j + k + l + m \tag{A.36}$$

These complex coefficients h_{jklm} are called resonance driving terms and generate angle dependent terms in the Hamiltonian that can result to a resonance motion of the particles. The solution of the betatron motion to first order strength of the perturbation potential is proportional to:

$$x - ip_x \propto \frac{1}{1 - e^{-i2\pi(n_x Q_x + n_y Q_y)}} h_{jklm}. \tag{A.37}$$

If:

$$\boxed{n_x Q_x + n_y Q_y = p} \tag{A.38}$$

where p is integer, the perturbation will have slowly varying terms in the Hamiltonian that do not average to zero over many turns and lead to resonant motion. The order of the resonance is N and the harmonic of the perturbation is p. If n_x and n_y have the same sign the resonance is called sum resonance, otherwise it is called difference resonance.

Appendix B

Modeling Transverse Beam Distributions

B.1 Gaussian Distribution

Gaussian (normal) distribution.

$$f_G(x;\mu,\sigma) = \frac{1}{\sigma\sqrt{2\pi}} e^{-\frac{(x-\mu)^2}{2\sigma^2}} \tag{B.1}$$

B.2 Q-Gaussian Distribution

The q-Gaussian function is given by:

$$f_{qG}(x;q,\beta,\mu) = \frac{\sqrt{\beta}}{C_q} e_q\left(-\beta(x-\mu)^2\right) \tag{B.2}$$

with:

$$e_q(x) = \begin{cases} e^x, & \text{if } x = 1 \\ (1+(1-q)x)^{\frac{1}{1-q}}, & \text{if } q \neq 1 \text{ and } (1+(1-q)x) > 0 \\ 0, & \text{if } q \neq 1 \text{ and } (1+(1-q)x) \leq 0 \end{cases} \tag{B.3}$$

and:

$$C_q(x) = \begin{cases} \dfrac{2\sqrt{\pi}}{(3-q)\sqrt{1-q}} \dfrac{\Gamma\left(\frac{1}{1-q}\right)}{\Gamma\left(\frac{3-q}{2(1-q)}\right)}, & \text{for } -\infty < q < 1 \\ \sqrt{\pi}, & \text{for } q = 1 \\ \dfrac{\sqrt{\pi}}{\sqrt{q-1}} \dfrac{\Gamma\left(\frac{3-q}{2(1-q)}\right)}{\Gamma\left(\frac{1}{1-q}\right)}, & \text{for } 1 < q < 3 \end{cases} \tag{B.4}$$

where $\Gamma(n) = (n-1)!$. If the parameter q is equal to one, the distribution coincides to a Gaussian one. If q is greater than one, the tails are overpopulated, while if q is less than one the tails are underpopulated.

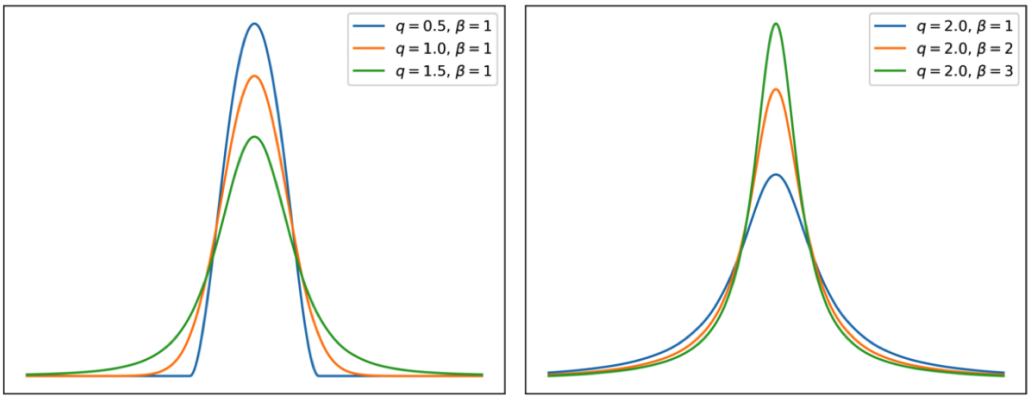

Figure B.1: q-Gaussian functions for different values of q and β.

In contrast to the double Gaussian function, the q-Gaussian function can represent both overpopulated and underpopulated tails with a single observable, the parameter q. Furthermore, since the Gaussian distribution is recovered as q approaches 1, the function is much more stable in terms of fitting measured beam profiles.

The RMS beam size in the Q-Gaussian function is calculated using:

$$\sigma_{QG} = \begin{cases} \sqrt{\dfrac{1}{\beta(5-3q)}}, & \text{for } q < 5/3 \\ \infty, & \text{for } 5/3 \leq q < 2 \\ \text{undefined}, & \text{for } 2 \leq q < 3 \end{cases} \tag{B.5}$$

Figure B.2 shows how a q-Gaussian (in blue) compares to a Gaussian function with a similar σ (in orange). The top-left graph shows a q-Gaussian profiles with underpopulated tails compared to a Gaussian ($q = 0.6$) and the other three q-Gaussian profiles with overpopulated tails ($q = 1.2$, $1 = 1.4$ and $q = 1.6$). The difference in the area between the q-Gaussian and Gaussian functions (that comes mostly from the tails but also from the peak in the profile center) is shown in percentage for different q-factors in Figure B.2.

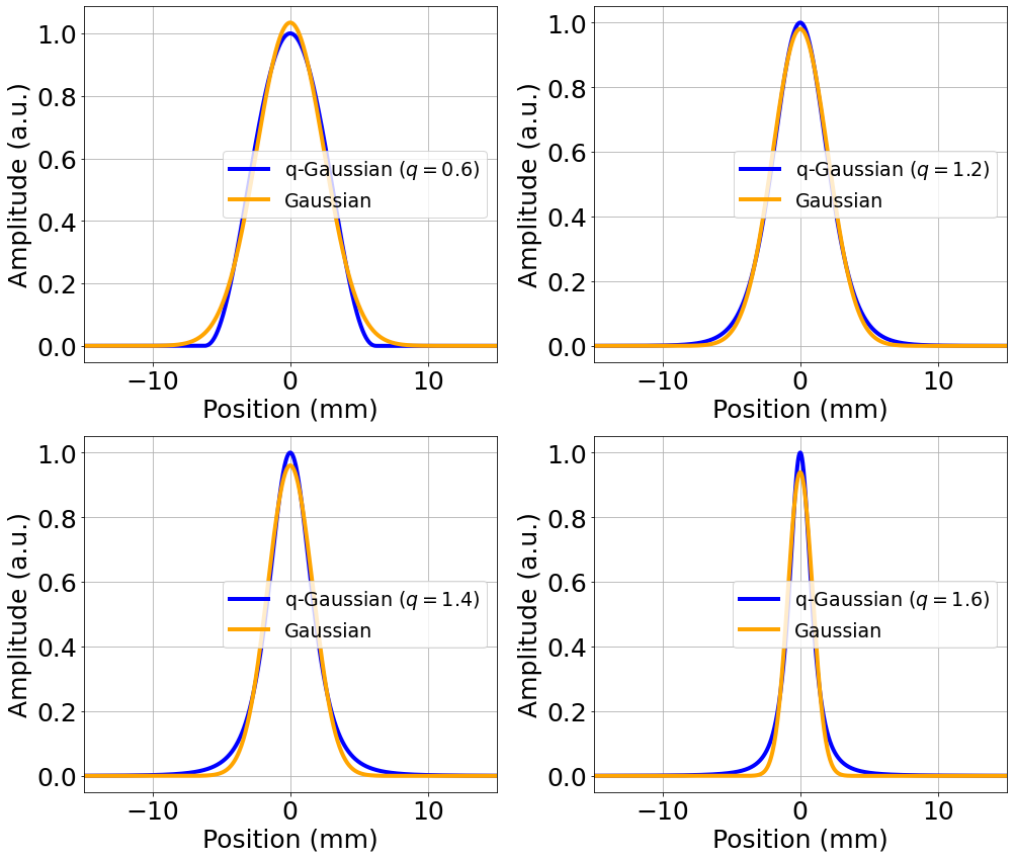

Figure B.2: Comparison of q-Gaussian functions with different values of the q-parameters to a Gaussian function that has a similar standard deviation (1σ).

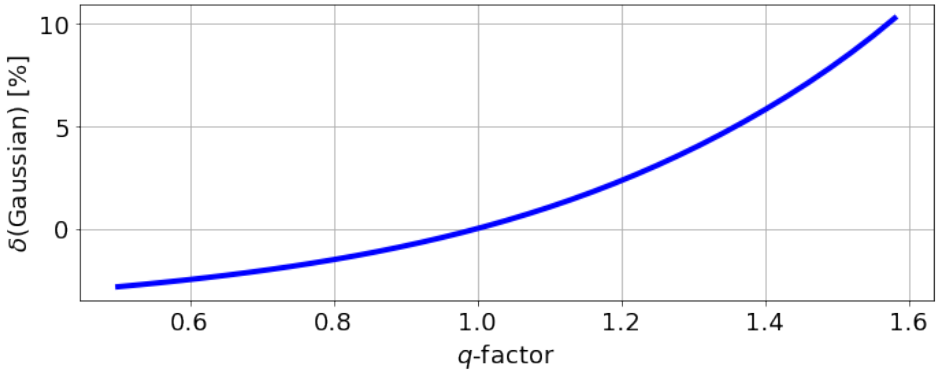

Figure B.3: Difference in the area (δ(Gaussian)) between a Gaussian and a q-Gaussian for different q-factors.

Bibliography

[1] "CERN Official Website, `https://home.cern/`".

[2] Oliver Sim Brüning, Paul Collier, P Lebrun, Stephen Myers, Ranko Ostojic, John Poole, and Paul Proudlock. *LHC Design Report Vol.1: The LHC Main Ring.* CERN Yellow Reports: Monographs. CERN, Geneva, 2004.

[3] Apollinari G., Béjar Alonso I., Brüning O., Fessia P., Lamont M., Rossi L., and Tavian L. *High-Luminosity Large Hadron Collider (HL-LHC): Technical Design Report V. 0.1.* CERN Yellow Reports: Monographs. CERN, Geneva, 2017.

[4] H Damerau, A Funken, R Garoby, S Gilardoni, B Goddard, K Hanke, A Lombardi, D Manglunki, M Meddahi, B Mikulec, G Rumolo, E Shaposhnikova, M Vretenar, and J Coupard. LHC Injectors Upgrade, Technical Design Report, Vol. I: Protons. Technical Report CERN-ACC-2014-0337, CERN, Dec 2014.

[5] Andrzej Wolski. *Beam Dynamics in High Energy Particle Accelerators.* Imperial College Press, 2014.

[6] Helmut Wiedemann. *Particle Accelerator Physics (Third Edition).* Springer, 2007.

[7] S. Y. Lee. *Accelerator Physics (Third Edition).* Wspc, 2011.

[8] "CERN Accelerator School (CAS), `https://cas.web.cern.ch`".

[9] "Joint Universities Accelerator School (JUAS), European Scientific Institude (ESI), `https://www.esi-archamps.eu/juas-presentation/`".

[10] K. H. Reich. The CERN Proton Synchrotron Booster. *IEEE Trans. Nucl. Sci.*, 16:959–961, 1969.

[11] Mauro Paoluzzi, Simon Albright, Maria Elena Angoletta, Luca Arnaudon, Salvatore Energico, Alan Findlay, Matthias Haase, Michael Jaussi, Anthony Jones, David Landré, John Molendijk, Danilo Quartullo, and Elena Shaposhnikova. Design of the New Wideband RF System for the CERN PS Booster. *CERN Internal Note*, page MOPMW024, 2016.

[12] Peter Forck, P Kowina, and Dmitry Liakin. Beam position monitors. *Synchrotron Radiation News*, 1, 01 2008.

[13] Robert C. Webber. Charged particle beam current monitoring tutorial. *AIP Conf. Proc.*, 333:3–23, 1995.

[14] Jose Luis Sirvent Blasco. Beam secondary shower acquisition design for the CERN high accuracy wire scanner, 2018. Presented 12 Dec 2018.

[15] Jonathan Emery, William Andreazza, David Belohrad, Salvatore Di Carlo, Jose C Esteban Felipe, Aurélie Goldblatt, Dmitry Gudkov, Ana Guerrero, Stephen Jackson, Guillaume O Lacarrere, Miguel Martin Nieto, Arnaud T Rinaldi, Federico Roncarolo, Christiane Schillinger, and Raymond Veness. Commissioning of the LHC Injectors BWS Upgrade. COMMISSIONING OF THE LHC INJECTORS BWS UPGRADE. *JACoW IBIC*, 2021:239–243, 2021.

[16] Jose Sirvent, Patrik Andersson, William Andreazza, Bernd Dehning, Jonathan Emery, Lionel Garcia, Dmitry Gudkov, Federico Roncarolo, Jean Tassan-Viol, Georges Trad, and Raymond Veness. Performance Assessment of Pre-Series Fast Beam Wire Scanner Prototypes for the Upgrade of the CERN LHC Injector Complex. *6th International Beam Instrumentation Conference*, page WEPCC03, 2018.

[17] M. Gasior and R. Jones. High sensitivity tune measurement by direct diode detection. In *7th European Workshop on Beam Diagnostics and Instrumentation for Particle Accelerators (DIPAC 2005)*, 10 2005.

[18] S Hancock and Sanchez Alvarez J-L. A pedestrian guide to online phase space tomography in the CERN complex. Technical report, CERN, Geneva, 2001.

[19] E.D Courant and H.S Snyder. Theory of the alternating-gradient synchrotron. *Annals of Physics*, 3(1):1–48, 1958.

[20] A. Wegscheider, A. Langner, R. Tomás, and A. Franchi. Analytical N beam position monitor method. *Physical Review Accelerators and Beams*, 20(11):111002, 2017.

[21] A. Garcia-Tabares, P.K. Skowroński, and R. Tomás. Optics Measurements in the CERN PS Booster Using Turn-by-Turn BPM Data. In *Proc. 10th International Partile Accelerator Conference (IPAC'19), Melbourne, Australia, 19-24 May 2019*, number 10 in International Partile Accelerator Conference, pages 285–288, Geneva, Switzerland, Jun. 2019. JACoW Publishing. https://doi.org/10.18429/JACoW-IPAC2019-MOPGW080.

[22] F. Asvesta et al. Resonance Compensation for High Intensity and High Brightness Beams in the CERN PSB. In *Proc. HB'21*, number 64 in ICFA ABDW on High-Intensity and High-Brightness Hadron Beams, pages 40–45. JACoW Publishing, Geneva, Switzerland, 04 2022.

[23] Karlheinz Schindl. Space charge. *CAS - CERN Accelerator School: Intermediate Accelerator Physics*, 2006.

[24] G. Franchetti and I. Hofmann. Modeling of space charge induced resonance loss. *AIP Conference Proceedings*, 642(1):260–262, 2002.

[25] G. Franchetti and I. Hofmann. Particle trapping by nonlinear resonances and space charge. *Nuclear Instruments and Methods in Physics Research Section A: Accelerators, Spectrometers, Detectors and Associated Equipment*, 561(2):195–202, 2006. Proceedings of the Workshop on High Intensity Beam Dynamics.

[26] Giuliano Franchetti and Ingo Hofmann. Resonance trapping due to space charge and synchrotron motion, in theory, simulations, and experiments. *HB 2006 - 39th ICFA Advanced Beam Dynamics Workshop on High Intensity High Brightness Hadron Beams*, 01 2006.

[27] W.J.M. Weterings, C. Bracco, L.O. Jorat, M. Meddahi, R. Noulibos, and P. Van Trappen. The New Injection Region of the CERN PS Booster. In *Proc. 10th International Particle Accelerator Conference (IPAC'19), Melbourne, Australia, 19-24 May 2019*, number 10 in International Particle Accelerator Conference, pages 2414–2417, Geneva, Switzerland, Jun. 2019. JACoW Publishing. https://doi.org/10.18429/JACoW-IPAC2019-WEPMP039.

[28] "MAD - Methodical Accelerator Design, `http://mad.web.cern.ch/mad/`".

[29] "PyORBIT-Collabiration, `https://github.com/PyORBIT-Collaboration`".

[30] F Schmidt, E Forest, and E McIntosh. Introduction to the polymorphic tracking code: Fibre bundles, polymorphic Taylor types and "Exact tracking". Technical report, CERN, Geneva, 2002.

[31] J. Galambos, S. Danilov, D. Jeon, J. Holmes, D. Olsen, J. Beebe-Wang, and A. Luccio. Orbit-a ring injection code with space charge. In *Proceedings of the 1999 Particle Accelerator Conference (Cat. No.99CH36366)*, volume 5, pages 3143–3145 vol.5, 1999.

[32] E. Benedetto, B. Balhan, J. Borburgh, C. Carli, V. Forte, and M. Martini. Detailed Magnetic Model Simulations of the H^- Injection Chicane Magnets for the CERN PS Booster Upgrade, including Eddy Currents, and Influence on Beam Dynamics. In *Proc. 5th International Particle Accelerator Conference (IPAC'14), Dresden, Germany, June 15-20, 2014*, number 5 in International Particle Accelerator Conference, pages 1618–1620, Geneva, Switzerland, July 2014. JACoW. https://doi.org/10.18429/JACoW-IPAC2014-TUPRI027.

[33] G Moritz. Eddy currents in accelerator magnets. *CAS*, 2010. Comments: 38 pages, presented at the CERN Accelerator School CAS 2009: Specialised Course on Magnets, Bruges, 16-25 June 2009.

[34] B. Mikulec, A. Findlay, V. Raginel, G. Rumolo, and G. Sterbini. Tune Spread Studies at Injection Energies for the CERN Proton Synchrotron Booster. In *Proc. HB'12, Beijing, China, September 17-21, 2012*. JACoW, 2012.

[35] T. Persson et al. LHC optics commissioning: A journey towards 1% optics control. *Phys. Rev. Accel. Beams*, 20(6):061002, 2017.

[36] B. Mikulec, A. Findlay, V. Raginel, G. Rumolo, and G. Sterbini. Lattice Issues of the CERN PSB with H- Charge Exchange Injection Hardware. In *Proc. PAC'2009, Vancouver, BC, Canada, May 4–8, 2009*. JACoW, 2009.

[37] T. Prebibaj et al. Injection Chicane Beta-Beating Correction for Enhancing the Brightness of the CERN PSB Beams. In *Proc. HB'21*, number 64 in ICFA ABDW on High-Intensity and High-Brightness Hadron Beams, pages 112–117. JACoW Publishing, Geneva, Switzerland, 04 2022.

[38] Rogelio Tomás, Masamitsu Aiba, Andrea Franchi, and Ubaldo Iriso. Review of linear optics measurement and correction for charged particle accelerators. *Phys. Rev. Accel. Beams*, 20:054801, May 2017.

[39] "Presentation at the ABP Injectors WG meeting #3, slide 37, `https://indico.cern.ch/event/910642/contributions/3830849/attachments/2030022/3403205/PSB_k-modulation_for_betabeating_correction_v9.3.pdf`".

[40] "2018 q-strip tests at 160 MeV, `http://elogbook.cern.ch/eLogbook/event_viewer.jsp?eventId=2701118`".

[41] "2018 reference measurements, `https://gitlab.cern.ch/PSB/reference_measurements/-/tree/master/tunes`".

[42] M McAteer, C Carli, B Mikulec, R Tomas, and M Aiba. Preliminary results of linear optics from orbit response in the CERN PSB. 2013.

[43] Holmes J. Shishlo A. and Gorlov T. The python shell for the orbit code *. In *Proceedings of ICAP09*, pages 351–354, 2009.

[44] F. Asvesta *et al.* Production of the LHC multi-bunch beams in the PSB. Presentation at Injectors Performance Panel meeting #11, CERN, Geneva, Switzerland, May 2020 [Online]. Available: `https://indico.cern.ch/event/915909/`.

[45] "PyQT5 - PyPI, `https://pypi.org/project/PyQt5/`".

[46] "Acc-Py Documentation Server, `https://acc-py.web.cern.ch/`".

[47] T. Prebibaj *et al.* Update on beta-beating measurement and correction during the fall of the PSB injection chicane. Presentation at Linac4-PSB MPC meeting #29, CERN, Geneva, Switzerland, June 2021 [Online]. Available: `https://indico.cern.ch/event/1051011/contributions/4415954`.

[48] S Papadopoulou, F Antoniou, T Argyropoulos, M Fitterer, M Hostettler, and Y Papaphilippou. Modelling and measurements of bunch profiles at the LHC. *Journal of Physics: Conference Series*, 874:012008, jul 2017.

[49] T. Prebibaj et al. Characterization of the Vertical Beam Tails in the CERN PS Booster. In *Proc. 13th International Particle Accelerator Conference (IPAC'22)*, number 13 in International Particle Accelerator Conference, pages 218–221. JACoW Publishing, Geneva, Switzerland, 07 2022.

[50] A. Santamaría García et al. Study of the Transverse Emittance Blow-Up Along the Proton Synchrotron Booster Cycle During Wire Scanner Operation. In *Proc. 10th International Particle Accelerator Conference (IPAC'19), Melbourne, Australia, 19-24 May 2019*, number 10 in International Particle Accelerator Conference, pages 1110–1113, Geneva, Switzerland, Jun. 2019. JACoW Publishing. https://doi.org/10.18429/JACoW-IPAC2019-MOPTS101.

[51] Federico Roncarolo. *Accuracy of the Transverse Emittance Measurements of the CERN Large Hadron Collider*. PhD thesis, Milan Polytechnic, 2005.

[52] Foteini Asvesta and Hannes Bartosik. Resonance Driving Terms From Space Charge Potential. *CERN-ACC-NOTE-2019-0046*, Oct 2019.

[53] F. Asvesta *et al.* Production of the LHC multi-bunch beams in the PSB. 5th ICFA Mini-Workshop on Space Charge, Oak Ridge 2022. Available: `https://conference.sns.gov/event/335/contributions/499/attachments/880/8154/resonanceCompensationHighBrightnessSCWS.pdf`.

[54] T Prebibaj. Transverse Emittance and Brightness Studies at Extraction of the CERN PS Booster, 2019.

[55] F. Antoniou et al. The PS Booster Alignment Campaign and a New Tune Control Implementation After the LHC Injectors Upgrade at CERN. In *Proc. HB'21*, number 64 in ICFA ABDW on High-Intensity and High-Brightness Hadron Beams, pages 89–94. JACoW Publishing, Geneva, Switzerland, 04 2022.

[56] T. Prebibaj, F. Antoniou, F. Asvesta, H. Bartosik, and G. Franchetti. Studies on the Vertical Half-Integer Resonance in the CERN PS Booster. In *Proc. 13th International Particle Accelerator Conference (IPAC'22)*, number 13 in International Particle Accelerator Conference, pages 222–225. JACoW Publishing, Geneva, Switzerland, 07 2022.

[57] Paul Conrad Vaagen Thrane. Measuring β^* in SuperKEKB with K Modulation, 2018. Presented 2018.

[58] Johan Bengtsson. Non-linear transverse dynamics for storage rings with applications to the low-energy antiproton ring (LEAR) at CERN, 1988. Presented on 1 Aug 1988.